Non-linear GaAs/AlOx waveguides for parametric down-conversion

Marco Ravaro

UNIVERSITE PARIS DIDEROT - PARIS 7

UFR DE PHYSIQUE

THESE

présentée pour obtenir le grade de

Docteur en Sciences de l'Université Paris 7

Nonlinear GaAs/AlOx waveguides for parametric down-conversion

Marco Ravaro

Soutenue publiquement le **30 janvier 2008**

JURY

M.	V. Berger	Examinateur
M.	A. Fiore	Rapporteur
M.	A. Godard	Examinateur
M.	G. Leo	Directeur de thèse
M.	J. Tignon	Rapporteur

To my father.

Acknowledgements

This work has been carried out at the MPQ laboratory of the Paris Diderot University. I'm grateful to Vincent Berger for allowing me to work in this young, lively, and stimulating laboratory and for constantly sustaining my research project. Thanks to his experience, creativity, and extensive knowledge of the physics of semiconductors he has been an irreplaceable source of inspiration throughout the years of my thesis.

It is difficult to express here all my gratitude to Giuseppe Leo. He has supported my entire scientific career, leading my first steps in research, at the Roma Tre University, and entrusting me with this ambitious research project under his direction. Besides friendly sustaining me on innumerable occasions, teaching me a lot, and transmitting me a part of his endless energy and determination, he is my example of passion for scientific research and culture. Thank you.

Sara Ducci has been a brilliant and competent co-worker, and a real friend. Besides her constant support to my experimental activities, her precious teachings and suggestions, she was an inexhaustible source of encouragement and good mood. I acknowledge her talent for didactics, her energy, and her endless availability.

I want to friendly thank Loïc Lanco and Jean-Pierre Likforman, my optical table partners, with whom I have shared the every-day difficulties and challenges of the experimental activity. Thank you for the numerous scientific discussions, for the tips exchanged, and for some memorable moment spent together. Working with you has been a real pleasure.

Pascal Filloux, Melanie Le Dû and Cristophe Manquest deserve all my gratitude for dealing with sample processing. Their skills in the clean room, their advice and constant availability have played a crucial role towards the results of this work. Thank you for your every-day support and the nice moments spent together as well.

I am grateful to Andrea Fiore, Antoine Godard, Isabelle Sagnes, and Jerome Tignon for accepting to take part to the examination committee. This manuscript has greatly benefited from their suggestions. Their interest in my work was an honour to me.

I want to thank all the members of the DON group that I have not yet mentioned, for their essential help to my experimental activities and their friendship: Alessio Andronico, Xavier Caillet, Lionel Deveaux, Ivan Favero, Aurore Gomez, and Erwan Guillotel. Thanks as well to Angela Vasanelli, Sukhdeep Dhillon, Yanko Todorov, Jean-Yves Bengloan, Luca Sapienza, Simone De Liberato, Carlo Sirtori, Stefano Barbieri, Edouard Boulat, and all the other members of the MPQ laboratory for the nice atmosphere in the lab.

During two years, while the own site of the Paris Diderot University Physics Department was in construction, my experimental setup was hosted in the laboratories of Thales Research and Technology, where I had the chance to interact with several nice people. I'm grateful in particular to Jean-Luc Reverchon for his experimental help and his endless availability, Xavier

Marcadet for sample growth, Alfredo De Rossi for scientific discussions, Alexandru Nedelcu, Olivier Guilcher, Eric Costard, Philippe Bois, Mathieu Carras, and Aude Leuliet for their kindness and niceness.

A few measurements presented in this thesis were performed at the Nonlinear Optics and Optoelectronics Laboratory of the Roma Tre University. I'm grateful to Gaetano Assanto, who first introduced me to the domain of nonlinear optics, for giving me the chance to work in his laboratory. In addition, I owe special thanks to Andrea Di Falco, Antonio Amoroso, Marco Peccianti, Andrea Fratalocchi and Lorenzo Colace for their constant support, their teachings, their pleasantry, and, above all, their friendship.

Finally, I'm infinitely grateful to my parents, who have always supported my choices and allowed me to arrive up to this point.

Résumé

Ce travail concerne des guides d'ondes semiconducteurs pour la génération et l'oscillation paramétrique. Dans de tels guides, la conversion de fréquence est accordée en phase grâce à un noyau multicouche biréfringent GaAs/AlOx. Cette technique d'accord de phase a déjà permis la réalisation de plusieurs interactions optiques non linéaires, telles que la génération de seconde harmonique et de différence de fréquence, ainsi que la fluorescence paramétrique. A présent, l'objectif est la réalisation d'un oscillateur paramétrique intégré semiconducteur. Notre travail dans cette direction a porté principalement sur deux points.

Le premier point est l'optimisation du processus de fabrication. Le principal inconvénient des guides d'ondes GaAs/AlOx sont les larges pertes par diffusion provoquées par la rugosité des couches oxydées. Des telles pertes ont pénalisé l'efficacité de dispositifs nonlinéaires intégrés déjà démontrés et empêché jusqu'à présent l'accomplissement de l'oscillation paramétrique. Dans le but d'améliorer la transmission des guides, un nouveau schéma de fabrication et d'oxydation a été introduit, et les résultats obtenus ont été systématiquement vérifiés par des mesures de pertes. Celles-ci ont été réduites, de manière reproductible, à 0.4 cm^{-1}.

Le deuxième point est la caractérisation nonlinéaire des guides. Nous avons démontré la fluorescence paramétrique avec une accordabilité entre 1.7 et 2.7 μm et une efficacité de conversion comparable à celle des meilleurs guides en niobate de lithium. En plus de cela, nous avons exploité les interactions de génération de seconde harmonique et d'amplification paramétrique pour étudier précisément le gain paramétrique dans nos guides. A la dégénérescence ($\lambda_S = \lambda_I \approx 2\ \mu m$) nous avons mesuré un coefficient de gain paramétrique $g / \sqrt{P_P} \approx 4\ cm^{-1}\ W^{-1/2}$ et démontré une amplification paramétrique $G = P_S(L)/P_S(0) - 1 \approx 4.5\%$.

Ces résultats sont très encourageants pour la réalisation d'un oscillateur paramétrique intégré. Sur la base de nos valeurs de pertes et de gain paramétrique nous estimons que la réflectivité des facettes requise pour atteindre le seuil d'oscillation dans une configuration doublement résonante est inférieure à 90%. Un premier essai de fabrication de miroirs intégrés a été effectué et le travail dans cette direction se poursuit actuellement au sein du laboratoire MPQ.

MOTS-CLES: Conversion de fréquence. Guides d'ondes AlGaAs. Accord de phase birefringent. Fluorescence paramétrique. Oscillation paramétrique.

Table of contents

List of figures

List of tables

Introduction: infrared generation by frequency down-conversion

Infrared (IR) radiation corresponds to the region of the electromagnetic spectrum with wavelengths between visible light (400-700 nm) and terahertz waves (0.1-10 mm). Conventionally, this interval is divided in three subregions: the near infrared (NIR), between 0.7 and 2.0 μm, the mid-infrared (MIR) from 2.0 to 20 μm, and the far infrared (FIR), from 20 to 100 μm.

Among these three intervals, the MIR range is of strong scientific and technological interest for spectroscopy. Several molecules exhibit their fundamental rotational-vibrational resonances in this region, with absorption spectra highly specific to their atomic structure. Chemical sensing has numerous key applications, both civilian, as atmosphere pollution monitoring or industrial process control, and military, e.g. the detection of neurotoxins. As MIR absorption lines are very strong, molecule concentrations as low as parts per-billion can be detected by means of laser-based detectors. In the NIR, where only overtone resonances can be excited, absorption peaks are weaker, and the corresponding detection thresholds several orders of magnitude higher.

At present, in spite of the lower sensitivity, many measurements are still performed at wavelengths below 2 μm, due to the absence of suitable laser sources at longer wavelengths. Infrared spectroscopy requires continuously tunable sources, with compactness and room temperature operation highly desirable. In the MIR, the present state of the art for this type of devices includes diode lasers and sources based on nonlinear frequency conversion. [Sorokina, 2003]

The main representatives of the former category are lead-salt, quantum-cascade and antimonide diode lasers. [Choi, 2004] Lead-salt diode lasers have been the workhorse for numerous successful sensing systems, and coverage of the whole 3-30 μm range has been demonstrated. However, they exhibit shortcomings in power, beam quality and spectral reproducibility, and require cryogenic cooling for continuous wave (CW) operation. Quantum cascade lasers (QCLs) hold great promise as an alternative free from these problems. They are proven to produce significant CW output power at room temperature in the 4-9 μm range, while maintaining single mode operation and being reproducibly tunable in a manner suitable for spectroscopy. Similar features are also typical of GaInAsSb/AlInAsSb laser diodes, covering

the 2-3 μm region. For all three of these families, tuning can be accomplished by changing either the temperature or the injected current. However, for a single device the overall tuning range is limited to some tenths of nanometers and is affected by longitudinal-mode hops. This major drawback can be significantly reduced by incorporating the diode into a grating-tuned external cavity. This solution, whose main technical issue is the deposit of an anti-reflection coating on one of the laser facets, has been successfully demonstrated for both antimonide diodes and QCLs.

IR sources based on three-wave mixing

A versatile alternative to laser diodes is represented by sources based on $\chi^{(2)}$ nonlinear processes. [Armstrong, 1962] Three-wave mixing is a well-known means of extending the operation of available lasers to further spectral regions, by exploiting the nonlinear optical properties of non-centrosymmetric crystals. The basic principle is as follows: two waves at angular frequencies ω_1 and ω_2, when injected into such crystals, give rise to a nonlinear polarization field oscillating at the frequencies $\omega_1+\omega_2$ and $\omega_1-\omega_2$. Accordingly, under opportune conditions, two waves at these frequencies are radiated from the crystal. Frequency conversion is now so well-established that it has been adopted for the fabrication of several commercial sources. One of the most significant examples is for green light generation, once the prerogative of gas lasers (Argon) and now mainly based on the frequency doubling of Nd^{3+} lasers oscillating at 1 μm.

For MIR generation, frequency conversion involves the use of an intense “pump” wave (generated by a laser), which is coupled to a seeded wave, the “signal”, and an “idler” wave generated at the difference frequency $\omega_p-\omega_s$. The initial source of photons for the signal wave can be either a second injected laser beam or quantum noise. In the former case the interaction is generally exploited in a single pass configuration and is referred to as difference-frequency generation (DFG). The latter process, called parametric fluorescence (PF), is generally exploited by resonantly enhancing the signal or the idler wave in a cavity containing the nonlinear medium, as the gain induced by the pump (parametric gain) is low. In this configuration, called optical parametric oscillator (OPO), if the parametric gain overcomes the overall losses in the cavity at the resonant frequency, the signal and idler waves oscillate.

DFG and OPOs are largely employed for the generation of MIR, as they can produce

coherent radiation in any temporal format and over a wide spectral range, only limited by the transparency of the nonlinear crystal. For both these processes, one of the main issues is the fulfillment of the phase-matching (PM) condition. For the signal and idler waves to be continuously fed by the pump as the beams propagate through the crystal, the three waves must stay unvaried in their initial phase relation. As the frequencies of the three fields are different, the phase-matching condition in general is not satisfied, due to crystal dispersion. The classical approach to achieve phase-matched propagation is based on the use of a birefringent nonlinear crystal. By properly polarizing some of the interacting waves along the ordinary axis and the remaining on the extraordinary axis, medium dispersion can be compensated. A more convenient way to fulfill the PM condition relies on microstructured crystals where the second-order susceptibility is periodically inverted, so as to keep the three waves into the correct phase relation. This technique, called quasi phase matching (QPM), was firstly demonstrated in ferroelectric crystal, like $LiNbO_3$ and KTP,[1] where such $\chi^{(2)}$ modulation can be achieved by reversing the crystal ferroelectric domains.

Even before the advent of QPM, which revolutionized the field of nonlinear optics, $LiNbO_3$ was the nonlinear crystal of choice, due to its numerous properties: wide transparency range, birefringence, thermal conductivity, and a considerable $\chi^{(2)}$ coefficient. The development of periodically poled lithium niobate (PPLN) further reinforced this position, including for the fabrication of infrared sources. The combination of high nonlinearity and long interaction length of PPLN has considerably increased the conversion efficiency of DFG and OPO systems based on this crystal, making them accessible to diode laser or fiber laser pumping.

The implementation of QPM had an even stronger impact on another optical nonlinear medium, gallium arsenide. This semiconductor has a $\chi^{(2)}$ coefficient considerably higher than those of $LiNbO_3$ and of most nonlinear crystals. Nevertheless, until the last decade it was not employed for frequency conversion, since it is neither anisotropic nor ferroelectric, and thus not readily suitable to the application of the above PM schemes. In 2001, the fabrication of the first effective QPM GaAs bulk crystals, [Eyres, 2001] rapidly opened the way for a series of tunable IR sources with impressive performances. In this orientation-patterned GaAs (OP-GaAs), the inversion of the nonlinear coefficient is obtained by means of epitaxial growth on a

[1] Potassium titanyl phosphate ($KTiOPO_4$).

peculiar, periodically patterned substrate. Among the results that followed from this technological innovation was the first GaAs-based OPO, reported in 2004. [Vodopyanov, 2004] Due to the high nonlinearity and wide transparency range of GaAs,[2] this device was continuously tunable between 2.2 μm and 9 μm (limited only by mirror reflectivity), with a maximum conversion efficiency of 25%. Based on these recent results, GaAs appears to be mature as an alternative to $LiNbO_3$ for the fabrication of NIR and MIR sources.

Integrated frequency converters for the IR generation

In terms of performances, frequency converters show substantial advantages compared to laser diodes. They are suitable for oscillation from continuous wave (CW) to femtosecond regimes, offer wider tunability ranges and great flexibility, especially since the advent of periodically poled materials. In addition, the recent demonstration of OP-GaAs promises to extend the versatility of PPLN-based sources to the whole MIR region. On the other hand, frequency converters are based on complex, often cumbersome setups that considerably limit their transportability, preventing their use outside of a laboratory setting. Despite the recent fabrication of miniaturized OPO sources, the degree of compactness offered by room-temperature or Peltier-cooled laser diodes remains unattainable for bulk nonlinear sources.

An intermediate solution between these two families of sources are guided-wave frequency converters, that potentially combine a compactness similar to that of semiconductor lasers with the performances of frequency conversion. In general, nonlinear interactions in waveguides offer several attractive features: compactness, on-chip integration with other devices and a variety of design solutions. In addition, the confinement of the interacting fields on a long propagation distance results in a conversion efficiency orders of magnitude higher compared to their bulk counterparts. On the other hand, the fabrication of waveguides is often technologically more complex than that of bulk crystals. The key issue are scattering losses, which can considerably limit the efficiency of nonlinear processes. In spite of such technological drawbacks, several highly-performing integrated frequency converters have been demonstrated to date. Similar to bulk crystals, PPLN has played a major role also for guided-wave generation both in the visible (through frequency up-conversion, [Kintaka, 1996]) and in

[2] GaAs transparency region, included between 0.9 and 17 μm, is far more extended in the MIR compared to that of $LiNbO_3$ (0.35-5 μm) and of most other common nonlinear crystals.

the IR (through down-conversion, [Bortz, 1995; Hofmann, 1999]).

With respect to PPLN, and to dielectric waveguides in general, GaAs integrated nonlinear devices offer the additional potential benefit of the integration with a pumping source. A tangible evidence of this appeal is given by the large number of integrated frequency converters reported in the last decade. Regretfully, to date, scattering losses have prevented GaAs waveguides from fully developing their potential. This is the case of QPM AlGaAs waveguides, based on the same inversion technique of OP-GaAs [Yu, 2005]. At present, a performing alternative to QPM is represented by form birefringence (FB) in GaAs waveguides. These integrated frequency converters, based on a strongly birefringent guiding core, were developed in the late 90's at the Thomson CSF (today Thales) laboratories. By embedding in a GaAs guiding layer several low-index AlOx [3] layers, a FB sufficient to fulfill the phase-matching condition in the NIR was attained. [Fiore, 1998b] As detailed in the following (Sections 1.2.4 and 2.2.2), AlOx layers result from the selective oxidation of AlAs layers embedded in the structure. Due to design versatility, this approach has since been successfully employed to phase match either down- or up-conversion interactions in the IR. [Fiore, 1997a; Fiore, 1998a; De Rossi, 2001]

From a technological point of view, in the last decade GaAs/AlOx approach has experienced a strong development. The very first conversion demonstrations suffered from processing immaturity, resulting in high propagation losses. At present, the conversion efficiency for both frequency doubling and down-conversion is comparable to that of $LiNbO_3$ counterparts. Nevertheless, a gap still remains in terms of propagation losses. This is the main obstacle towards the accomplishment of a resonant configuration, i.e. of an integrated OPO.

Within this scenario, this thesis aims at further developing GaAs/AlOx nonlinear waveguides. In particular we have focused on the IR generation by parametric down-conversion, after the first PF demonstration of 2001 [De Rossi, 2001]. Working on an integrated parametric generator pumped at 1 μm, with a strong appeal towards the field of IR spectroscopy, we have pursued two main tasks:

- the optimization of waveguide processing, based on a strong synergy between clean-room and optical characterization of the devices, in order to substantially reduce

[3] Non-stoichiometric aluminum oxide.

scattering losses;

- the extensive experimental investigation of the nonlinear properties of the waveguides, in order to reliably ascertain the nonlinear conversion efficiency.

The achievement of these objectives should open the way towards the ambitious goal of an integrated OPO in GaAs. This possibility has been explored, with the aid of numerical modeling, by studying different cavity configurations, as well as by fabricating and testing the first resonant devices.

Outline

In Chapter 1 we briefly overview the field of nonlinear quadratic interactions in AlGaAs waveguides. The basic concepts of nonlinear optics are presented through a brief description of several $\chi^{(2)}$ processes, in order to review the theoretical tools required for the following. After a short introduction to guided-wave frequency conversion, the main phase-matching schemes for AlGaAs waveguides are illustrated; in this context, the theoretical features and the state of the art of GaAs/AlOx FB waveguides are compared with those of alternative schemes.

In Chapter 2 we describe the design guidelines for our integrated parametric generator. Its main features (i.e. tunability, conversion efficiency, and fabrication tolerances) are investigated thoroughly. Subsequently, the fabrication procedure is outlined. Our contribution in this respect is highlighted, as well as the consequent benefits for the waveguide performances, which have been evaluated by measurements of propagation losses.

An extensive experimental nonlinear study of the device is the subject of Chapter 3. Besides PF experiments, two further nonlinear interactions have been performed: second-harmonic generation (SHG), and DFG. PF has allowed to investigate the complete tuning curve and the phase-matching bandwidth. SHG and DFG have been carried out in order to reliably evaluate the parametric gain.

Chapter 4 discusses the perspective of an integrated parametric oscillator. Firstly, we describe different possible configurations for an integrated OPO based on our GaAs/AlOx parametric generator. Secondly, we report the results of our calculations of the oscillation threshold, based on the experimental values of parametric gain and propagation losses. Thirdly, we detail the design and the fabrication of our first integrated dielectric mirrors.

Chapter 5 shows two examples of $\chi^{(2)}$ processes employed as characterization tools for

GaAs waveguides. Firstly, tunable PF is exploited to measure the optical losses of the waveguide on a broad wavelength interval. This approach has allowed us to quantitatively characterize an AlOx absorption peak between 3 and 4 μm. Secondly, surface-emitted frequency conversion. These interactions, which have proven as the most convenient technique to directly measure the birefringence of GaAs waveguide, are exploited here to investigate the efficiency of a counterpropagating twin-photons source.

1 Frequency conversion in AlGaAs waveguides

Nonlinear optics (NLO) is the subfield of optics that describes the optical effects arising from the interaction of intense optical fields with matter. The history of this science is strongly connected to that of laser sources. Until the first demonstration of the laser, dating back to the early 1960s, most of optical phenomena were described by linear equations. For the electric polarization $\vec{P}$ induced in a medium by the electric field $\vec{E}$ of an applied optical wave, a dependence $\vec{P} = \varepsilon_0 \chi \vec{E}$ was assumed.[4] However, as we know from other domains of physics, the linear description of a physical system is generally an approximation that holds only in a limited range. Indeed, the advent of intense coherent laser beams pointed out a series of light-matter interactions, previously unknown, requiring a nonlinear description of the vector $\vec{P}$. The first NLO process observed was a quadratic one, the frequency doubling of a ruby laser beam in a quartz crystal. [Franken, 1961] Since then, the improvement of pump sources and nonlinear media has turned quadratic NLO into an effective approach to generate coherent radiation at frequencies not attained by available lasers.

The intensity enhancement typically allowed by guided-wave geometry considerably reduces the power required for the accomplishment of a given nonlinear process and has granted optical waveguides a prominent position in the NLO scenario. In addition, the wealth of solutions offered by waveguide engineering has allowed the exploitation of nonlinear processes to theoretically and experimentally demonstrate a variety of complex functions for all-optical signal processing. These reports reinforced the hope for integrated optical circuits, where nonlinear optical devices act like electronic components in today's microelectronics.

In the first Section of this Chapter we review the basic concepts of nonlinear optics, focusing on the fundamental equations of three-wave mixing. The second Section, after an introduction to the main features of guided-wave nonlinear optics, describes the main phase-matching schemes adopted in AlGaAs waveguides.

1.1 Optical quadratic interactions: fundamental concepts

The most rigorous approach to the physics of NLO optics is based on quantum electrodynamics, treating both the medium and the optical field as quantized systems. Whereas this theory

[4] ε_0 is the vacuum electric permittivity and χ the electric linear susceptibility of the medium.

proves successful to explain any radiation-matter interaction, its formal complexity is not justified for our purposes. The NLO basic equations reported in the following result from a semi-classical treatment, which describes the medium through quantum mechanics and light radiation with the classical electromagnetic field theory. [Shen, 1984] The quantum description of the matter is exploited to obtain the expression of the macroscopic nonlinear electric susceptibilities of the medium, which then can be employed in Maxwell equations. With the exception of parametric fluorescence,[5] this theoretical approach is perfectly suitable to describe wave-mixing interactions. Here, the use of quantum electrodynamics will be limited to provide a simple additional description of some processes.

Let us consider the case of a typical optical medium: local, homogenous, with no free-carriers and far from resonances. The electric polarization associated to an electric field $\vec{E}$ can be expanded into a power series of $\vec{E}$

$$\vec{P}(t) = \overbrace{\underbrace{\varepsilon_0 \chi^{(1)}(t) \cdot \vec{E}(t)}_{\vec{P}^{(1)}}}^{\vec{P}^{L}} + \overbrace{\underbrace{\varepsilon_0 \chi^{(2)}(t) : \vec{E}(t)^2}_{\vec{P}^{(2)}} + \underbrace{\varepsilon_0 \chi^{(3)}(t) : \vec{E}(t)^3}_{\vec{P}^{(3)}} + \ldots}^{\vec{P}^{NL}} \tag{1.1}$$

where $\chi^{(n)}$ is a rank (n+1) tensor defining the nth-order susceptibility, with a structure determined by the crystal symmetry. Here we have singled out the term $\vec{P}^{L}$, describing the linear response of the medium, and the term $\vec{P}^{NL}$, including higher-order polarization terms.

In order to obtain the counterpart of Eq. 1.1 in the frequency domain, $\vec{E}(\vec{r},t)$ and $\vec{P}(\vec{r},t)$ have to be expressed through their Fourier transform. As in most practical situations the total electric field is given by the superposition of (quasi-) monochromatic waves (laser beams), it can be conveniently expressed as the sum

$$\vec{E}(\vec{r},t) = \sum_m \vec{E}_m(\vec{r},t) = \sum_m \frac{1}{2} \vec{e}_m E_m(\omega_m) \exp[i(\vec{k}_m \cdot \vec{r} - \omega_m t)] + c.c. \tag{1.2}$$

of waves of (angular) frequency ω_m, wavevector $k_m = \omega_m n_m / c$ and unit vector $\vec{e}_m$.[6] Note that here, for simplicity, we resort to the plane-wave approximation. Based on Eq. 1.2, the Fourier

[5] Where quantum noise acts like one of the input fields.

[6] c.c. stands for complex conjugate. While the field $\vec{E}_m$ is a real quantity, the wave amplitude E_m is conventionally complex valued to include the description of phase accumulation.

transform of Eq. 1.1 gives

$$\vec{P}(\omega) = \vec{P}^{(1)}(\omega)\delta(\omega-\omega_1) + \vec{P}^{(2)}(\omega)\delta[\omega-(\omega_1+\omega_2)] + \ldots \tag{1.3}$$

with

$$\vec{P}^{(n)}(\omega_{n+1}) = \varepsilon_0\chi^{(n)}(-\omega_{n+1};\omega_1,\omega_2,\ldots,\omega_n) : \vec{E}(\omega_1)\vec{E}(\omega_1)\ldots\vec{E}(\omega_n) \tag{1.4}$$

where the n+1 frequencies coupled by the nth-order susceptibility fulfill the summation relation

$$\sum_{j=1}^{n}\omega_j = \omega_{n+1} \tag{1.5}$$

Let us consider now the case of an electric field oscillating at the frequencies ω_1 and ω_2, focusing on $\vec{P}^{(2)}(\omega)$ and neglecting higher-order terms. Under these assumptions, the nonlinear polarization field oscillates at the frequencies $\omega_3 = \omega_1 + \omega_2$ (sum-frequency generation, SFG), $\omega_3 = \omega_1 - \omega_2$ (DFG), $\omega_3 = 2\omega_1$, $2\omega_2$ (SHG), and $\omega_3 = 0$ (optical rectification). For SFG and DFG processes, the projection of $\vec{P}^{(2)}(\omega)$ on the i-th axis (i = 1,2,3) results in

$$P_i^{(2)}(\omega_3) = \frac{\varepsilon_0}{2}\sum_{jk}\chi_{ijk}^{(2)}(-\omega_3;\omega_1,\omega_2)E_j(\omega_1)E_k(\omega_2) \qquad \text{(SFG)} \tag{1.6}$$

$$P_i^{(2)}(\omega_3) = \frac{\varepsilon_0}{2}\sum_{jk}\chi_{ijk}^{(2)}(-\omega_3;\omega_1,-\omega_2)E_j(\omega_1)E_k^{*}(\omega_2) \qquad \text{(DFG)} \tag{1.7}$$

Note that, with respect to reciprocal interactions, i.e. $\omega_3 = \omega_1 + \omega_2$, $\omega_1 = \omega_3 - \omega_2$, $\omega_2 = \omega_3 - \omega_1$, the second-order susceptibility tensor exhibits the following permutation symmetry

$$\chi_{ijk}^{(2)}(-\omega_3;\omega_1,\omega_2) = \chi_{jki}^{(2)}(-\omega_1;-\omega_2,\omega_3) = \chi_{kij}^{(2)}(-\omega_2;\omega_3,-\omega_1) \tag{1.8}$$

This property, that is valid also for higher order susceptibilities, results in the same photon conversion efficiency for reciprocal processes. Moreover, as we are considering a spectral region far from medium resonances,[7] the permutation symmetry is independent of the frequencies involved, turning into a relation between the different elements of the same tensor

[7] In this case $\chi^{(2)}$ dispersion can be neglected.

(Kleinman symmetry). [Kleinman, 1962] Under this assumption, the 3^3 elements of the $\chi^{(2)}$ tensor are reduced to only 10 independent elements.

1.1.1 The three-wave-mixing coupled equations

In the absence of charges, the wave equation for the electric field in an isotropic and non-magnetic $\chi^{(2)}$ dielectric, reads

$$\nabla^2\vec{E} = \frac{1}{c^2}\frac{\partial^2\vec{E}}{\partial t^2} + \frac{1}{\varepsilon_0 c^2}\frac{\partial^2\vec{P}}{\partial t^2} = \frac{\varepsilon}{\varepsilon_0 c^2}\frac{\partial^2\vec{E}}{\partial t^2} + \frac{1}{\varepsilon_0 c^2}\frac{\partial^2\vec{P}^{(2)}}{\partial t^2} \tag{1.9}$$

where the term $\frac{\partial^2\vec{P}^{(2)}}{\partial t^2}$ takes into account the energy transfer between fields at different frequencies, coupled by the second-order nonlinearity. In order to quantitatively analyze this process, let us consider the interaction between three collinear monochromatic plane waves at frequencies ω_1, ω_2, ω_3, with $\omega_3 = \omega_1 + \omega_2$.

$$\begin{aligned}
\vec{E}_1(\vec{r},t) &= \frac{1}{2}\{\vec{e}_1 E_1(z)\exp[i(k_1 z - \omega_1 t)] + c.c.\} \\
\vec{E}_2(\vec{r},t) &= \frac{1}{2}\{\vec{e}_2 E_2(z)\exp[i(k_2 z - \omega_2 t)] + c.c.\} \\
\vec{E}_3(\vec{r},t) &= \frac{1}{2}\{\vec{e}_3 E_3(z)\exp[i(k_3 z - \omega_3 t)] + c.c.\}
\end{aligned} \tag{1.10}$$

As the three waves exchange energy during propagation, with respect to Eq. 1.2 we have explicitly introduced the dependence of the three amplitudes on z.[8] However, we make the assumption that the variation of such amplitudes is small within the distance of one wavelength (slow-varying envelope approximation), i.e.

$$\frac{dE_i(z)}{dz}k_i >> \frac{d^2E_i(z)}{dz^2} \tag{1.11}$$

If Kleinman symmetry holds, by inserting Eqs. 1.6 and 1.10 in Eq. 1.9 we obtain the coupled equations for the SFG process $\omega_3 = \omega_1 + \omega_2$ [Armstrong, 1962]

[8] For $\vec{P}^{(2)} = 0$, the solution of eq. 1.9 is given by eq. 1.10 with $E_i(z)$ constant.

$$\begin{aligned}\frac{dE_1}{dz} &= -i\frac{\omega_1 d_{eff}}{n_1 c}E_2^* E_3 e^{-i\Delta kz}\\ \frac{dE_2}{dz} &= -i\frac{\omega_2 d_{eff}}{n_2 c}E_1^* E_3 e^{-i\Delta kz}\\ \frac{dE_3}{dz} &= -i\frac{\omega_3 d_{eff}}{n_3 c}E_1 E_2 e^{i\Delta kz}\end{aligned} \qquad (1.12)$$

where n_i is the refractive index of the medium at ω_i, $\Delta k = k_3 - k_2 - k_1$ the phase mismatch and d_{eff} is the effective nonlinear coefficient given by $d_{eff} = (1/2)\vec{e}_3 \cdot \chi^{(2)}(-\omega_3;\omega_1,\omega_2) : \vec{e}_1\vec{e}_2$. Similarly, for the DGF process $\omega_3 = \omega_1 - \omega_2$ we find

$$\begin{aligned}\frac{dE_1}{dz} &= -i\frac{\omega_1 d_{eff}}{n_1 c}E_2 E_3 e^{i\Delta kz}\\ \frac{dE_2}{dz} &= -i\frac{\omega_2 d_{eff}}{n_2 c}E_1 E_3^* e^{-i\Delta kz}\\ \frac{dE_3}{dz} &= -i\frac{\omega_3 d_{eff}}{n_3 c}E_1 E_2^* e^{-i\Delta kz}\end{aligned} \qquad (1.13)$$

where the phase mismatch is equal to $\Delta k = k_1 - k_2 - k_3$. These sets of equations describe the evolution of the amplitude of three waves coupled by the second-order nonlinearity. Note that the only difference between the two sets is given by the phase of the complex amplitudes E_i, which depends on the initial conditions and determines the direction of the energy transfer. In this respect, we stress the key role of the phase mismatch: if $\Delta k = 0$, the initial direction of the energy transfer between the interacting waves stays unvaried along the propagation direction, while for $\Delta k \neq 0$ it is periodically inverted. This behavior will be further discussed in the following, when the conversion efficiencies of up- and down-conversion processes will be calculated by integrating the three-wave-mixing equations along the propagation length.

1.1.2 Sum- and difference-frequency generation

Although the nonlinear coupled equations give a good description of $\chi^{(2)}$ processes, it is instructive to complement the above electromagnetic formalism with a quantum picture. This approach, relying on the concepts of virtual transition and intermediate state, provides a schematic and effective explanation of all nonlinear optical effects. [Shen, 1984] Unlike real

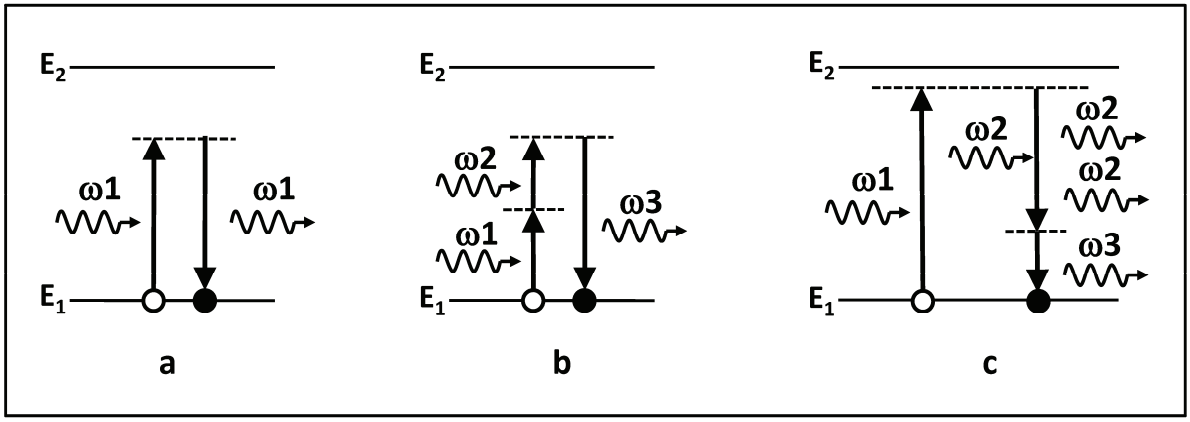

Figure 1.1 Virtual transitions in a two-energy-level system: transmission (a), sum-frequency generation (b), and difference-frequency generation (c).

transitions, like absorption or stimulated emission, which imply a resonant interaction of the field with the medium, virtual transitions occur towards an ultrashort-lifetime energy level, where the density of states is zero.

In Figure 1.1 three examples of virtual transitions are illustrated, with the medium represented as a system of two energy eigenlevels, E_1 and E_2. The scheme "a" shows the linear response of the medium: a photon at frequency ω_1 (with $\hbar\omega_1<E_2–E_1$) excites the system to a state that is not an eigenvalue of the energy, and is successively re-emitted as the system returns to the fundamental state. The short, but finite, lifetime of the excited state is responsible for the reduced light speed in the medium.[9] The scheme "b" represents a SFG process: after a first virtual transition, the system is further excited by a second photon at frequency ω_2 and its subsequent decay results in the emission of a photon at $\omega_3 = \omega_1 + \omega_2$. As this interaction requires that two photons excite the system within the short lifetime of the intermediate state, its probability is non negligible only for intense photon fluxes.[10] The DFG process can be described similarly, as shown in the scheme "c": in this case, the arrival of the second photon at frequency ω_2 ($< \omega_1$) induces a first partial decay of the system, resulting in the emission of a further photon of the same energy, through a process analogous to stimulated emission. Accordingly, a photon at frequency $\omega_3 = \omega_1 - \omega_2$ is emitted after the complete decay. This description clearly illustrates the two distinct features of DFG, which is at the same time a

[9] In classical electrodynamics this delay is accounted for by the material refractive index.

[10] According to Heisenberg uncertainty principle, the lifetime of the virtual state is as longer as nearer it is to the real state. This accounts for the increase of both the nonlinear coefficients and the refractive index near the resonances of the material.

frequency generation and an amplification process. In order to exploit the latter feature, the intensity of the field at ω_1 is set much higher than that of the field to amplify at ω_2. In this configuration, the three waves at ω_1, ω_2 and ω_3 are commonly referred to as pump, signal and idler, respectively.

Up- and down-conversion efficiencies can be readily calculated by integrating the nonlinear coupled equations (Eqs. 1.12 and 1.13) along the propagation distance, in the case of a low conversion efficiency, when the amplitudes of the two input fields stay constant along z. Let us treat first the SFG process. Based on the assumptions $E_1(z)=E_1(0)$, $E_2(z)= E_2(0)$, and $E_3(0)=0$ the integration of Eq. 1.12 over a distance L gives

$$\left|E_3(L)\right|^2 = \left(\frac{\omega_3 d_{eff}}{n_3 c}\right)^2 \left|E_1\right|^2 \left|E_2\right|^2 L^2 \left[\frac{\sin\left(\frac{\Delta kL}{2}\right)}{\frac{\Delta kL}{2}}\right]^2 \tag{1.14}$$

Integrating the intensities $I_i = 2\varepsilon_0 n_i c\left|E_i\right|^2$ on the transverse area A of the interacting beams, the conversion efficiency of the interaction reads

$$\eta = \frac{P_3}{P_1 P_2} = \eta_{norm}\, L^2 \left[\frac{\sin\left(\frac{\Delta kL}{2}\right)}{\frac{\Delta kL}{2}}\right]^2 \qquad [W^{-1}] \tag{1.15}$$

where P_i is the power at ω_i and

$$\eta_{norm} = \frac{1}{A}\frac{8\pi^2 d_{eff}^2}{n_1 n_2 n_3 \varepsilon_0 \lambda_3^2 c} \qquad [W^{-1}cm^{-2}] \tag{1.16}$$

with $\lambda_3 = 2\pi c/\omega_3$, the conversion efficiency normalized to the interaction length, at phase matching ($\Delta k = 0$). Under the same assumptions, the integration of Eq. 1.13 results in an identical expression for the conversion efficiency of the DFG process $\omega_3 = \omega_1 - \omega_2$.

In Eq. 1.15 the impact of the phase-matching condition is further clarified. For $\Delta k \neq 0$, as the polarization and the electric field at ω_3 experience different phase velocities, the energy transfer between the excitation fields and the generated one is periodically inverted along

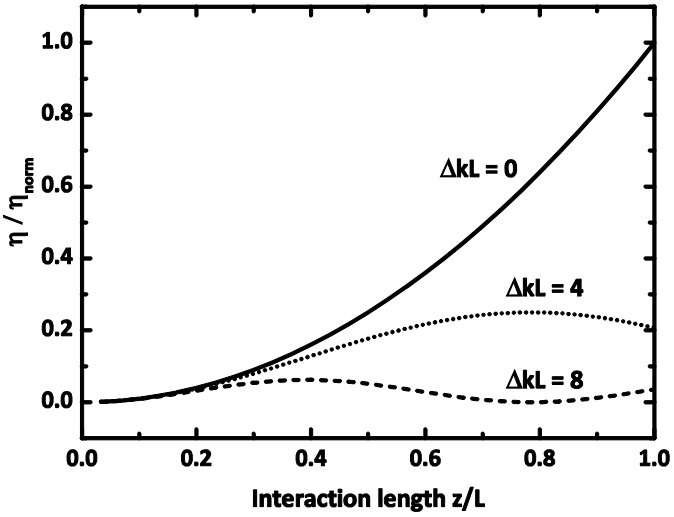

Figure 1.2 SFG conversion efficiency vs. interaction length for three different values of phase mismatch.

L, according to the coherence length $L_c = \pi/\Delta k$. As illustrated in Figure 1.2, this leads to a negligible conversion efficiency compared to the case of perfect phase matching, with the intensity of the sum frequency field growing monotonically as the square of the interaction length L. Accordingly, the phase-matching condition determines the spectral band of the conversion process, which exhibits a characteristic $sinc^2$ shape, as shown in Figure 1.3.

Due to normal dispersion, the phase-matching condition in optical media is generally not satisfied. The common approach to obtain phase matching is based on birefringent nonlinear crystals. In order to illustrate this technique, let us refer for the sake of simplicity to the case of degenerate SFG, i.e. SHG. The latter process is based on a single excitation wave at

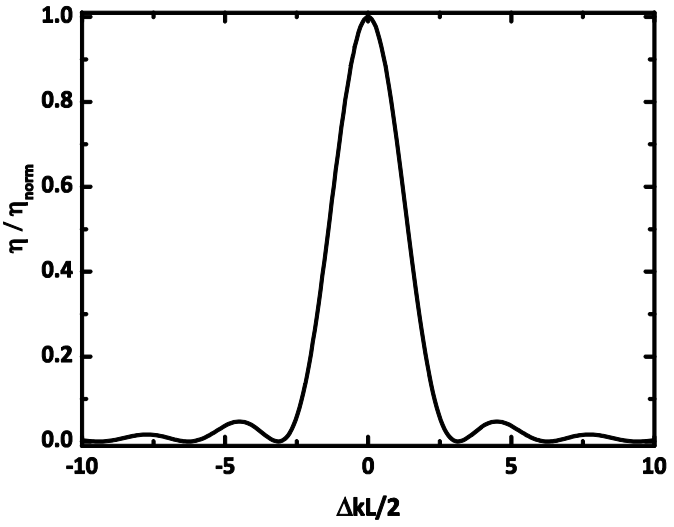

Figure 1.3 SFG normalized detuning curve.

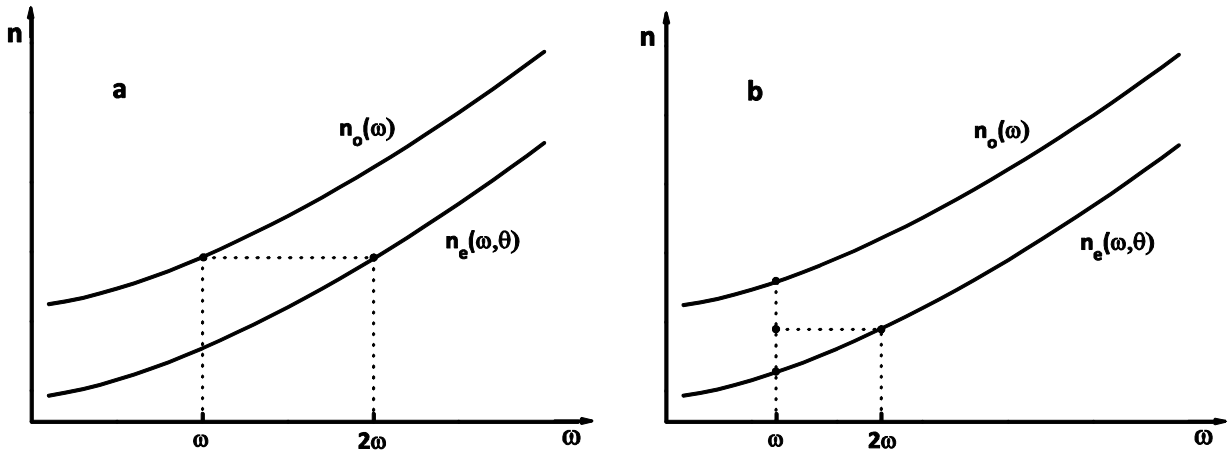

Figure 1.4 Type I (a) and type II (b) birefringent phase matching in a negative uniaxial crystal. Note that type I PM is suitable to compensate a larger dispersion.

the fundamental frequency ω, which acts like both the fields E_1 and E_2, resulting in a generated E_3 field at frequency 2ω. The phase mismatch for SHG can be written as $\Delta k = k_3 - k_2 - k_1 = k_{2\omega} - 2k_\omega = 4\pi(n_{2\omega}-n_\omega)/\lambda_\omega$, where n_ω ($n_{2\omega}$) and λ_ω ($\lambda_{2\omega}$) are the refractive index and the wavelength at ω (2ω), respectively. Through a proper polarization of the interacting fields, n_ω and $n_{2\omega}$ can be made equal by exploiting the crystal birefringence. As shown in Figure 1.4a, in a negative uniaxial medium this is possible for an ordinary wave at ω and an extraordinary wave at 2ω (type I PM), for which the PM condition reads $n_e(2\omega,\theta) = n_o(\omega)$.[11] An alternative SHG configuration is based on an extraordinary wave at 2ω arising from the interaction of an ordinary and an extraordinary wave at ω (type II PM). In this case, the PM condition is expressed by $2n_e(2\omega,\theta) = n_e(\omega,\theta)+n_o(\omega)$ (Figure 1.4b). Due to the angular dependence of the extraordinary index, the pair of phase-matched frequencies $(\omega,2\omega)$ can be tuned by rotating the crystal.

1.1.3 Parametric amplification and fluorescence

The amplification of a signal field at expense of an intense pump wave in a DFG interaction is known as optical parametric amplification (OPA). As the intensity of the signal is supposed to be initially weak and to significantly increase along the interaction length, the modeling of this configuration is based on different assumptions with respect to DFG. In this case Eq. 1.13 has to be integrated by setting $E_I(0)=0$, $|E_P(z)|\approx|E_P(0)|$ and $|E_S(0)|<<|E_P(0)|$.

[11] In an uniaxial crystal, the refractive index for the extraordinary wave depends on the angle θ between the direction of propagation and the extraordinary axis: $n_e(\theta,\omega)=[\cos^2(\theta)/n_o(\omega)^2+\sin^2(\theta)/n_e(\omega)^2]^{-2}$. [Yeh, 1988]

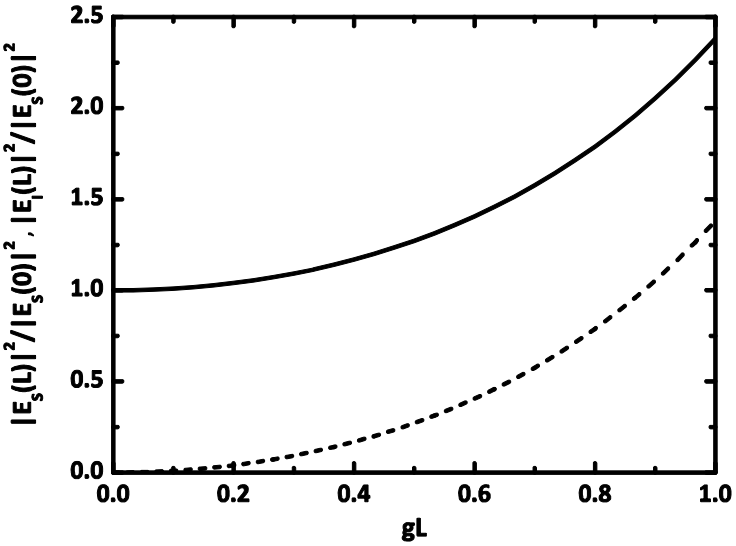

Figure 1.5 Normalized signal (solid line) and idler (dashed line) intensity vs. gL.

At phase matching, the resulting evolutions of signal and idler fields versus the interaction length L are expressed by (Figure 1.5)

$$\left|E_S(L)\right|^2 = \left|E_S(0)\right|^2 \cosh^2(gL) \tag{1.17}$$

$$\left|E_I(L)\right|^2 = \left|E_S(0)\right|^2 \sinh^2(gL) \tag{1.18}$$

where g is the parametric gain coefficient, defined as

$$g^2 = \frac{P_P}{A}\frac{8\pi^2 d_{eff}^2}{\varepsilon_0 n_P n_S n_I \lambda_S \lambda_I c} \quad [m^{-1}] \tag{1.19}$$

It is often useful to rewrite this expression through a degeneracy factor δ

$$g^2 = \frac{P_P}{A}\frac{8\pi^2 d_{eff}^2}{\varepsilon_0 n_P n_0^2 \lambda_0^2 c}(1-\delta^2) \quad [m^{-1}] \tag{1.20}$$

where $\lambda_0 = 2\,\lambda_P$, $n_0 \approx n_S \approx n_I$, $1+\delta = \lambda_0/\lambda_S$, and $1-\delta = \lambda_0/\lambda_I$ ($0 \le \delta \le 1$).

This formulation points out that parametric amplification is maximum at degeneracy[12] ($\delta = 0$) and decreases as signal and idler wavelength split ($\delta \to 1$). Signal power amplification is usually expressed in terms of the parametric gain G. Taking into account the phase mismatch:

[12] Note that at degeneracy $g/\sqrt{P_P} = \sqrt{\eta_{norm}}$ ($cm^{-1}W^{-1/2}$).

[Sutherland, 1996]

$$\frac{P_S(L)}{P_S(0)} = 1 + G = 1 + (gL)^2 \frac{\sinh^2\left(\sqrt{(gL)^2 - (\Delta kL/2)^2}\right)}{(gL)^2 - (\Delta kL/2)^2} \tag{1.21}$$

At phase matching $G(L)=\sinh^2(gL)$, which can be approximated as $G(L)=(gL)^2$ for low-gain ($gL \leq 1$). In general, for small gain $(gL)^2 << (\Delta kL/2)^2$

$$G \approx (gL)^2 \frac{\sin^2(\Delta kL/2)}{(\Delta kL/2)^2} \tag{1.22}$$

The co-generated idler power can be expressed in terms of parametric gain by the equation

$$\frac{P_I(L)}{P_S(0)} = \frac{\omega_I}{\omega_S} G \tag{1.23}$$

The generation of a signal and idler photon pair through the annihilation of a pump photon can also take place in the absence of a signal seed, albeit such a process cannot be described classically. This spontaneous parametric down-conversion (SPDC) of a pump photon is referred to as parametric fluorescence. It is of particular interest in the field of quantum optics, due to the correlation features of the down-converted photon pairs. [Bouwmeester, 2000] This process, which arises from the interaction of the pump with the quantum noise via the $\chi^{(2)}$ nonlinearity, can be conveniently modeled by addressing the pump classically and by quantizing the signal and idler fields. [Yariv, 1989] The contribution of quantum fluctuations is equivalent to the presence of one photon in either the signal or the idler modes, which locally interacts with the pump field producing a nonlinear polarization at all the possible frequencies between 0 and ω_P. However, the growth of the generated optical field is effective only at those frequencies that approximately fulfill the phase-matching condition. Accordingly, in order to evaluate the effective signal input, only the modes within the phase-matching band must be taken into account. The signal input power for frequencies between ω_S and $\omega_S + d\omega_S$ is obtained by putting one quantum of energy in each of the signal longitudinal modes in this band, divided by the transit time in the nonlinear medium $\tau = Ln_s/c$ [Byer, 1968; Baldi, 1996]

$$dP_S(0) = \frac{\hbar\omega_S}{2\pi} d\omega_S \tag{1.24}$$

The overall output idler power is obtained by integrating the associated dP_I, according to Eqs. 1.21 and 1.23

$$P_I(L) = (gL)^2 \frac{\omega_I}{\omega_S} \int_0^{\infty} \frac{\hbar\omega_S}{2\pi} \frac{\sinh^2\left(\sqrt{(gL)^2 - (\Delta kL/2)^2}\right)}{(gL)^2 - (\Delta kL/2)^2} d\omega_S \tag{1.25}$$

In the low gain regime ($gL \ll 1$), the approximation $(gL)^2 \ll (\Delta kL/2)^2$ is valid over almost all the integration range, except at the center of the PM band ($\Delta k \approx 0$), which does not contribute significantly to the integral in Eq. 1.25. This can thus be rewritten as

$$P_I(L) = (gL)^2 \frac{\omega_I}{\omega_S} \int_0^{\infty} \frac{\hbar\omega_S}{2\pi} \frac{\sin^2(\Delta kL/2)}{(\Delta kL/2)^2} d\omega_S \tag{1.26}$$

Hence, in the low gain regime, the generated idler exhibits a linear dependence on the pump power. Symmetrically, the generated signal power is expressed by a similar equation, obtained by considering quantum noise as an idler effective input.

As the pair of generated signal and idler wavelengths is determined only by frequency and momentum conservation, PF is typically widely tunable, over a range basically limited by the nonlinear crystal transparency. These desirable feature is illustrated in Figure 1.6, where the calculated tuning curve for a $LiNbO_3$ crystal is reported: here we have considered a simple

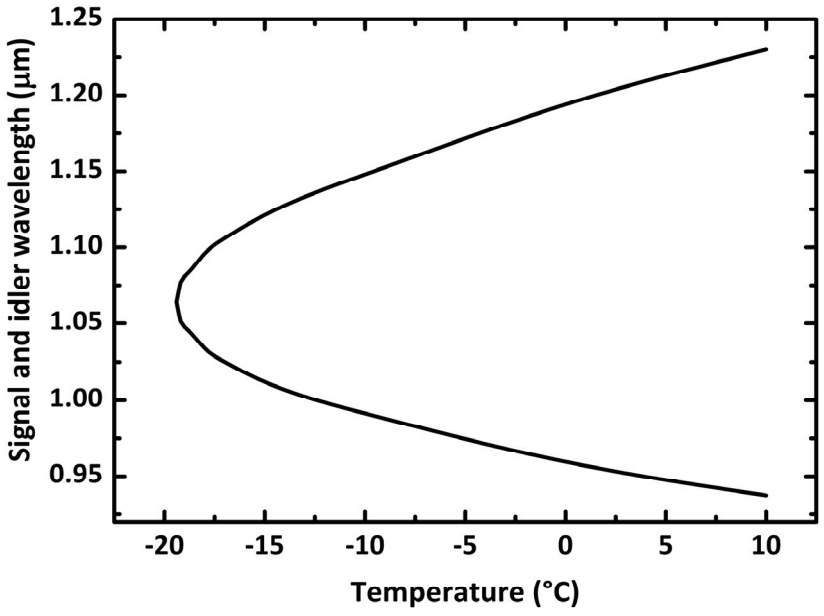

Figure 1.6 Calculated temperature tuning curve for parametric generation in a $LiNbO_3$ crystal, pumped at 532 nm in the extraordinary polarization.

type I non-critical PM scheme, with the pump and the generated fields polarized along the extraordinary and the ordinary axis, respectively. While tuning can be accomplished also by changing the pump wavelength or the crystal orientation, in this case we calculated the PM condition versus the crystal temperature, with a hundred of nanometers range covered by the generated wavelengths.

1.1.4 Optical parametric oscillation

As parametric amplification in a nonlinear crystal is generally low, even with an intense pump beam, the employment of a single-pass OPA is limited to a few specific applications. According to Eq. 1.19, a CW 10 W Nd:YAG beam focused on a 20 μm radius spot in a $LiNbO_3$ crystal results in a parametric gain coefficient $g \approx 0.14$ cm^{-1} at degeneracy ($\lambda_S=\lambda_I=2.128$ μm).[13] Only high peak power pulses from picosecond and femtosecond pump sources are suitable to produce a parametric gain sufficient to considerably amplify an injected seed, or to make the generated wave emerge from quantum noise in a single-pass configuration. The parametric gain achieved with CW (or quasi-CW) pumps is typically enhanced through a positive feedback to the generated waves, which is obtained by inserting the nonlinear crystal in an optical cavity. As in a laser, when the parametric gain overcomes the overall losses inside the cavity, the generated fields oscillate, resulting in two coherent output beams. Such a device, known as optical parametric oscillator (OPO), has been studied and demonstrated with several different cavity configurations. Among these, two common schemes are the singly-resonant OPO (SROPO) and the doubly-resonant OPO (DROPO). Referring to Figure 1.7, in the former geometry the cavity is resonant only at signal (idler) wavelength, i.e. $R_P \approx 0$, $R_S \approx 1$, $R_I \approx 0$ ($R_P \approx 0$, $R_S \approx 0$, $R_I \approx 1$), while in the latter both the generated wavelengths are resonating, i.e. $R_P \approx 0$, $R_S \approx 1$, $R_I \approx 1$. Note that, unlike in a laser, the gain in the active medium is unidirectional: as the PM condition is fulfilled only when the three waves are copropagating, signal and idler are amplified in the nonlinear crystal only in one propagation direction.[14] By equating cavity losses in a round trip and single-pass parametric amplification, the gain threshold for a SROPO results [Sutherland, 1996]

[13] For type I non-critical phase matching, with d_{eff}=5pm/V.

[14] However, in some cavity configuration, the pump is made pass through the crystal forward and backward, thus amplifying the generated waves in both propagation directions.

$$(g_{th}L)^2 \approx 2\left[1 - R_S \exp(-\alpha_S L)\right] \tag{1.27}$$

In a DROPO, due to the simultaneous cavity enhancement of signal and idler fields, the threshold is significantly lower:

$$(g_{th}L)^2 \approx \left[1 - R_S \exp(-\alpha_S L)\right]\left[1 - R_I \exp(-\alpha_I L)\right] \tag{1.28}$$

with $(g_{th}L)^2_{SROPO}/(g_{th}L)^2_{DROPO} \approx 2/[1-R_I\exp(-\alpha_I L)] \approx 100$ for $R_I = 99\%$ and $\alpha_I L = 0.01$. For pumping levels above threshold, at steady state, the gain coefficient is clamped at g_{th} through pump depletion, with the pump power exceeding the threshold value P_{th} transferred to the generated fields and to a "reflected" pump wave.[15] The conversion efficiency $\eta = (P_S+P_I)/P_P$, which depends on the OPO configuration, is typically maximized for P_P/P_{th} ranging from 2 to 4 and can reach values higher than 80%. [Bosenberg, 1996]

The most relevant feature of OPOs is the tunability of the emitted wavelengths: since these do not depend on a resonance of the active medium but only on frequency conservation and on the PM condition along the cavity axis, a wide spectral range is attainable, typically limited by the high-reflectivity band of the cavity mirrors. The emission linewidth of signal and idler depends on the parametric gain bandwidth, the pump beam spectrum, and the features of the OPO cavity: free spectral range (FSR) and finesse (F).[16] With a monochromatic pump the features of a SROPO are similar to those of a laser with homogenous line broadening. On the

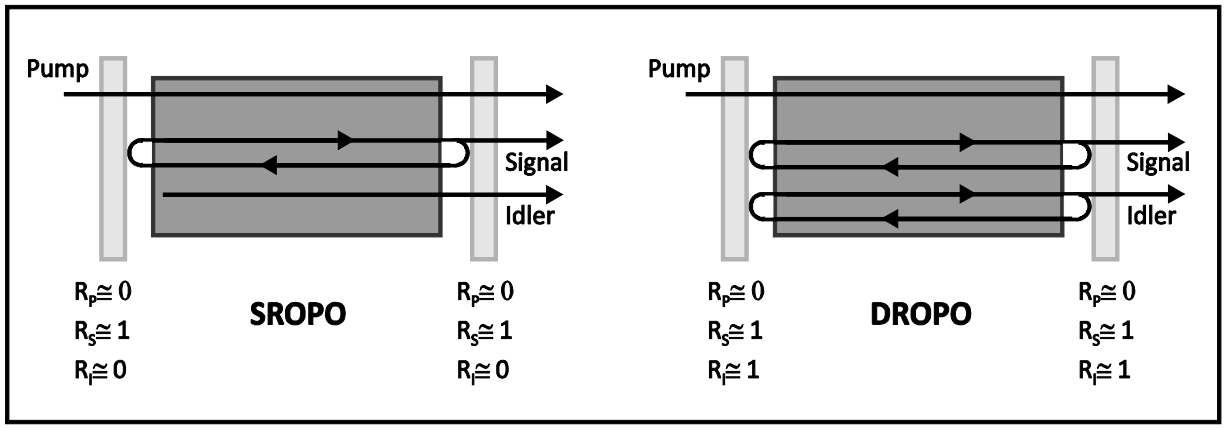

Figure 1.7 Singly- and doubly-resonant OPO schemes.

[15] The reflected pump is a sum-frequency wave generated by the backward travelling signal and idler in the cavity.

[16] The free spectral range of a cavity of length L is the frequency spacing between two subsequent longitudinal modes. It is expressed by FSR = c/2nL, where n is the refractive index inside the cavity. The finesse is defined as the ratio between the FSR and the spectral width of the longitudinal modes.

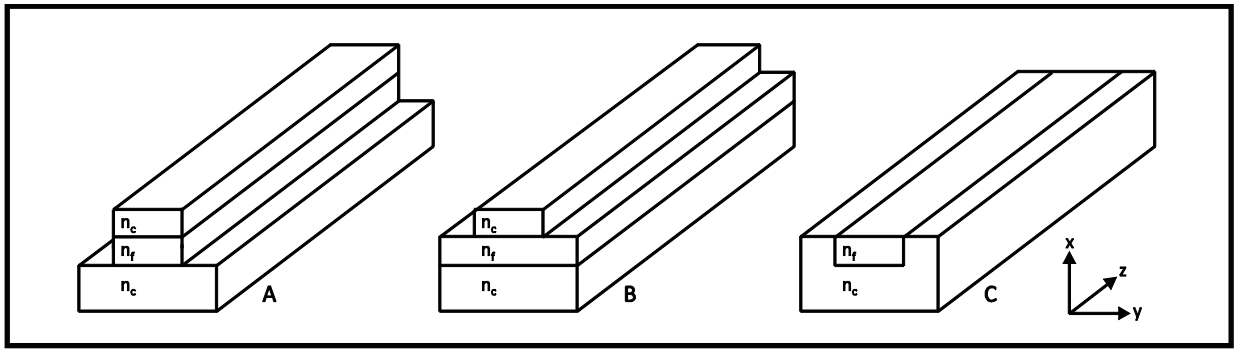

Figure 1.8 Ridge waveguide geometries, with (A,B) and without upper cladding (C).

other hand, a DROPO exhibits a more complex behavior that stems from the discretization of both signal and idler wavelengths dictated by the cavity longitudinal modes; this results in poor frequency stability and discontinuous tuning, affected by mode hopping. The detailed characteristics of SROPO and DROPO, in terms of both conversion efficiency and spectral features, will be the subject of Chapter 4.

1.2 Nonlinear AlGaAs waveguides

1.2.1 Thin-film waveguides

An optical waveguide is a physical structure where the electromagnetic radiation in the optical spectrum can propagate being confined in the transverse dimensions. This is obtained through a proper dielectric constant distribution, in general invariant along the propagation direction. The most simple type of optical waveguide is the slab waveguide, which consists of a dielectric layer (guiding film), with a thickness of the order of the wavelength, included between two semi-infinite bounding media of lower refractive index (claddings). In such a structure an optical wave can propagate along a direction (z) in the layer plane, being confined in the direction orthogonal to the interfaces (x), due to total internal reflection at the guiding film boundaries. For this configuration the solutions of Maxwell equations for a given wavelength are in a discrete number and are called guided modes. [Yeh, 1988] These can be divided into two sets, according to their polarization: TE modes, with the electric field E y-polarized and the magnetic field H polarized in the x-z plane (H_x, H_z, E_y), and TM modes, with inverted polarizations (E_x, E_z, H_y). Each TE and TM mode is identified by an index m=0,1,2,.. and is characterized by:

- an effective index n_{eff}, included between that of the guiding film and that of the claddings, which expresses its phase velocity.

- a field spatial distribution in the transverse direction x, invariant along the propagation direction z, which presents a number of zeros equal to the modal order m.

Among the various approaches developed, [Hunsperger, 2002] a slab waveguide can be readily fabricated through the epitaxial growth of an AlGaAs heterostructures, due to the dependence of the AlGaAs refractive index on the Al molar fraction. Moreover, this technology allows to go beyond the fabrication of a simple guiding film sandwiched between two claddings, and to grow complex multilayered structures where the effective index dispersion can be finely engineered, after the example of dispersion-flattened optical fibers. [Cohen, 1982]

In slab waveguides the confinement of energy is limited to one dimension, while in the y direction the radiation is affected by diffraction. Such geometry is thus of limited usefulness, and in practice most optical waveguides provide a two-dimensional (2D) confinement. In AlGaAs planar waveguides lateral guidance can be introduced by a post-growth etching which leaves intact a thin stripe ("ridge") of the epitaxial structure. Hence, in the y direction the optical field is confined in the high index contrast structure air/AlGaAs/air. This confinement of light was a key issue in the development of room temperature semiconductor laser diodes in the late 60s and early 70s. Some different 2D waveguide configurations are shown in Figure 1.8: in such rectangular-section waveguides the order of a mode is expressed by two indices, equal to the number of zeroes of the modal field distribution along the two transverse direction. The field associated to a 2D guided mode can be expressed as

$$E = B\phi_{m,n}(x,y)\exp[j(\beta_{m,n}z - \omega t)] \tag{1.29}$$

with $\beta_{m,n} = n_{eff}\,\omega/c$ the propagation constant, B [V] the complex amplitude and $\phi_{m,n}(x,y)$ [m^{-1}] the modal field distribution, for which the normalization

$$\int \phi_{m,n}(x,y)\phi_{m,n}(x,y)dxdy = 1 \tag{1.30}$$

is adopted. After normalization, the power carried by the mode is equal to $P = c\,\varepsilon_0 n_{eff}|B|^2/2$.

In general, the guided modes of 2D waveguides cannot be classified according to their polarization, as all of them exhibit a non negligible projection of both E and H fields on the three axis. However, in semiconductor waveguides, the confinement provided by the epitaxial structure is usually much more narrow than that provided by the ridge. In such circumstances the modes can be classified as quasi-TE (quasi-TM) with E (H) field predominantly oscillating in

the y direction. Moreover, in such quasi-planar waveguides the effective index of the $TE_{m,0}$ and $TM_{m,0}$ modes is well approximated by that of the corresponding TE_m and TM_m modes of the planar counterpart. In this case, although with current personal computers the effective indices of 2D waveguides can be readily calculated,[17] the resort to planar approximation proves convenient when these parameters must be extensively calculated.

1.2.2 Guided-wave frequency conversion

Hereafter, the expression for the normalized conversion efficiency in guided-wave geometry is inferred. To this purpose, with respect to the plane-wave treatment, we have to take into account the field distribution of the interacting modes. Moreover, the different media which compose the waveguide structure have in general different nonlinear coefficients: also their spatial distribution must be accounted for.

Let us consider three interacting modes, with amplitudes expressed by Eq. 1.29. Here we assume that B is a slowly varying function of the propagation direction z, to take into account the energy exchange between the three waves. The spatial overlap between the modal distributions $\phi_1(x,y)$, $\phi_2(x,y)$ and $\phi_3(x,y)$ and the nonlinear coefficient $d_{eff}(x,y)$ can be expressed through the nonlinear overlap integral

$$\Gamma = \int d_{eff}(x,y)\phi_1(x,y)\phi_2(x,y)\phi_3(x,y)dxdy \qquad [V^{-1}] \tag{1.31}$$

Γ summarizes the key features of the guiding structure with respect to the nonlinear process: the medium nonlinearity, the normalized intensity of the three modes and their spatial overlap. Focusing on a guided wave SFG process $\omega_3 = \omega_1 + \omega_2$, the nonlinear coupled equations (Eq. 1.12) can be reformulated as

$$\begin{aligned}
\frac{dB_1}{dz} &= -i\frac{\omega_1}{n_{eff\,1}c}\Gamma B_2^* B_3 e^{-i\Delta kz} \\
\frac{dB_2}{dz} &= -i\frac{\omega_2}{n_{eff\,2}c}\Gamma B_1^* B_3 e^{-i\Delta kz} \\
\frac{dB_3}{dz} &= -i\frac{\omega_3}{n_{eff\,3}c}\Gamma B_1 B_2 e^{i\Delta kz}
\end{aligned} \tag{1.32}$$

[17] For step-index waveguides, the fully vectorial calculation of the effective index and of the field distribution of a guided mode takes few minutes with commercial softwares on standard personal computers.

where the indices of refraction of the bulk case have been replaced by the effective indices, also in the phase mismatch $\Delta k = 2\pi(n_{eff3}/\lambda_3 - n_{eff2}/\lambda_2 - n_{eff1}/\lambda_1)$. The integration of Eq. 1.32 leads to the same expression of Eq. 1.15, where the normalized conversion efficiency is given by

$$\eta_{norm} = \frac{8\pi^2}{n_{eff1} n_{eff2} n_{eff3} c\varepsilon_0 \lambda_3^2} |\Gamma|^2 \quad [W^{-1}cm^{-2}] \tag{1.33}$$

By comparing Eqs. 1.33 and 1.16, we can conveniently define the effective area

$$A_{eff} = \left| \frac{\max(d_{eff})}{\Gamma} \right|^2 \quad [m^2] \tag{1.34}$$

which allows to employ the expressions for the conversion efficiency in plane-wave approximation for the guided-wave case.

1.2.3 Modal phase matching in AlGaAs waveguides

The phase mismatch in a guided-wave interaction depends on the effective indices of the interacting modes rather than on the refractive indices of the material. This feature offers a high degree of flexibility towards the fulfillment of the PM condition, as this can be satisfied through multimode dispersion. Moreover, as the dispersion of the different effective indices can be finely engineered trough a convenient design of the waveguide, both PM wavelengths and bandwidth can be finely adjusted.

The AlGaAs second-order nonlinear tensor presents only three non-zero elements: χ_{xyz}, χ_{yxz} and χ_{zxy}. They couple three electric fields, each polarized along one principal dielectric axis. Accordingly, for AlGaAs quasi-planar waveguides grown on standard (100) substrates, one of the three interacting modes must be TM-polarized and the remaining two TE-polarized. Then the effective nonlinear coefficient depends then on the in-plane propagation direction: it is maximum and equal to $\chi_{xyz}/2$ for a (011) oriented ridge, while it is zero for propagation along (010) direction. As the former orientation allows to exploit the natural cleavage planes to define the waveguide facets, this is by far the most common configuration.

Let us consider a practical SHG scheme, the frequency doubling of a TE_0 field into a second harmonic n-th order TM mode, in the multilayer guiding structure [GaAs (substrate), 2000 nm $Al_{0.7}Ga_{0.3}As$, 1500 nm GaAs, air]. The phase-matching condition in this case is

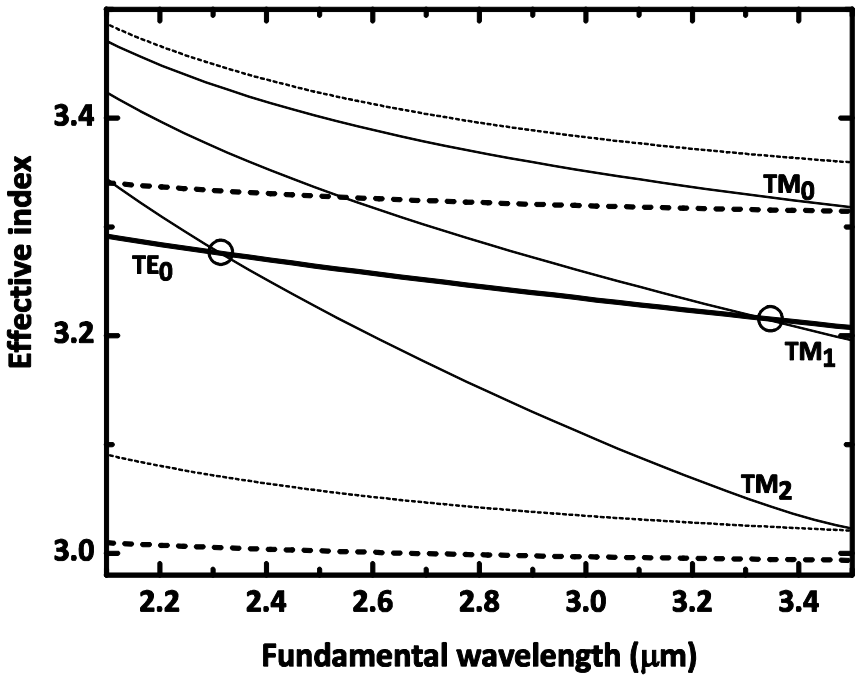

Figure 1.9 Effective indices (solid lines) and refractive indices of film and cladding (dashed lines) for the guiding structure [GaAs (substrate), 2000 nm $Al_{0.7}Ga_{0.3}As$, 1500 nm GaAs, air]. Mode polarization is TE at ω (thick lines) and TM at 2ω (thin lines). Two phase-matched interactions are allowed: $TE_0(\omega)$-$TM_2(2\omega)$ at 2.3 μm and $TE_0(\omega)$–$TM_1(2\omega)$ at 3.3 μm.

$n_{TE0}(\omega)=n_{TMn}(2\omega)$. As shown in Figure 1.9, where the effective indices of the guided modes are traced versus wavelength, such condition is fulfilled for two fundamental wavelengths: 2.313 μm, for the pair of modes $TE_0^{\omega} - TM_2^{2\omega}$; and 3.33 μm, for the pair $TE_0^{\omega} - TM_1^{2\omega}$. The phase-matched wavelengths follow from the waveguide design and can be readily shifted by varying the guiding film thickness or its composition.[18] This example illustrates the easy attainability of modal phase matching (MPM) in generic AlGaAs waveguides. However, there is a price to pay for such a flexibility: the low nonlinear overlap integral (i.e. the large effective area) arising from the field distribution of different-order modes, as suggested in Figure 1.10. In a 3 μm wide ridge the calculated effective area of the interaction for the TE_0-TM_2 pair is A_{eff}=643 μm^2 while for the TE_0-TM_1 pair is A_{eff}=1318 μm^2. Such areas are much larger than those associated to interactions between fundamental modes, which are comparable to the waveguide transverse

[18] The fabrication of an etched ridge on such planar structure would only result in a shift of all the phase-matching wavelengths, the larger the narrower is the lateral confinement. For large ridges, with a resulting modal profile much wider along y than along x direction, this shift is negligible.

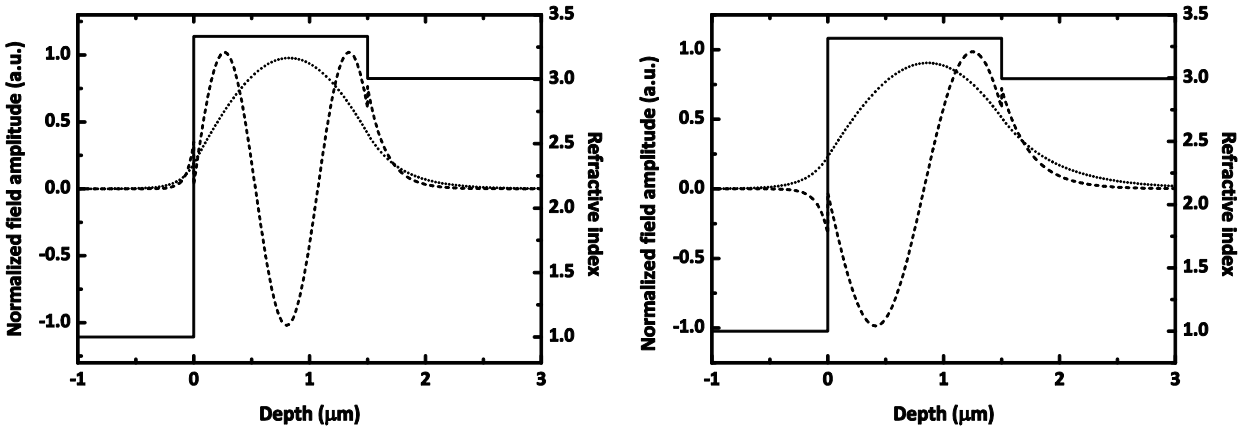

Figure 1.10 Refractive index profiles and normalized modal profiles for the guiding structure [GaAs (substrate), 2000 nm $Al_{0.7}Ga_{0.3}As$, 1500 nm GaAs, air]. Left: TE_0 (dotted line) and waveguide index (solid line) profile at λ = 2.3 μm plus TM_2 (dashed line) profile at $\lambda/2$. Right: TE_0 (dotted line) and waveguide index (solid line) profile at λ = 3.3 μm plus TM_1 profile (dashed line) at $\lambda/2$.

section (≈ 10 μm^2). Although an optimized design of the waveguide profile can significantly increase the nonlinear overlap and thus the conversion efficiency, with effective areas as low as 100 μm^2, [Oster, 2001] an optimum exploitation of guided-wave frequency conversion requires an interaction between fundamental order modes.

1.2.4 Form-birefringent GaAs/AlOx waveguides

In interactions between fundamental order modes, the need for dispersion compensation requires a PM scheme analogous to those employed in bulk crystals. Hereafter, we focus in particular on birefringent PM.

A significant difference n_{TE0}-n_{TM0}, referred to as modal birefringence, can e.g. be achieved by fabricating waveguides with birefringent materials like $LiNbO_3$. Clearly, even in the case of isotropic media, quasi-planar waveguides are slightly birefringent due to different boundary conditions for TE and TM polarizations. Whereas such "form" birefringence is too weak to compensate dispersion in frequency conversion processes, it can be greatly enhanced by designing a waveguide with several index discontinuities.

In a periodic multilayer stack of isotropic materials, the existence of repeated discontinuities of the refractive index along one direction breaks the original 3 axes rotation symmetry of the constituent media and results in a macroscopic negative uniaxial crystal. With reference to the geometry described in Figure 1.11a, for plane waves in an infinitely extended

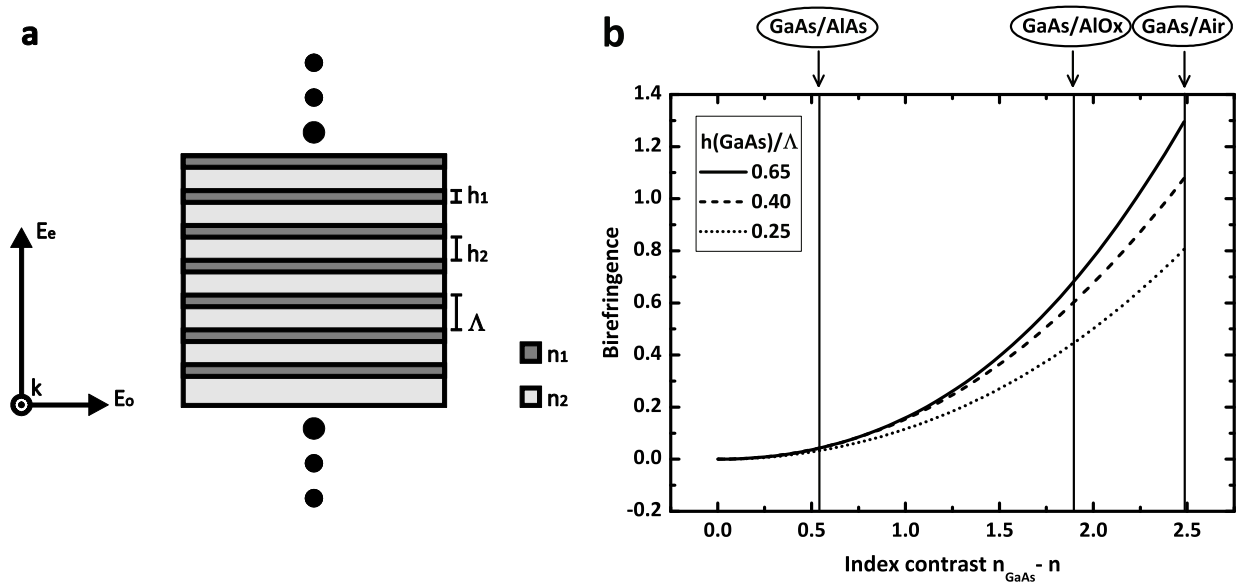

Figure 1.11 a) Scheme of a form birefringent multilayer periodic structure. b) Form birefringence, in plane-wave approximation, of a multilayer periodic structure of GaAs and a generic material of refractive index n, for three different duty cycles. The index contrasts corresponding to GaAs/AlAs, GaAs/AlOx, and GaAs/air combinations are pointed out.

medium, the ordinary and the extraordinary refractive index are equal to [Born, 1980; Yeh, 1988]:

$$\begin{cases} n_0^2 = \dfrac{h_1}{\Lambda} n_1^2 + \dfrac{h_2}{\Lambda} n_2^2 \\ \dfrac{1}{n_e^2} = \dfrac{h_1}{\Lambda}\dfrac{1}{n_1^2} + \dfrac{h_2}{\Lambda}\dfrac{1}{n_2^2} \end{cases} \tag{1.35}$$

where n_i and h_i are the refractive index and the thickness of the i*th* (i = 1, 2) repeated layer, and Λ the period ($h_1 + h_2 = \Lambda << \lambda$). The corresponding form birefringence $\Delta n = n_o - n_e$ depends on the duty cycle and the index contrast, as shown in Figure 1.11b for a periodic structure alternating GaAs with a lower index material.

Form birefringent PM was firstly proposed in multilayer AlGaAs structures, with a birefringence suitable to obtain SHG in the MIR, for instance from a CO_2 (λ = 10.6 μm) pump laser. [Ziel, 1975; Ziel, 1978] As maximum birefringence obtained by GaAs/AlAs index contrast is not sufficient to compensate dispersion near the forbidden band, NIR phase matching is not accessible with these materials. The scenario changed in the early 90's with the demonstration of selective wet oxidation of AlAs layers embedded in GaAs. [Dallesasse, 1990a] This technique,

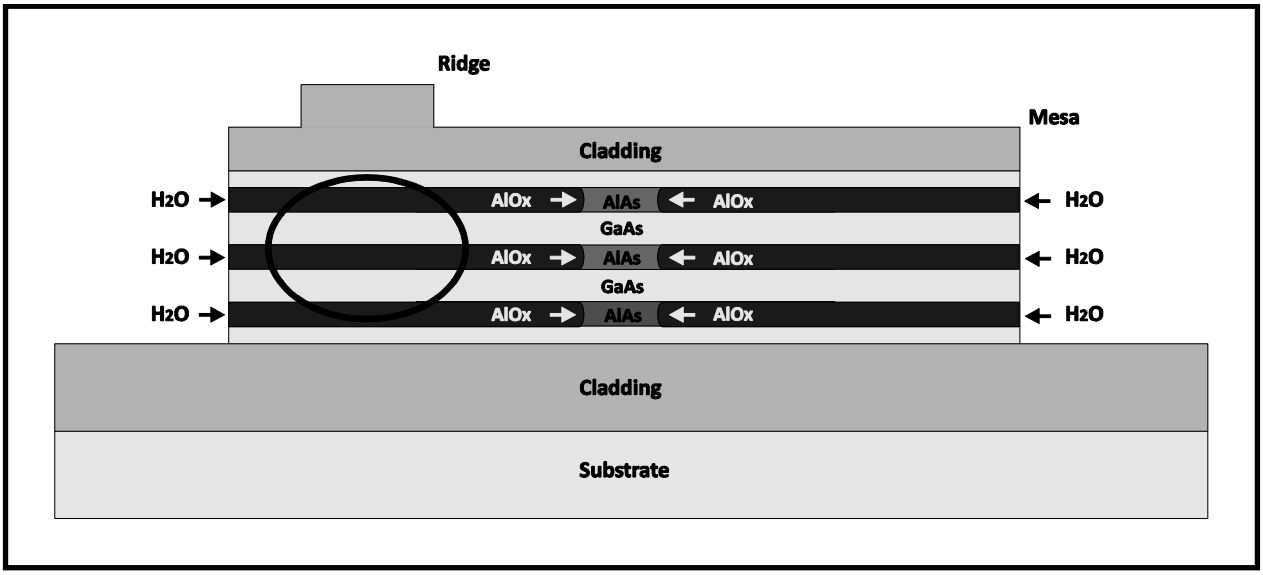

Figure 1.12 Double-etched structure for optical confinement and oxidation in GaAs/AlOx waveguides.

was adopted by Fiore et al. one decade ago at Thomson CSF (today Thales) to fabricate integrated frequency converters based on a multilayer core alternating GaAs (n = 3.4) and AlOx (n = 1.6). [Fiore, 1998b]

After MBE[19] growth of a GaAs/AlAs multilayer structure, oxidized waveguides were obtained through two etching steps (Figure 1.12): the first etching defined a 3 to 9 μm wide ridge for lateral confinement; the second etching defined 100 μm wide mesa for lateral oxidation. After selective oxidation of AlAs layers, a birefringence as high as 0.2 was obtained in the NIR. With this type of waveguide, several nonlinear interactions have been demonstrated:

- Type I DFG from a CW tunable TM polarized Ti:Sapphire laser at 1 μm and a CW TE polarized Nd:YAG laser at 1.3 μm, producing a temperature-tunable TE field within 5.2 μm and 5.6 μm (Figure 1.13). MIR power as high as 120 nW was achieved with 17 mW and 0.4 mW of pump and idler power, respectively; [Bravetti, 1998]
- Type I SHG from either a CW dye-laser pump at 1.6 μm and a femtosecond pulsed OPO pump at 2.1 μm. In the former case, an efficiency $\eta = 0.12\%\ W^{-1}$ was obtained in a 1.7 mm waveguide. [Fiore, 1998a] In the latter case, a normalized efficiency $\eta_{norm} \approx 1000\%\ W^{-1}\,cm^{-2}$, very near to the theoretical value, was inferred. However, due to group velocity dispersion, the effective interaction length was shorter than 200 μm, with an overall efficiency $\eta = 0.1\%$

[19] Molecular Beam Epitaxy.

W^{-1}; [Moutzouris, 2001]

- Type I parametric fluorescence with a Ti:Sapphire CW TM pump at 1.06 μm in a 3.2 mm long waveguide, with a conversion efficiency $\eta_{PF} = P_S/P_P = 6 \cdot 10^{-7}$ at degeneracy and a maximum parametric gain coefficient g = 0.4 cm^{-1}; [De Rossi, 2001]

The weak point of this approach, which has made GaAs an outstanding solution for guided-wave frequency conversion, and a serious $LiNbO_3$ competitor, are the high propagation losses. They severely limited the conversion efficiency in most of the works just mentioned. Early-stage, still immature processing resulted in attenuation coefficients one and two order of magnitude higher than in unoxidized GaAs waveguides and in $LiNbO_3$ low-loss waveguides, respectively. Oxidized layers, and in particular the roughness at the interfaces with the adjacent GaAs layers, are the main factor affecting the attenuation coefficient in form birefringent waveguides.

GaAs/AlOx system was recently employed at Stanford University with a different design strategy, in small core waveguides, for SHG pumped at 1.55 μm. [Scaccabarozzi, 2006] The intrinsically strong birefringence of these waveguides[20] was further increased by the introduction of one 90 nm thick AlOx layer at the center of the guiding core (Figure 1.14). This configuration results in an impressive calculated normalized conversion efficiency η_{norm} =

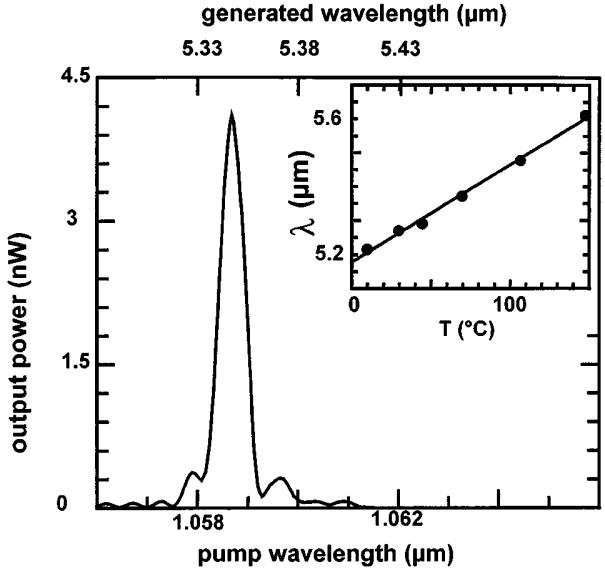

Figure 1.13 Experimental detuning curve for MIR DFG in a GaAs/AlOx waveguide. Inset: experimental temperature tuning curve (from Ref. [Bravetti, 1998]).

[20] For a given refractive-index step, the smaller the core section of the waveguide, the higher is the modal field intensity at the boundaries with the claddings and the consequent modal birefringence.

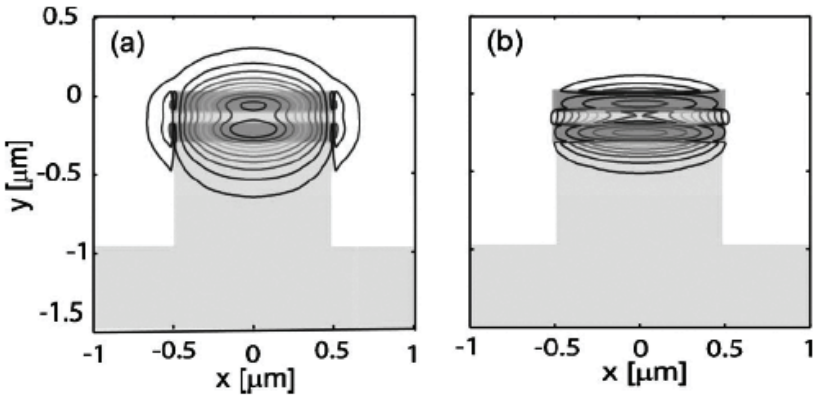

Figure 1.14 AlGaAs/AlOx birefringent waveguide for SHG from 1.55 μm from Ref. [Scaccabarozzi, 2006]. Profiles of the phase-matched modes: TE_{00} at λ = 1.55 μm (a) and TM_{00} at $\lambda/2$ (b). The very tight confinement of this device, at both ω and 2ω, results in a huge field intensity and a subsequent high nominal conversion efficiency. On the other hand, the considerable overlap of the modes with all the waveguide interfaces results in scattering losses higher compared to the approach of Fiore et al. [Fiore, 1998b]

20000% W^{-1} cm^{-2}. However, in spite of the short waveguide length (600 μm), the measured value was only η_{norm} = 1100% W^{-1} cm^{-2}, because of very high propagation losses (2.3 dB/mm at 1550 nm and 25-35dB/mm at 775 nm).

1.2.5 OP-AlGaAs waveguides

Early experiments in AlGaAs nonlinear optics addressed phase matching by assembly of QPM media from stacked plates polished to the coherence-length thicknesses. [Thompson, 1976] However, these methods never found widespread use, due to difficulties in fabrication to the required tolerances, and the high losses associated with the many interfaces between the high-index plates and air. Elimination of these interfaces through diffusion bonding the stack into a single block reduced the interface losses, but difficulties with fabrication to the required tolerances remained. [Zheng, 1998]

A current method for microstructuring semiconductors for QPM is orientation-patterned (OP) growth. In these approach, a template substrate is patterned lithographically to control the crystallographic orientation of subsequently grown films. Multilayer thin-film (microns) growth then produces a QPM waveguide; thick-film (≈ 1mm) growth produces a bulk QPM medium.

One of the first accomplishments of OP-GaAs growth was based on diffusion bonding two [100] GaAs wafers, rotated 90◦ around [100] with respect to each other. After a selective

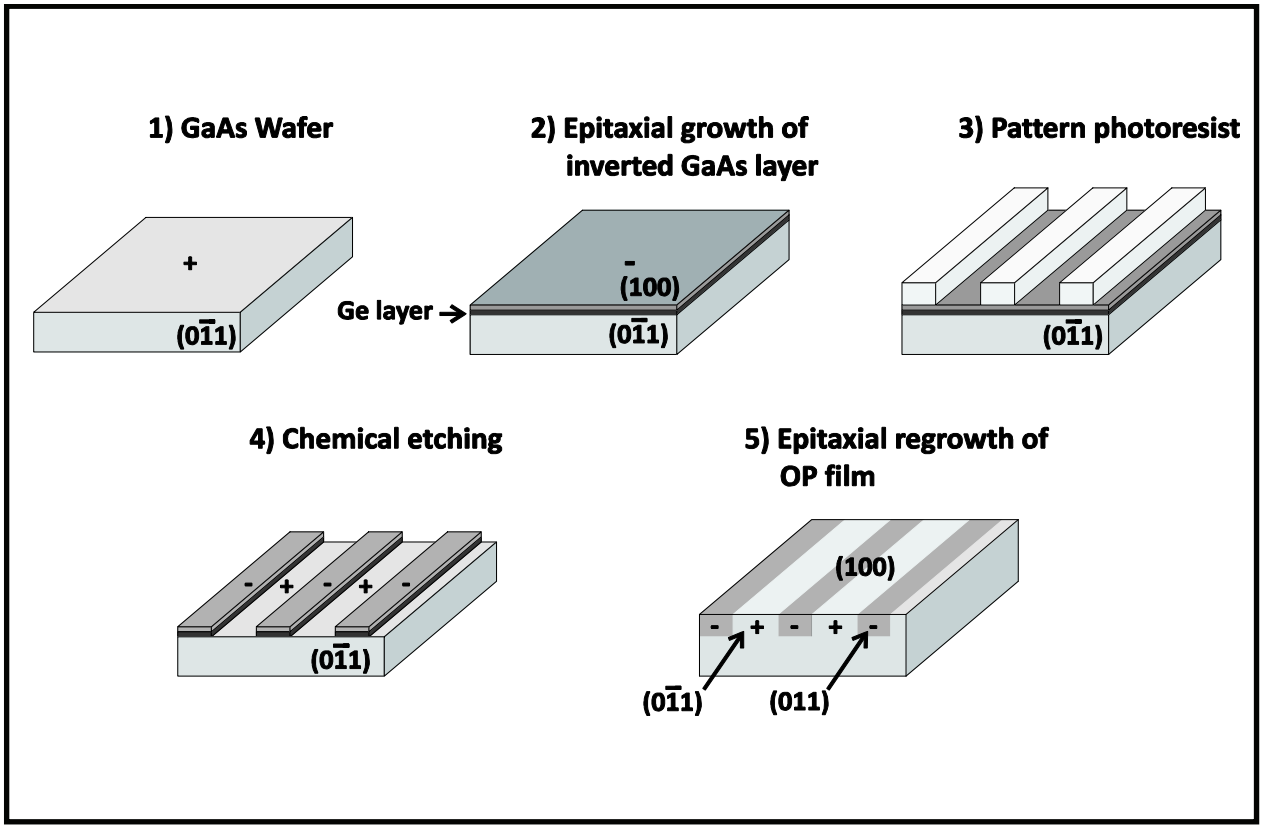

Figure 1.15 Sketch of process flow for fabrication of OP-GaAs by GaAs/Ge heteroepitaxy.

etching, only a thin film with orientation rotated by 90◦ was left behind on the other wafer, which could then be lithographically patterned to form the orientation template. QPM type II SHG have been demonstrated in AlGaAs waveguides based on this method: a 1.54 μm laser was doubled with an efficiency $\eta = 0.12\%\ W^{-1}$ in a 3 mm long device. [Yoo, 1995] The gap between such value and the calculated efficiency was ascribed to huge scattering losses (5 dB/cm at ω and 25 dB/cm at 2ω) and to unequal domain sizes.

Today, the most widely used templates are based on lattice-matched heteroepitaxy of GaAs/Ge films on GaAs substrates. Such templates are obtained by the MBE growth of a thin Ge layer that allows the subsequent growth of a thin GaAs layer with rotated orientation with respect to the substrate. Afterwards, the two layers are periodically patterned with a lithographic step (Figure 1.15). The growth of thick GaAs films by hydride vapor phase epitaxy on such templates results in GaAs bulk crystals with losses as low as 0.01 cm^{-1}. [Eyres, 2001] A long series of impressive frequency conversion demonstrations has followed the advent of this technology, e.g.: SHG, [Skauli, 2002] OPO, [Vodopyanov, 2004] THz generation. [Vodopyanov, 2006]

The MBE growth of thin AlGaAs multilayers on such templates has recently allowed the demonstration of guided-wave QPM SHG. [Yu, 2005] With a CW 1.55 pump, a normalized conversion efficiency η_{norm} = 92 % W^{-1} cm^{-2} was achieved. The discrepancy with the calculated efficiency, η_{norm} = 500% W^{-1} cm^{-2}, arises once again from high propagation losses. Indeed, unlike their bulk counterpart, waveguides based on OP-GaAs are heavily affected by scattering losses due to waveguide corrugation at the inverted domain boundaries. An attenuation coefficient of 6-7 dB/cm at ω and 13-15 dB/cm at 2ω was reported.

1.2.6 Counter-propagating phase matching

As a last example of guided-wave PM scheme, we present in this section a peculiar geometry, which relies on the interaction of two counterpropagating modes. In order to describe this configuration, we consider for simplicity the case of SHG: as illustrated in Figure 1.16, two counterpropagating modes at ω generates, via the waveguide nonlinearity, a field at 2ω radiating from the waveguide upper surface. The out-of-plane propagation angle of the surface-emitted SHG (SESHG), is set by the phase-matching condition on the waveguide axis

$$k_1(\omega) - k_2(\omega) \equiv \frac{2\pi}{\lambda}[n_1(\lambda) - n_2(\lambda)] = k_3(2\omega)\sin(\vartheta) \equiv \frac{4\pi}{\lambda}\sin(\vartheta) \tag{1.36}$$

where λ is the pump wavelength and n_1, n_2 the effective indices of the counter-propagating modes. As θ depends only on λ and on the difference n_1 - n_2, SESHG can be exploited to investigate some parameters of the waveguide, in particular modal birefringence (see Chapter 5). Note that, if the modes are identical, i.e. n_1 = n_2, the SH radiates orthogonally to the waveguide surface. While PM is always fulfilled along z, due to θ adaptability, the interaction is not phase matched in the vertical direction, where the nonlinear polarization has a constant phase, while the SH is a traveling wave. The resulting coherence length along x

$$L_c = \frac{\pi}{k_3(2\omega)\cos(\vartheta)} = \frac{\lambda}{4\cos(\vartheta)} \tag{1.37}$$

limits the maximum conversion efficiency. This is attainable for a thickness of the guiding film ≈ L_c, while for a much larger thickness the conversion efficiency vanishes.

SESHG was firstly obtained in Ti:$LiNbO_3$ waveguides, [Normandin, 1979] and ten years later in GaAs waveguides. [Vakhshoori, 1988; Fiore, 1997b] Semiconductor waveguides are

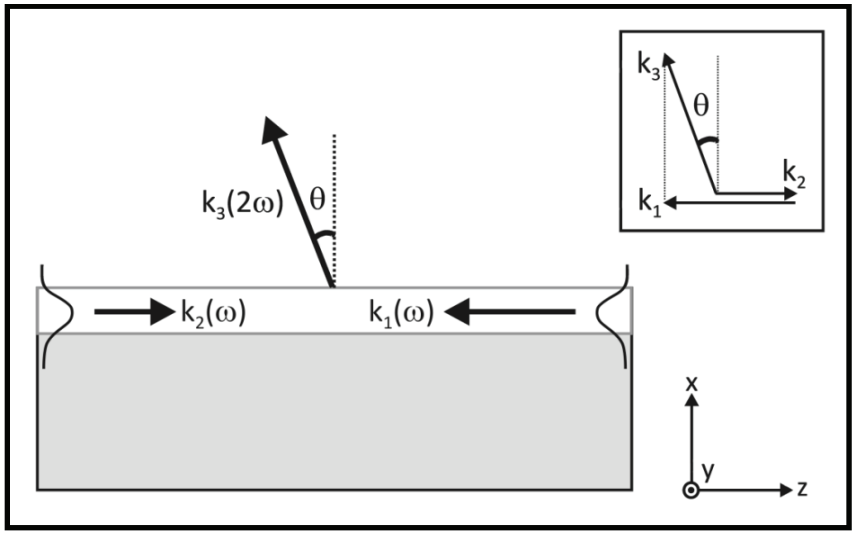

Figure 1.16 Scheme of surface emitting SHG. Inset: diagram of momentum conservation along the waveguide axis.

especially suitable for SESHG, as in this devices PM can be attained also along x. Indeed, a QPM grating can be fabricated in this direction by growing a multilayer waveguide alternating alloys with different nonlinear coefficients. Thanks to this approach, a conversion efficiency of 5×10^{-5} W^{-1} was reported by Janz et al. [Janz, 1998].

The conversion efficiency of this interaction can be calculated starting from the nonlinear polarization induced by the modes at ω. For a planar waveguide:

$$P_{2\omega}(x) = 2\varepsilon_0 d_{eff}(x) E_1 \phi_1(x) E_2 \phi_2(x) \tag{1.38}$$

where $\phi_1(x,y)$, $\phi_2(x,y)$ are the normalized modal distributions and E_1, E_2 the modal amplitudes. Each polarization plane dx radiates an electric field at 2ω towards the substrate and the waveguide top surface. Integration along x of all the contributions gives the overall emitted intensity at 2ω. In the case of multilayer semiconductor waveguides, the calculations are more complex, as the radiating SH undergoes multiple reflections before reaching the surface. In this case, the contribution of each layer can be calculated with transfer matrix methods. [Whitbread, 1994] The SESHG power P_3 is then obtained by integrating the radiated intensity on the waveguide area, w × L (w width, L length). The resulting conversion is efficiency is conventionally expressed through a nonlinear cross-section, defined as $A_{nl} = P_3/(P_1P_2)(w/L)$. A_{nl} accounts only for the conversion efficiency of the multilayer structure, independently of the ridge size. The value reported by Janz et al. was $A_{nl} = 2\times10^{-6}\,W^{-1}\,cm^{-1}$ mm.

Counter-propating PM can be employed also for different $\chi^{(2)}$ processes, e.g. for spontaneous or seeded down-conversion. In this case, a pump beam impinging on the waveguide upper surface generates a parametric gain for a pair of counter-propagating modes (this configuration will be detailed in Chapter 5).

2 Form-birefringent nonlinear waveguides: design and fabrication

In this work, I have pursued the goal of reducing GaAs/AlOx waveguides losses through design optimization and, above all, technological development. In this Chapter I will present my work and the results achieved in these directions. The project guidelines that have led to define a birefringent guiding structure for parametric generation are detailed in Section 2.1, along with a complete description of the final project features. Section 2.2 is dedicated to the description of fabrication and processing. Section 2.3 describes the technique adopted to characterize the final devices in terms of propagation losses, and reports the advancements obtained.

2.1 Device project and expected performances

The main criterion for the design of a form birefringent nonlinear waveguide is to obtain a guiding structure where form birefringence exactly balances overall (material+waveguide) dispersion for the fundamental modes at the frequencies involved. As previously stated, our goal is to obtain parametric down-conversion starting from a 1 μm pump field. According to GaAs selection rules for waveguides grown on standard (001) GaAs substrates, second order nonlinear interactions are only possible between a combination of two TE modes and a TM mode. As form birefringence results in a lower refractive index for the polarization orthogonal to the layers plane, i.e. TM, the only possible PM scheme in this geometry is a type I with a TM polarized pump. The phase-matching condition for parametric generation at degeneracy reads

$$n_{TM_0}(1\mu m) = n_{TE_0}(2\mu m) \tag{2.1}$$

which implies that birefringence at 1 μm must compensate TE_0 overall dispersion between 1 μm and 2 μm:

$$\underbrace{n_{TE_0}(1\mu m) - n_{TM_0}(1\mu m)}_{\text{Birefringence}} = \underbrace{n_{TE_0}(1\mu m) - n_{TE_0}(2\mu m)}_{\text{Dispersion}} \tag{2.2}$$

2.1.1 Vertical structure design

Besides achieving the required birefringence, further guidelines followed for the multilayer waveguide design are:

- maximizing the nonlinear overlap integral: in order to improve the efficiency of a frequency conversion process, interacting modes must have similar field distributions with as-high-as-

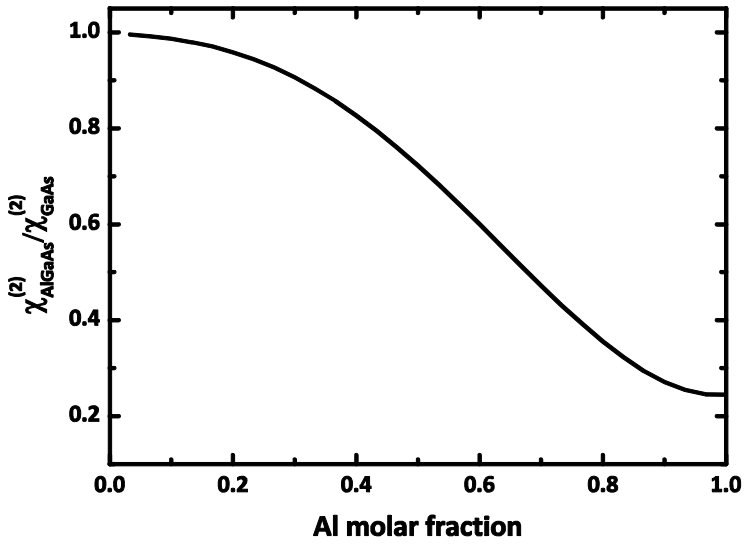

Figure 2.1 Normalized AlGaAs nonlinear coefficient as a function of Al molar fraction, extrapolation from experimental data (from Ref. [Ohashi, 1993]).

possible peak intensities. In addition, in AlGaAs waveguides, Al content must be minimized, as AlGaAs $\chi^{(2)}$ strongly decreases with the Al content (Figure 2.1). In other words, the interacting modes must be well confined in a GaAs guiding core, and exhibit a poor overlap with the Al-rich claddings. Moreover, in the case of GaAs/AlOx waveguides, AlOx content has to be minimized, since its bulk nonlinear coefficient is zero.

- minimizing the propagation losses: AlOx layers are the main cause for propagation losses in GaAs/AlOx waveguides, because of roughness at the interfaces with contiguous crystalline layers; their number must be kept small. Field intensy at the interface with air must be minimized as well: those modes that do not satisfy this condition experience strong scattering due to surface roughness and exhibit high attenuation coefficients.
- reducing the amount of guided modes at pump wavelength, to avoid distributing the injected pump on non phase-matched higher-order modes.
- avoiding unintentional oxidation: wet oxidation is not limited to AlAs but concerns in general AlGaAs with high Al content. [Dallesasse, 1990a; Dallesasse, 1990b] In order to avoid this process, layers that are not supposed to be oxidized must have an Al content lower than a certain value, depending on the layer thickness. (see Section 2.2.2)
- setting the thickness of AlOx layers between 10 and 300 nm, because of the technological constraints detailed in Section 2.2.2.

Design work has been carried out with the aid of one-dimensional (1D) simulations: the

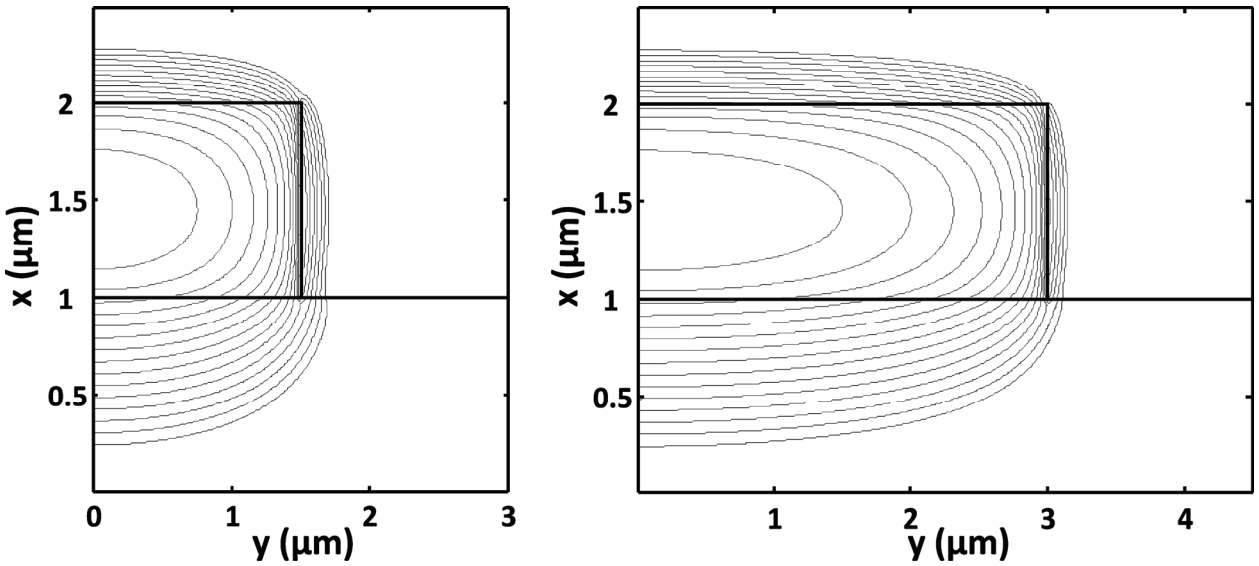

Figure 2.2 TE_{00} modal profiles at 1.55 μm of the waveguide [GaAs (substrate), $Al_{0.7}Ga_{0.3}As$, 1000 nm GaAs, air]: for a 3 μm wide, 1 μm high ridge (left); and for a 6 μm wide, 1 μm high ridge (right). The effective indices are n_{eff} = 3.3091 and n_{eff} = 3.3165, respectively, while for the TE_0 mode of the 1D structure n_{eff} = 3.3190.

transfer matrix method [Yeh, 1988] has been used to calculate the waveguides eigenvalues and eigenfunctions. The former are required to verify the phase-matching condition, while the latter to calculate the nonlinear overlap integral. Thanks to a considerable reduction in computing time, 1D modeling is of invaluable usefulness for the design of multilayer waveguides, especially when extensive calculations of the effective indices are required. If modal distributions are much wider in the horizontal than in the vertical direction (see Figure 2.2), neglecting the effects of lateral confinement does not imply a considerable loss of accuracy. Still, even if lateral confinement is tight and 2D simulations become substantially more accurate, it is advantageous to resort to 1D modeling, able to provide qualitative indications that can be successively validated or corrected by means of an exact method. AlGaAs refractive indices have been calculated resorting to the Afromovitz dispersion model. [Afromovitz, 1974] For AlOx, whose forbidden energy is in the ultraviolet (UV), a constant refractive index of 1.6 has been adopted. [Durand, 2003]

We have started the waveguide design from the basic vertical profile shown in Figure 2.3: a thick GaAs core included between two thick $Al_{0.7}Ga_{0.3}As$ claddings.[21] Then we have introduced thin AlOx layers in the GaAs film to increase FB until it compensates the overall

[21] For a 1 μm thickness, we estimate 70% as the highest Al molar fraction not subject to oxidation.

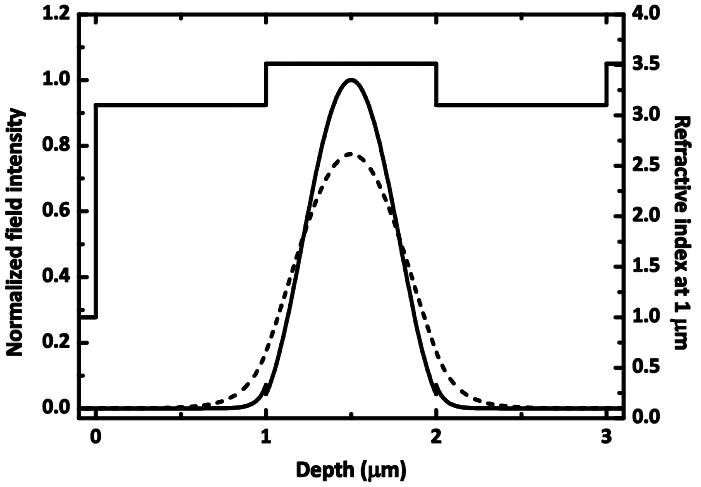

Figure 2.3 Basic guiding structure for FB parametric generation, before AlOx layers introduction: refractive index profile (solid line), TM_0 (dotted line) and TE_0 (dashed line) modal profiles at 1 μm and 2 μm respectively.

dispersion (≈ 0.21) between 1 μm and 2 μm. In the following, the procedure that has led to establish the exact structure of the AlOx/GaAs multilayer core will be briefly described.

In plane-wave approximation, for a given index contrast, FB depends only on the filling factor of the two media. According to Eq. 1.35, with an index contrast n_{GaAs}-n_{AlOx}, a maximum FB ≈ 0.7 is attainable, for an AlOx thickness $h_1 \approx 0.4\ \Lambda$. However, in the case of our guided-wave configuration some additional elements have to be taken into account. Firstly, the interacting mode confinement: the ratio h_1/Λ must be kept below a certain limit, much lower than 0.4, so that the resulting TM_0 effective index stays higher than the refractive index of $Al_{0.7}Ga_{0.3}As$ claddings. Secondly, the finite dimensions of the structure: the guiding core size, dictated by the overlap integral maximization, relates the number of repetitions and the period Λ. For a given core thickness (in our case $\approx 4\cdot\lambda/n_{eff}$), a reduction of AlOx layers number results in a larger period. This does not affect form birefringence as long as we stay in the long-wavelength approximation ($\lambda/n_{eff} >> \Lambda$), since FB is independent of Λ under this condition. Conversely, reducing the number of repetitions down to some units makes this approximation no more valid and results in a lower FB than that predicted by Eq. 1.35. The effects of these two constraints have been studied in a structure with six AlOx layers: Figure 2.4 shows the FB at 1 μm of the structure [GaAs (substrate), 1000 nm $Al_{0.7}Ga_{0.3}As$, h_1 AlOx, 5 × (h_2 GaAs , h_1 AlOx), 1000 nm $Al_{0.7}Ga_{0.3}As$, air], calculated vs. h_2/Λ for three different values of the AlOx thickness h_1. The three curves are traced down to the minimum value of h_2/Λ that assures a good

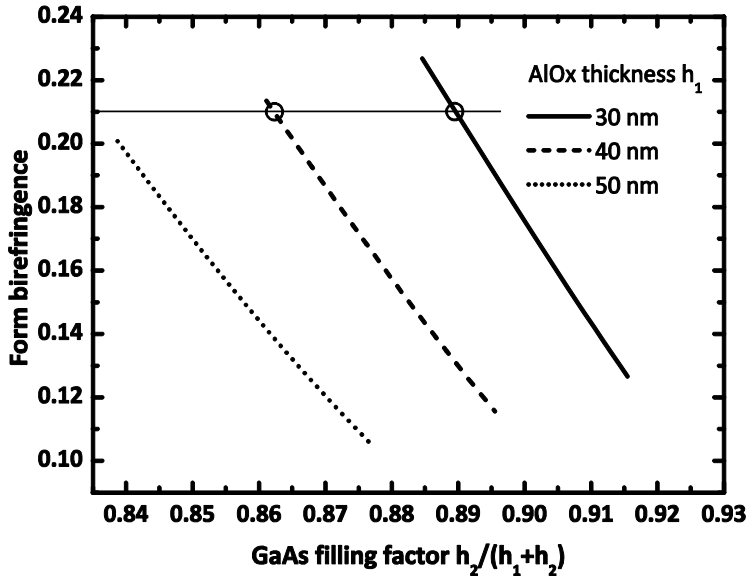

Figure 2.4 FB of guiding structure [GaAs (substrate), 1000 nm $Al_{0.7}Ga_{0.3}As$, h_1 AlOx, 5 × (h_2 GaAs , h_1 AlOx), 1000 nm $Al_{0.7}Ga_{0.3}As$, air] for three different values of h_1 as a function of the GaAs filling factor $h_2/(h_1+h_2)$.

confinement of the TM_0 mode at 1 μm: in all the cases the birefringence increases for lower h_2/Λ, until modal cut-off occurs. A FB n_{TE0}-n_{TM0} > 0.21, sufficient to compensate 1-2 μm dispersion is obtained with both h_1 = 30 nm and h_1 = 40 nm. We stress that in these structures we are not in the long wavelength regime ($\Lambda \approx \lambda/n_{eff}$): this is the reason why, for a given duty

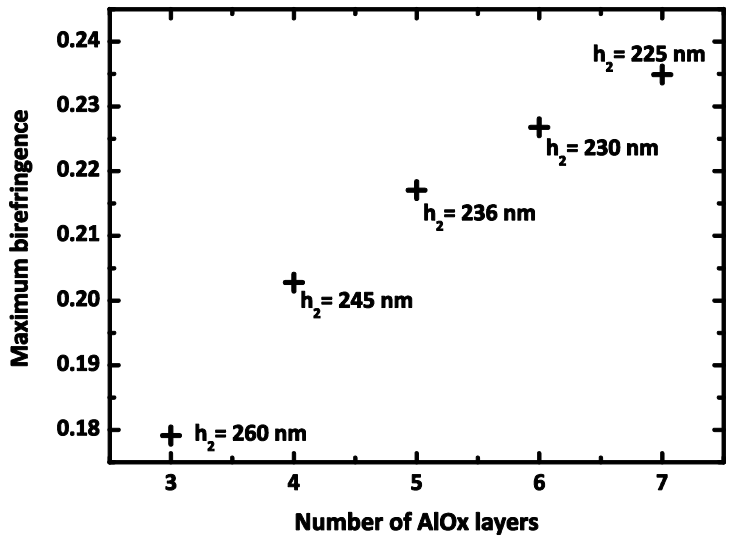

Figure 2.5 Maximum birefringence of the structure [GaAs (substrate), 1000 nm $Al_{0.7}Ga_{0.3}As$, 30 nm AlOx, n × (h_2 GaAs , 30 nm AlOx), 1000 nm $Al_{0.7}Ga_{0.3}As$, air] vs. AlOx layer number (n+1): the maxima are obtained in every case for the minimum thickness h_2 that assures a good TM_0 mode confinement.

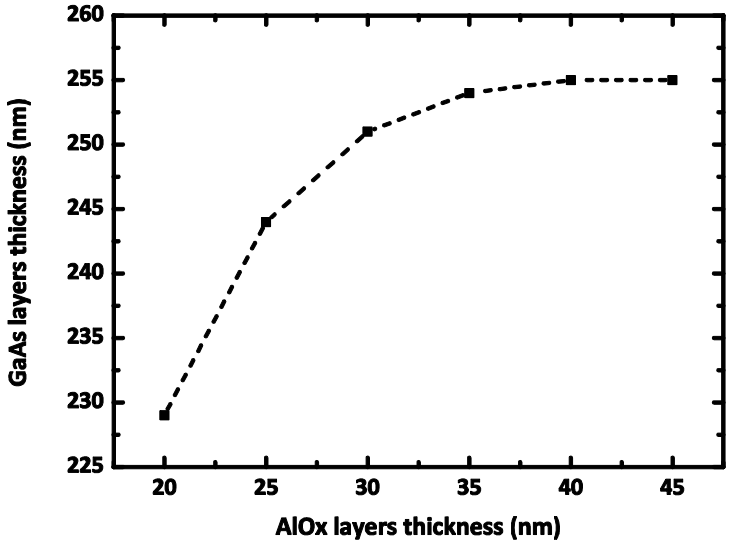

Figure 2.6 GaAs h_2 versus AlOx h_1 thickness in structure [GaAs (substrate), 1000 nm $Al_{0.7}Ga_{0.3}As$, h_1 AlOx, 4 × (h_2 GaAs , h_1 AlOx), 1000 nm $Al_{0.7}Ga_{0.3}As$] fulfilling the condition $n_{TM_0}(1.03\ \mu m) = n_{TE_0}(2.06\ \mu m)$.

cycle, birefringence is lower for higher h_1, i.e. for larger periods. In other words, with a small number of repetitions, a lower AlOx thickness allows combining a shorter period with a higher h_1/Λ ratio, resulting in a higher birefringence.

With thin AlOx layers, six repetitions have proved sufficient to fulfill our PM condition. On this basis, we have studied the minimum number of repetitions necessary to this purpose. Considering conservatively 30 nm as the technological lower limit for the AlOx layers thickness, we have calculated the maximum birefringence attainable for the structure [GaAs (substrate), 1000 nm $Al_{0.7}Ga_{0.3}As$, 30 nm AlOx, n × (h_2 GaAs , 30 nm AlOx), 1000 nm $Al_{0.7}Ga_{0.3}As$, air], vs. the number n of periods (Figure 2.5): the minimum number of AlOx layers to match the dispersion from 1 to 2 μm is 5 (i.e. n = 4). As the number of AlOx layers directly affects the waveguide transmission, we have chosen to employ this configuration for our devices. Resorting to a higher number of AlOx layers is necessary for frequency conversion closer to GaAs band gap, where a larger dispersion need be compensated for. [Fiore, 1998a]

The scheme with 5 AlOx layers has then been the object of further calculations, to precisely define the final waveguide vertical profile. In particular, we have designed two different multilayer structures, "A" and "B", with degeneracy at a pump wavelength of 1.03 μm and 1.064 μm, respectively. Figure 2.6 shows the relation between the thicknesses of GaAs and AlOx layer which results in the former PM wavelength. These data have lead to the final design

of structure A, detailed in table 2.1

	Composition	Thickness (nm)
	GaAs	Substrate
	$Al_{0.92}Ga_{0.08}As$	1000
	$Al_{0.7}Ga_{0.3}As$	1000
	AlOx	33
4 X	GaAs	255
	AlOx	33
	$Al_{0.7}Ga_{0.3}As$	1000
	GaAs	30

Table 2.1 Multilayer epitaxial structure A.

Multilayer B has the same structure, except for the thickness of GaAs layers, 273 nm. The characteristics of the two devices are basically identical, with the exception of the slight tuning shift. In the following, unless otherwise stated, we will refer to structure A.

2.1.2 Tuning and efficiency: expected performances

The refractive index vertical profile is shown in Figure 2.7 along with the TM_0 and TE_0 vertical modal profiles at 1.03 μm and at 2.06 μm, respectively. Lateral confinement is obtained by means of ridges, usually 3 μm wide, wet etched in (110) direction (Figure 2.8).

As shown in Figure 2.9, the generated signal and idler wavelengths can be tuned on a wide spectral region by reducing the pump wavelength with respect to degeneracy. Compared to typical bulk nonlinear crystals, wavelength tuning in our geometry is highly sensitive to pump wavelength. This peculiarity stems from the huge waveguide dispersion at λ_p, much larger than at $2\lambda_p$, as clarified by the approximated expression for the relationship between λ_p, λ_I,and λ_S around degeneracy: [De Rossi, 2005b]

$$\lambda_{S,I} = \frac{2\lambda_P}{1 \pm \alpha\sqrt{\frac{\lambda_P^0}{\lambda_P} - 1}} \tag{2.3}$$

where the "aperture" α of the tuning curve is given by

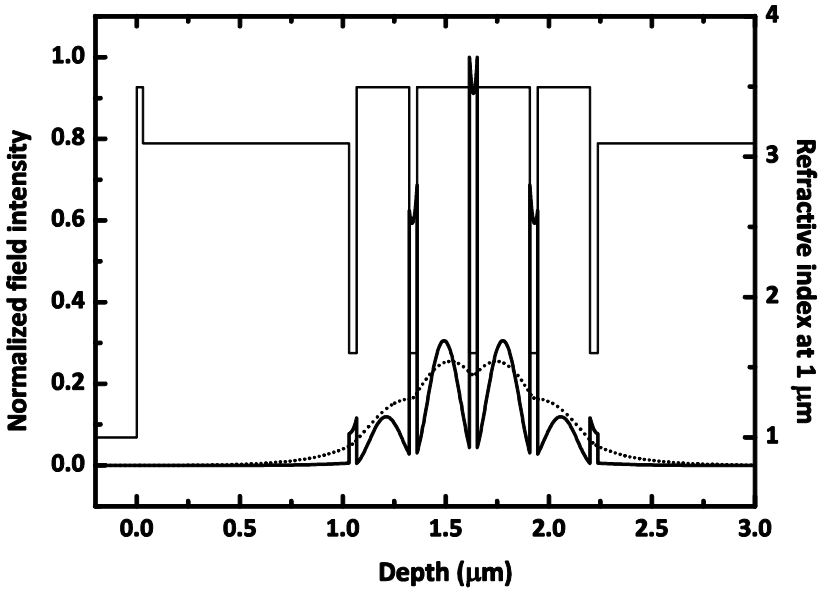

Figure 2.7 Vertical structure of the FB parametric generator A: refractive index (thin solid line), TM_0 (thick solid line) and TE_0 (dotted line) modal profiles at 1 μm and 2 μm, respectively.

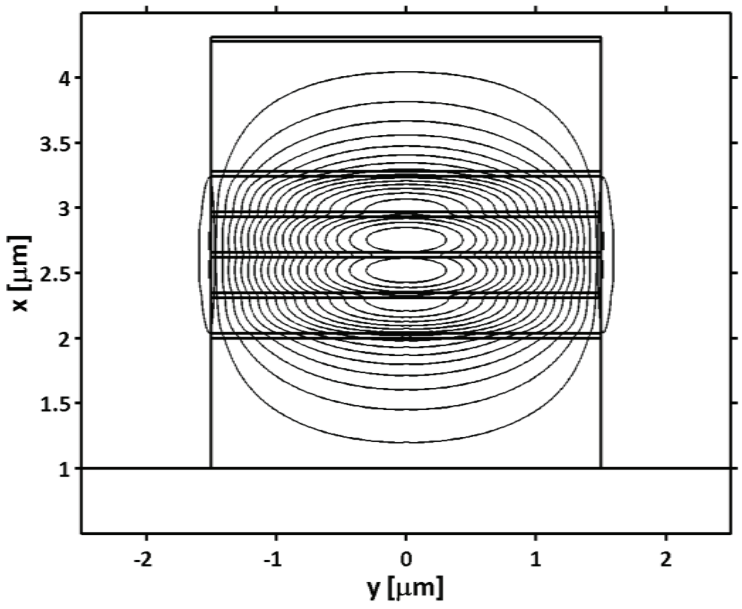

Figure 2.8 TE_{00} modal profile of the FB parametric generator at 2 μm for a ridge width of 3 μm.

$$\alpha = \sqrt{\frac{\frac{\partial n_{TM_0}}{\partial \lambda}\left(\lambda_P^0\right)}{2\frac{\partial n_{TE_0}}{\partial \lambda}\left(\lambda_S^0\right)} - 1} \tag{2.4}$$

In both expressions, the superscript 0 indicates values at degeneracy. Eqs. 2.3 and 2.4, which are obtained by neglecting the second-order derivatives of the effective indices, show how a

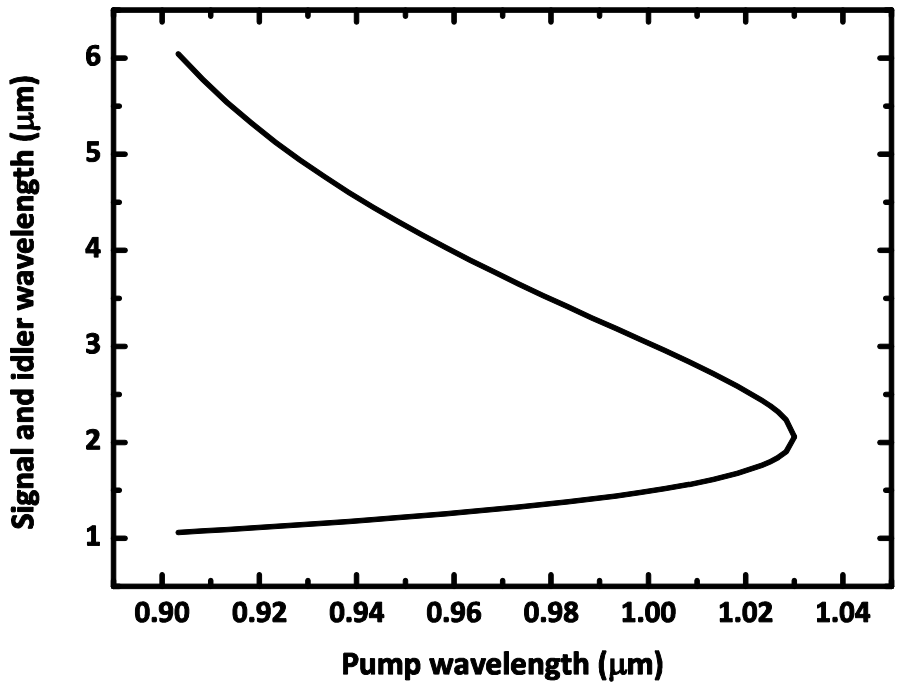

Figure 2.9 Parametric generation tuning curve (calculated).

higher ratio between $(\partial n_{TM_0} / \partial \lambda)_{\lambda_P^0}$ and $(\partial n_{TE_0} / \partial \lambda)_{\lambda_S^0}$ implies a wider aperture of the tuning curve.[22] A wide aperture α is strongly desirable for a tunable source, especially in the perspective of integrating a pump laser diode, usually exhibiting limited tunability. In addition, waveguide strong dispersion leads to somewhat reduce the down-conversion PM bandwidth, typically much wider than in type II processes, especially at degeneracy. For a usual value of the waveguide length, 3 mm, we calculate a bandwidth of about 125 nm FWHM (full width at half maximum). As shown in Figure 2.10, this value abruptly decreases down to a few nanometers far from degeneracy.

While an advantage for tunability, the strong dispersion is a major drawback as far as the device fabrication is concerned. It implies a high sensitivity of the tuning curve to the variation of parameters like refractive indices, layer thicknesses, or ridge profile. [De Rossi, 2005b] In general: 1) the thickness of MBE grown layers can hardly be kept more accurate than 1%; 2) the width and the depth of wet-etched ridges exhibit a poor reproducibility and are affected by fluctuations along the propagation direction, in each waveguide. In addition,

[22] A similar behavior is found for temperature tuning as well, due to the great difference between the thermorefractive coefficients $(\partial n_{TM_0} / \partial T)_{\lambda_P^0}$ and $(\partial n_{TE_0} / \partial T)_{\lambda_P^0}$. Signal and idler can cover a 0.3 μm interval around 2 μm, with a temperature shift of 10 C°.

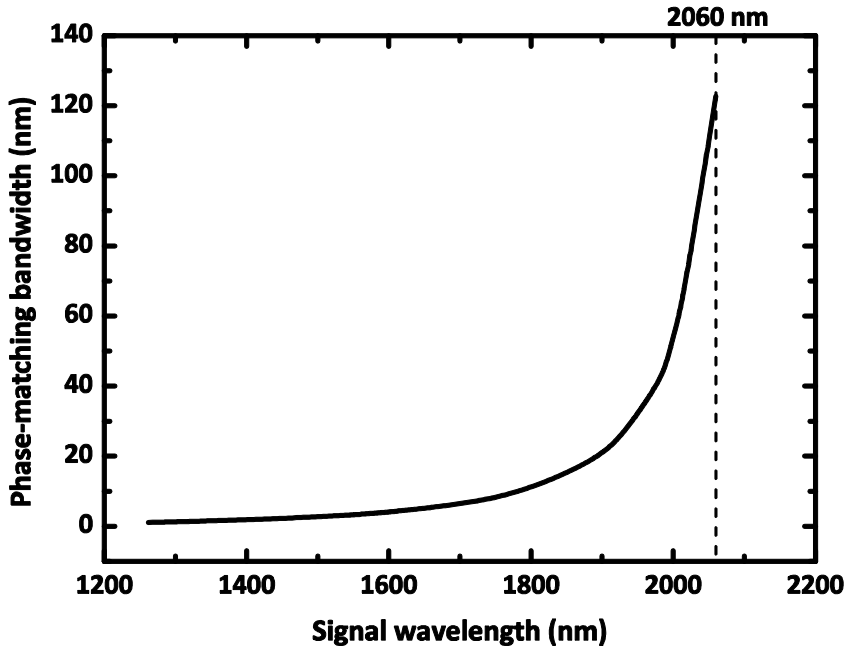

Figure 2.10 Signal phase-matching bandwidth versus wavelength for an interaction length L = 3 mm (as obtained by PM spectra calculation).

GaAs/AlOx form-birefringent waveguides are affected by further severe uncertainties. AlOx dispersion has not been modeled yet with a precision adequate to the design of optoelectronic devices. This is mostly because its structure, and consequently its optical properties, critically depend on the oxidation process. Moreover, AlAs layers are found to contract during oxidation: although this behavior is commonly reported in literature, the contraction has not been unambiguously evaluated and seems to depend on the oxidation conditions as well. In the following, we will analyze quantitatively the influence on the tuning curve of the uncertainty on refractive indices, layers thickness, and ridge profile.

Form birefringence, as shown in Section 1.2.4, is strongly dependent on the refractive index contrast of the multilayer. While GaAs dispersion has been extensively modeled and offers a satisfactory accuracy for our purposes nowadays, the exact determination of AlOx refractive index is far from being achieved and in general a 5% tolerance on the predicted values has to be accounted for. [Hall, 1999; Knopp, 1998; Durand, 2003] However, in our waveguides, an AlOx refractive index n_{AlOx} = 1.60 ± 0.005 was inferred from effective-index measurements. [Durand, 2003] Figure 2.11 reports the shift of the tuning curve in such n_{AlOx} range: as expected, lower values of n_{AlOx} increase FB and shift the curve toward lower pump wavelengths, where dispersion is stronger.

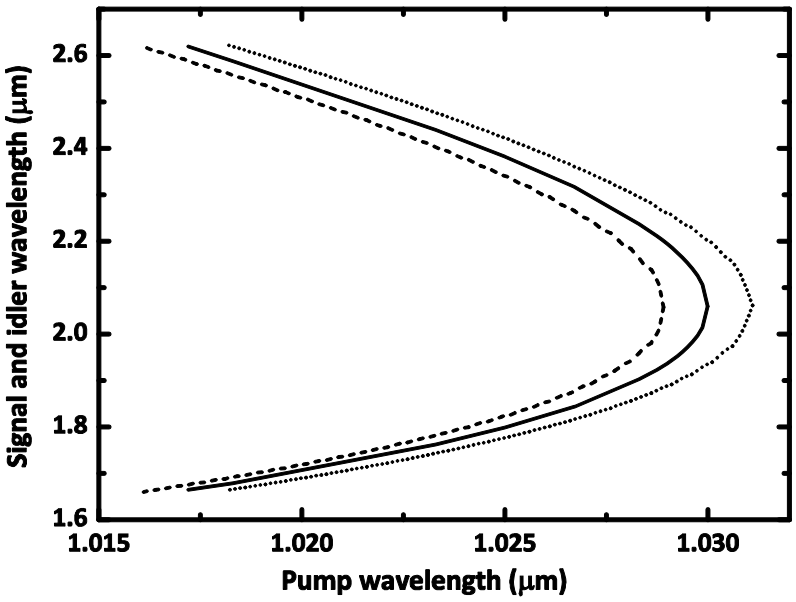

Figure 2.11 Tuning curves for AlOx refractive indices of 1.595 (dashed line), 1.6 (solid line) and 1.605 (dotted line).

The main element of uncertainty associated with epitaxial growth is the thickness of GaAs and AlOx layers. As the interacting modes are strongly confined, the thickness and the composition of the $Al_{0.7}Ga_{0.3}As$ claddings do not exhibit a strong influence on their effective indices. Conversely, the thickness of GaAs layers has a strong impact on the tuning curve, as shown in Figure 2.12: a variation of just 1% with respect to the nominal value shifts the degeneracy pump wavelength of 5 nm. On the other hand, this parameter can be exploited to design waveguides with different degeneracy wavelengths, as has been done in structure B, shifting λ_P^0 from 1.03 μm to 1.064 μm. The thickness of oxidized layers is by far less critical, as shown in Figure 2.13: due to a small overlap with the guided modes, variations of AlOx thickness induce small effective indices changes, especially in TE polarization, and a very limited shift of the tuning curve. With reference to AlOx contraction during oxidation, this turns out to be a considerable advantage.

All numerical results concerning PM condition presented up to here have been obtained with 1D effective-index calculations. In addition, in case of tight lateral confinement the effective indices dependence on the transverse ridge shape must be taken into account, for several reasons. Firstly, to evaluate the changes that this induces in the 1D tuning curve, so that they can be anticipated by modifying the vertical structure. Secondly, to correct a tuning curve

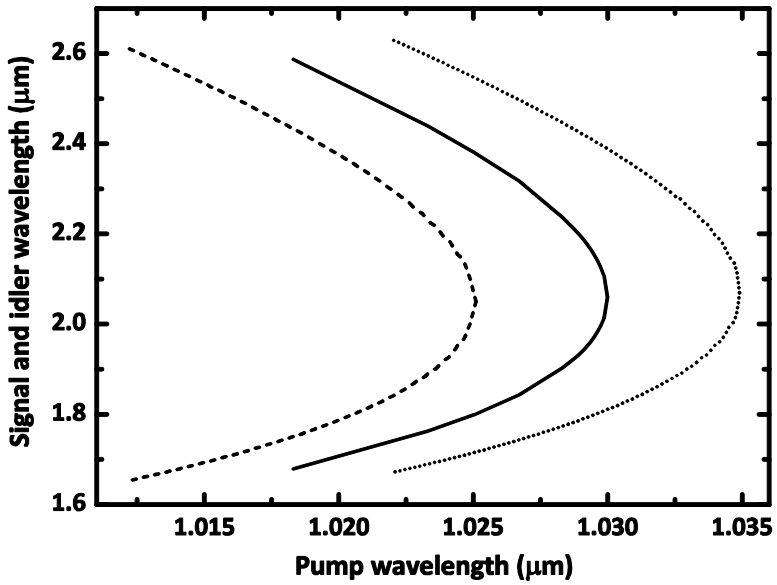

Figure 2.12 Tuning curves for GaAs thickness = 230 nm (solid line), 232 nm (dotted line), and 228 (dashed line).

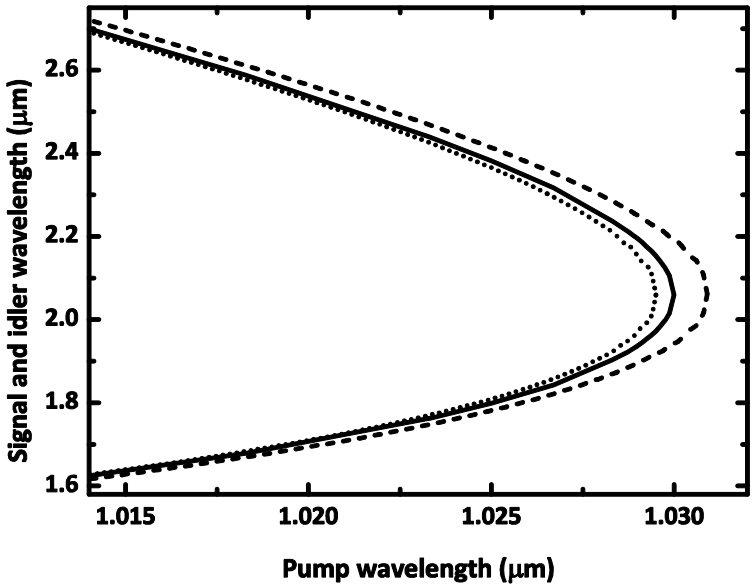

Figure 2.13 Tuning curves for AlOx thickness = 33 nm (solid line), 35 nm (dotted line), and 31 nm (dashed line).

shift due to a growth inaccuracy by means of an appropriate ridge design. Thirdly, to estimate the broadening of the PM resonance arising from the lack of etching uniformity along the propagation direction. The introduction of lateral confinement lowers the effective indices, especially those of long-wavelength signal and idler modes. Hence, a narrow lateral guidance increases waveguide dispersion, inducing a shift of the tuning curve towards longer pump

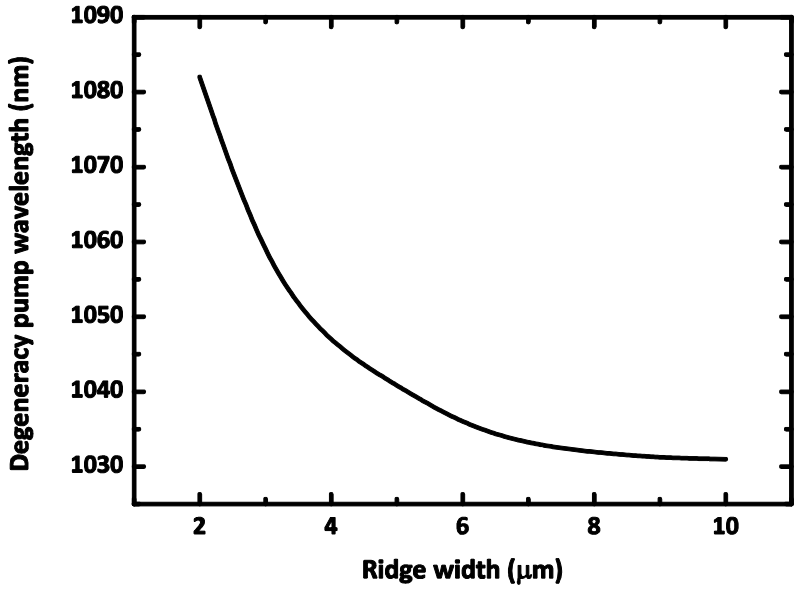

Figure 2.14 Degeneracy pump wavelength versus ridge width for an etching depth of 3 μm.

wavelengths. Figure 2.14 shows the results of 2D calculations of the phase-matching condition for a rectangular ridge profile: degeneracy wavelength is plotted versus ridge width for a fixed etching depth (3 μm). For ridge widths larger than 6 μm λ_p^0 stays essentially unvaried compared to the results of 1D calculations. Conversely, a narrower ridge results in a degeneracy shift towards longer wavelengths. We stress that the slope of the curve considerably increases for small width values. Accordingly, the narrower the ridge, the larger the PM band broadening following from ridge width fluctuations along the propagation direction.

Along with tunability, the other key feature of a waveguide for parametric generation is the nonlinear conversion efficiency. In guided-wave geometry this feature depends not only on the medium nonlinearity, but also on the interaction effective area, determined by the modal nonlinear overlap integral (Eq. 1.31). For 3 μm wide rectangular ridges, at degeneracy, we calculate an effective area A_{eff} = 7.4 μm^2 for structure A and A_{eff} = 7.6 μm^2 for structure B. These values correspond to a normalized parametric gain coefficient $g/\sqrt{P}$ = 4.95 $cm^{-1}W^{-1/2}$ and $g/\sqrt{P}$ = 4.83 $cm^{-1}W^{-1/2}$, respectively. As described in Section 1.1.3, the parametric efficiency intrinsically depends on the interacting wavelengths: it is maximum at degeneracy and decreases as signal and idler split. Moreover, also the profiles of the interacting modes, and accordingly the effective area, are a function of the three wavelengths. In our case, in particular, the modal overlap is maximum at degeneracy and decreases as the idler moves

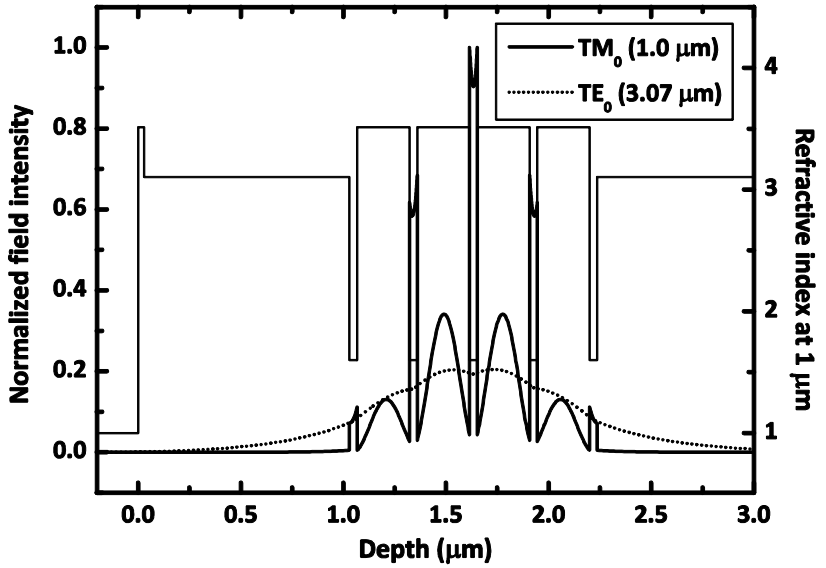

Figure 2.15 Pump and idler modal profiles far from degeneracy: as the idler wavelength grows, the corresponding modal profile gets broader and the overlap integral decreases (compare with Fig. 2.7).

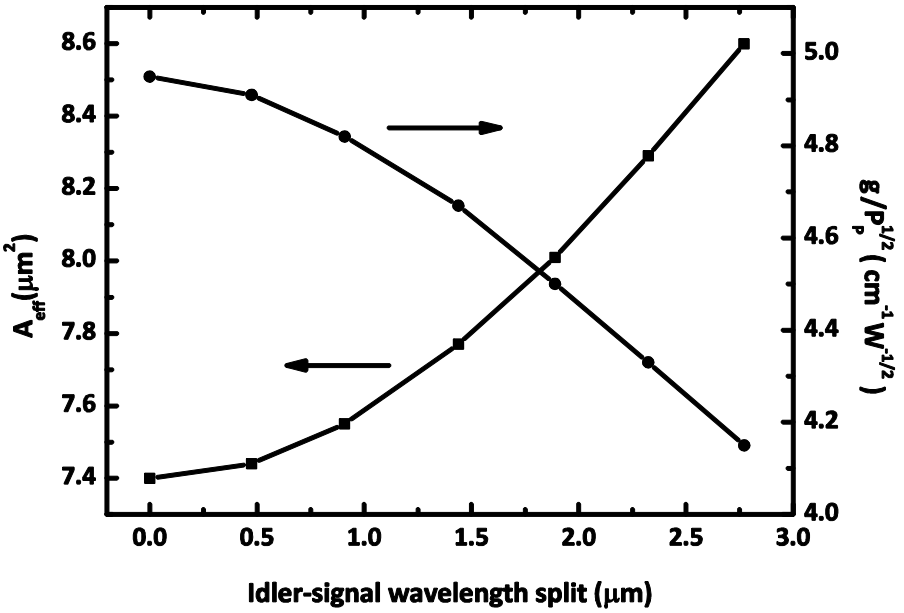

Figure 2.16 Nonlinear effective area A_{eff} and normalized parametric gain $g/\sqrt{P_P}$ vs. idler-signal wavelength separation.

towards the MIR, where its field distribution gets broader, as shown in Figure 2.15. Figure 2.16 reports the effective area and the normalized parametric gain coefficient as a function of idler-to-signal wavelength separation: for a split up to 3 μm, the calculated values slowly change from A_{eff} = 7.4 μm^2 to A_{eff} = 8.6 μm^2 and from $g/\sqrt{P}$ = 4.95 cm^{-1}W$^{-1/2}$ to $g/\sqrt{P}$ = 4.15 cm^{-1} W$^{-1/2}$.

For a further separation, corresponding to an idler wavelength longer than 4 μm, the idler mode is no more well confined, and the nonlinear efficiency falls very quickly, due to poor overlap integral and idler leakage into the substrate. Parametric generation is thus expected to cover the infrared spectrum between 1.2 and 4 μm (assuming no AlOx absorption in this spectral range): it is worth recalling that this wide spectral range is attainable with some tens of nm of pump wavelength tuning. Throughout the tuning range, the parametric gain decreases less than 20% with respect to maximum value. The exploitation of such a device in a resonant cavity would thus allow widely tunable parametric oscillation, provided that the cavity mirrors are highly reflecting over the same spectral width.

2.2 Waveguide fabrication

As detailed in Section 1.2.4, in spite of promisingly high nominal values, the efficiency of GaAs/AlOx nonlinear waveguides has been limited so far by high propagation losses. These arise mainly from scattering at AlOx layers interfaces, due to the oxidation process. In this Section we will briefly describe the origin of this problem and the fabrication improvements we have introduced with respect to the state of the art.

2.2.1 Growth and lithography

Both structures A and B have been grown by MBE in the laboratories of Thales Research and Technology (Palaiseau). MBE is historically the solution of choice for GaAs/AlOx waveguides, due to the its performances in terms of: 1) precision on the layer thicknesses, which is crucial towards the achievement of a given phase-matching wavelength; 2) abruptness of the layer interfaces, a key issue to limit scattering losses following from oxidation of AlAs layers.

As regards processing, different techniques have been reported. As anticipated in Section. 1.2.4, besides a ridge for lateral confinement, GaAs/AlOx waveguides require a mesa for the lateral oxidation of AlAs layers from sidewalls (Figure 1.12). To date, two distinct etching steps were performed to this aim.

1) For the first form-birefringent PM frequency conversion demonstrations [Fiore, 1997a; Bravetti, 1998] both these structures were defined by reactive ion etching, with propagation losses ≈ 5 dB/cm before oxidation and ≈ 7 dB/cm after oxidation.
2) In the following works from the same group [De Rossi, 2001], reactive etching was replaced

with standard H_2SO_4:H_2O_2:H_2O wet etching. This choice, at the price of a poorer control of the shape and the size of the ridge, results in smoother etched surfaces with respect to plasma assisted technique. Losses were reduced to less than 0.3 dB/cm before oxidation and 4 dB/cm after oxidation. With this approach, AlOx layers became the main cause of limited waveguide transmission in the NIR.

Since scattering at AlOx interfaces increases with oxidation duration, as explained in Section 2.2.2, we have chosen to abandon the double-etching process and to adopt a different procedure based on a single narrow ridge for lateral confinement and oxidation. Thanks to the low superficial roughness achieved by chemical etching, the adoption of deeply-etched narrow structures for lateral guidance does not imply a degradation of the waveguide transmission due to scattering at ridge sidewalls. On the other hand, the oxidation time required to completely convert AlAs layers in AlOx is enormously reduced, resulting in a further gain in terms of attenuation coefficient.

Figure 2.17 shows an oxidized ridge obtained following this procedure. Because of etching solution isotropy, the depth and the width of the ridge can't be controlled

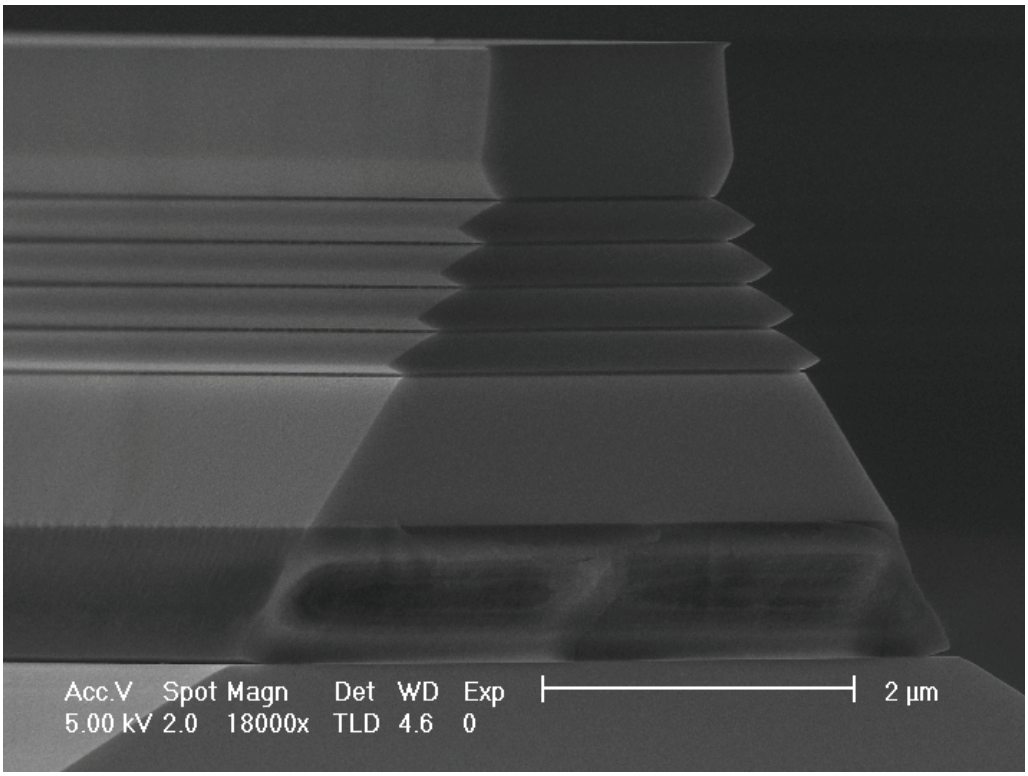

Figure 2.17 SEM (scanning electron microscopy) image of a structure B ridge waveguide etched by H_2SO_4 solution and oxidized: sidewalls motif arises from etching slight selectivity.

independently. In particular, under-etching results in a trapezoidal profile, narrower than the original mask pattern. On the other hand, the saw-tooth sidewall pattern stems from the slight selectivity of the etching solution, the faster the higher is the Al content. Anyway, this peculiar profile affects by no means optical losses.[23] Initially employed H_2SO_4:H_2O_2:H_2O solution has been successively replaced with the more performing HBr:CH_3COOH:$K_2Cr_2O_7$. Besides being less selective, the latter reduces under-etching and, above all, further improves etched surface smoothness (see Figure 2.18). A surface analysis at the atomic force microscope has revealed a roughness reduction from 3 to 2 nm rms. This amelioration represents an advantage also for the oxidation process. Indeed, a smoother AlAs/Air lateral interface is supposed to improve oxidation kinetics, allowing a better flux of H_2O toward the ridge core and a better release of reaction products.

It is worth comparing the above roughness values with those recently reported by Fejer's group for strongly confining AlOx waveguides obtained by e-beam lithography + chlorine plasma etching. [Scaccabarozzi, 2006] Their 6 nm rms measured on the ridge sidewalls suggest that, in spite of recent improvements, plasma-assisted etching does not provide yet the same surface quality as wet etching. The latter, in spite of poor control and reproducibility, remains a reasonable choice when low propagation losses are a priority.

2.2.2 AlAs layers wet oxidation

AlAs, or more precisely, AlGaAs with high Al molar fraction, gets easily oxidized if exposed to air. [Dallesasse, 1990b] The resulting oxide is unstable and causes the material to crumble. This process thus severely affects the performances of AlGaAs devices, such as lasers and more generally waveguides, containing Al rich layers. In the early 90's, an attempt to accelerate this process in a wet atmosphere at high temperature, led to demonstrate the formation of a stable native oxide [Dallesasse, 1990a]. The so obtained aluminum oxide, AlOx, exhibits a refractive index much lower than that of AlGaAs and it is electrically insulating. The possibility of incorporating this oxide inside complex III-V heterostructures quickly opened up new perspectives: oxide apertures for current-confined VCSELs, [Choquette, 1995] efficient high-index contrast GaAs/AlOx distributed Bragg reflectors (DBRs),[MacDougal, 1994] semiconductor

[23] Such a ridge shape just results in modal distributions with an analogous saw-tooth profile. As this profile is translation invariant along the propagation direction, it does not cause any energy transfer towards other guided or radiation modes.

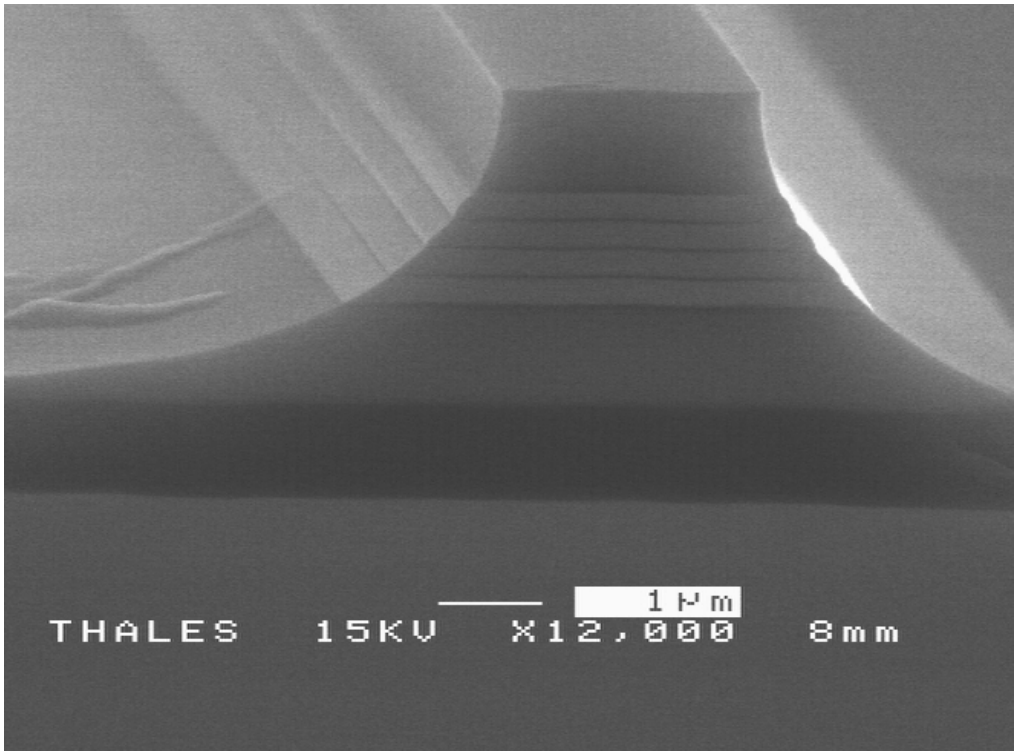

Figure 2.18 SEM image of a ridge waveguide etched by HBr solution and oxidized: besides a reduced selectivity, this processing has produced the best results in terms of sidewalls smoothness.

nonlinear waveguides for frequency conversion, [Fiore, 1997c] and AlGaAs-based MOS junctions. [Chen, 1995]

AlOx is obtained following a procedure similar to silicon wet oxidation, but at a lower temperature (400-500 °C). In these conditions, AlGaAs turns into an aluminum oxide by one of the following reactions [Sugg, 1991; Sugg, 1993]

$$AlAs+2H_2O \longrightarrow AlO(OH)+AsH_3 \quad - \quad AlO(OH)+AlAs+H_2O \longrightarrow Al_2O_3+AsH_3 \tag{2.5}$$

$$2AlAs+3H_2O \longrightarrow Al_2O_3+2AsH_3 \tag{2.6}$$

A buried thin AlGaAs layer can be oxidized (see Figure 1.12), starting from the etched sidewalls of a mesa or from a cleaved facet. In general the oxidation rate can be either linear, if the process is reaction limited, or rather quadratic if diffusion limited [Ashby, 1997]. It strongly depends on several parameters:

- Al composition: the oxidation rate increases with Al composition. [Nickel, 1995] A difference larger than one order of magnitude was found between $Al_{0.86}Ga_{0.14}As$ and AlAs. [Kim, 1996]
- Layer thickness: the oxidation rate increases with the layer thickness as well, until it

saturates at about 100 nm. Oxidation is not possible for layers thinner than 10 nm. [Kim, 1996]

- Temperature: the rate dependence on temperature was suggested to be exponential, $r = C \cdot \exp(-E_a/kT)$, with an activation energy E_a between 1.1 and 1.2 eV for an Al content > 60%. [Nickel, 1995]

Not only is oxidation kinetics very sensitive to the different parameters involved, but also the structure and the characteristics of the final oxide. AlOx is basically composed of polycrystalline γ - Al_2O_3, with grain size up to about 10 nm, and amorphous Al_2O_3. The oxidation conditions favoring the former or the latter structure have not been unambiguously clarified yet, although extensively studied by means of transmission electron microscopy (TEM) observations. [Twesten, 1996; Takamori, 1996] It seems anyway that the presence of amorphous regions originates from the mechanical stress due to the smaller volume (about 50%) of γ-Al_2O_3 with respect to AlAs. [Guha, 1996] The contraction of AlOx layers was quantitatively studied either by TEM observations or by X-ray reflectometry: apart from a dependence on Al composition, values between 6% and 13% have been reported. [MacDougal, 1994; Twesten, 1996; Durand, 2003] The consequent mechanical stress induced in the structure increases with the oxidized layer thickness and can lead to delamination. [Fiore, 1997c] Different pieces of advice concern the maximum layer thickness not affected by this problem: values from some hundreds of nm up to more than 1 μm have been reported. About this subject, there is nevertheless a general agreement on the better mechanical resistance of oxidized AlGaAs layers with respect to oxidized AlAs. [Choquette, 1996]

Also the knowledge of AlOx optical properties is affected by inconsistence between reported measurements. While AlOx transparency region has been unambiguously demonstrated to extend from deep UV (about 240 nm) up to 10 μm, [Fiore, 1997c; Bravetti, 1998; Hall, 1999] excepted an O-H absorption peak at 3 μm, several different values of the AlOx refractive index have been reported. In the NIR these are included between 1.55 and 1.64, with a claimed dependence on the original AlGaAs composition. [Knopp, 1998; Hall, 1999; Durand, 2003]

For many applications, an accurate knowledge of the AlOx physical properties is not mandatory: e.g. for GaAs/AlOx DBRs, the reflectivity bandwidth being extremely broad, a high

level of accuracy on the index contrast or on the AlOx layer thickness is not necessary. Conversely, this is a major issue for the design of birefringent GaAs/AlOx nonlinear waveguides, as uncertainty on these properties affects the phase-matching wavelength of such devices.

An additional point of concern for GaAs/AlOx waveguides is AlOx morphology and its relation with scattering losses. Analyses based on Auger spectroscopy (AS) and TEM have shown that the main source of losses in oxidized structures are a-few-nanometers-thin layers that form at the interfaces between AlOx and GaAs layers. [Fiore, 1997c; Durand, 2003] These layers, that AS identifies as a Ga oxide (GaOx), exhibit a roughness markedly higher compared to the adjacent, homogeneous, AlOx. The formation of GaOx is supposed to be subsequent to AlAs oxidation and to continue during prolonged heating, which explains why scattering in oxidized multilayers increases with oxidation duration. This interpretation, which has recently been confirmed by spectroscopic losses measurements, [Rao, 2002] induced us to abandon the double-etching processing, where 100 μm wide mesa requires an oxidation time longer than 1 hour.

Our oxidation process is carried out in a quartz tube oven where samples are heated at 420-430°C while the atmosphere is saturated in water vapor by a 2 l/min flux of wet N_2. This is

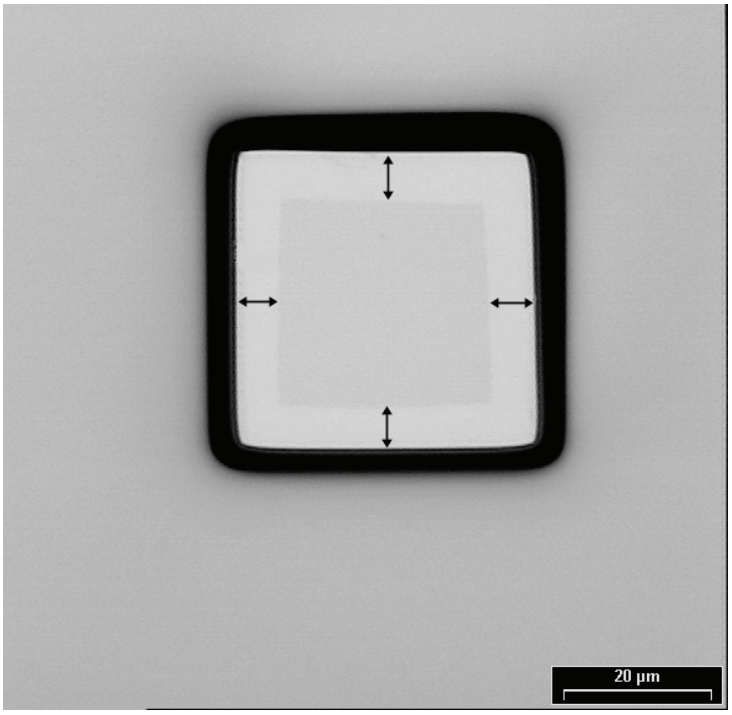

Figure 2.19 Partially oxidized squared mesa observed at microscope: the arrows point out the progress of the oxidation front on the four sides.

obtained by previously making dry N_2 pass through a water bubbler stabilized at 70 °C. Under these conditions we achieve a repeatable linear oxidation rate of about 0.3 μm/min. [Fiore, 1997c] In addition, in our vertical structure the oxidation progress can be directly measured by optical microscope observations: in fact, oxidation of $Al_{0.98}Ga_{0.02}$ layers induces an evident increase of the reflectivity of the structure upper surface. This variation, while clearly recognizable on unprocessed planar samples (where oxidation can progress from a cleaved edge), is hardly perceptible on some μm large ridges, because of their limited width. That is why, with the aim of systematically verifying the oxidation progress on every sample, 50 μm wide, squared mesa are defined along with ridges, and observed after oxidation. Figure 2.19 shows a microscope picture of an oxidized mesa: the oxidation front, on the four sides, can be easily recognized. Thanks to this expedient, we can set an oxidation time just sufficient to entirely cover ridge width. This solution along with the novel processing technique has allowed us to further improve the transmission characteristics of GaAs/AlOx waveguides with respect to the best results previously reported. [De Rossi, 2001] This has been demonstrated by systematic loss measurements.

2.3 Optical loss measurement

Compared to gradual index dielectric waveguides, high-index-contrast semiconductor waveguides are significantly affected by scattering losses. Scattering can originate from roughness on either the ridge sidewalls or the epitaxial layers interfaces, as well as from bulk media inhomogeneity.

Attenuation measurement is a key issue for the development of semiconductor and, in general, of all guided-wave devices. Among the different techniques proposed to this purpose, the simple transmission evaluation is certainly the easiest approach. Nevertheless, the precision attained in this way is considerably limited by the uncertainty on the input coupling efficiency. Hence, this method is often performed by progressively reducing the sample length (cut-back method). [Kaminow, 1978]

Another possibility is represented by scattered light measurement: [Okamura, 1983] in this case the waveguide superficial scattering is measured along the propagation direction by means of a local probe or of near-field imaging, allowing to infer the modal attenuation. While the latter method has the advantage, compared to the former, of being non-destructive, it is

not suitable for losses lower than a few tenths of cm^{-1}, and its accuracy considerably depends on the quality of the device surface.

Scattered light measurements in AlOx waveguides, with a femtosecond NIR OPO, have allowed to determine the dependence of propagation loss on both wavelength and intensity. [Rao, 2003] In the range from 1.3 to 2.1 μm, losses were found to decrease with wavelength, as expected for Rayleigh scattering. This confirms the dominant contribution of AlOx/GaAs interface roughness to the attenuation coefficient, as already emerged from TEM observations. The high peak intensities employed (≈ 1 GW/cm^2) in such experiments have allowed to measure as well the two-photon-absorption (TPA) coefficient of these waveguides, $\beta \approx 10$ cm/GW around 1.55 μm.[24]

In order to draw some feedback for our processing optimization, we adopt another non-destructive technique, based on a simpler experimental setup and with a higher sensitivity. This resorts to Fabry-Perot transmission fringes in the waveguide to infer the attenuation coefficient independently on input coupling efficiency.

2.3.1 The Fabry-Perot technique

This technique, at first employed on $LiNbO_3$, [Regener, 1985] allows loss evaluation of single-mode waveguides. The knowledge of modal facet reflectivity is required, the precision of this value limiting the measurement accuracy.

Due to the modal reflectivity at input and output facets, the transmission of a waveguide can be treated analogously to that of a Fabry-Perot resonator in plane-wave approximation. In a single-mode waveguide, for a monochromatic input, the transmission is given by the Airy function

$$T_{FP} = \frac{T^2 e^{-\alpha L}}{(1-R')^2 + 4R'\sin^2(\phi/2)}\eta \qquad (2.7)$$

where α is the modal attenuation coefficient, L the waveguide length, η the coupling efficiency, T (R) the transmission (reflectivity) of the two facets (supposed equal), and $R' = R\cdot\exp(-\alpha L)$.

[24] With 1 GW/cm^2, such TPA coefficient results in an attenuation of 1 cm^{-1}. In our nonlinear experiments, carried out with CW sources, guided-wave intensity is always lower than 1MW/cm^2 and TPA contribution is negligible with respect to scattering.

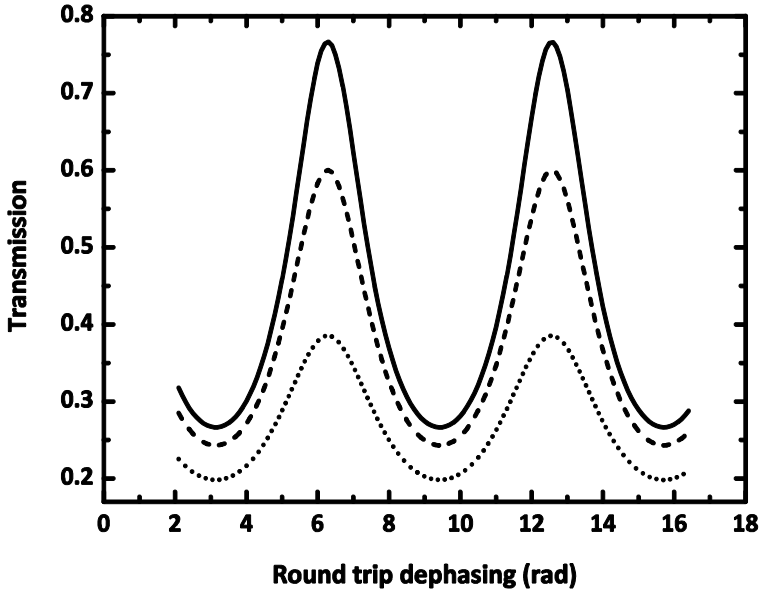

Figure 2.20 Calculated waveguide transmission fringes for R = 30%, η = 1; and αL = 0.15 (solid line), 0.3 (dashed line), and 0.6 (dotted line).

T_{FP}, as shown in Figure 2.20, is a periodic function of the round-trip dephasing $\phi = 2k_0 n_{eff} L + \phi_0$, with k_0 the free-space wave vector and n_{eff} the effective index. By tuning the input wavelength or the effective index (by e.g. varying the sample temperature), T_{FP} oscillates between a maximum T_{max} and a minimum T_{min} that depend only on R'. By measuring the contrast of the transmission fringes

$$K = (T_{max}-T_{min})/ (T_{max}+T_{min}) \tag{2.8}$$

R' can be inferred exploiting the relation

$$R' = \frac{1}{K}\left(1-\sqrt{1-K^2}\right) \tag{2.9}$$

If the facet modal reflectivity R is known, the attenuation coefficient can finally be calculated as

$$\alpha = \ln(R/R')/L \tag{2.10}$$

In single-mode weakly confining waveguides,[25] R is well approximated by the Fresnel formula

$$R = \left(\frac{n_{eff}-1}{n_{eff}+1}\right)^2 \tag{2.11}$$

[25] As for example Ti:$LiNbO_3$ or annealed H^+:$LiNbO_3$ waveguides.

due to the small numerical aperture of the guided mode. Accordingly, a good accuracy (better than 0.1 dB/cm) on the attenuation coefficient is typically obtained.

The application of the Fabry-Perot loss measurement to semiconductor waveguides is quite delicate. [De Rossi, 2005a] Indeed, guiding core dimension of 1 μm or less and abrupt step-index profiles generally prevent single-mode operation in such devices. With an appropriate design this can be achieved only in the epitaxial growth direction. Conversely, in the other direction, air-semiconductor index contrast results in several horizontal modes, unless a very narrow (≈1 μm) ridge is adopted, at the price of considerably increased propagation losses. Moreover, the large numerical aperture makes the Fresnel formula inadequate to model the facet reflectivity. To this aim, Herzinger has proposed an approach based on matching the electric and magnetic fields at the facet, using the eigenmode expansion in air and in the waveguide. [Herzinger, 1993] However, especially for narrow ridges, three-dimensional (3D) finite-difference time domain (FDTD) simulations are the most suitable tool to calculate this parameter. The resort to such complex calculations is justified by the error on the attenuation coefficient stemming from an inexact estimation of R. The latter heavily affects the precision on the attenuation coefficient, especially for low attenuation values, as stressed by the differential of Eq. 2.10

$$\frac{\Delta\alpha}{\alpha} = \frac{1}{\alpha L}\frac{\Delta R}{R} \tag{2.12}$$

In the multimode case, the waveguide total transmission is given by the superposition of several Airy functions, one for each excited mode. In general, these exhibit different amplitudes and different periodicities (as different are the effective indices). By optimizing the coupling on the fundamental mode, the corresponding Airy function emerges over the others. This is usually possible due to the better overlap of the fundamental mode with a Gaussian beam profile. In spite of that, the fringe contrast is reduced, because of residual power coupled into higher-order modes. In general this results in a considerable error in the attenuation coefficient. Nevertheless, precision can be greatly improved under some conditions:

- The different Airy functions overlapped must have the same contrast: in this case, if they are all in phase, the total contrast corresponds to that of a single Airy function. This is the same as saying that the guided modes must have the same reflectivity and the same attenuation

coefficient. The former condition is reasonably fulfilled if the waveguide is multimode only in the horizontal direction, where the numerical aperture is much smaller than in the vertical direction; the latter, if roughness on the ridge sidewalls is negligible and scattering does not depend on the breadth of the modal distribution.

- The waveguide must admit only few modes in the horizontal direction: in this case, by measuring the transmission over a sufficiently large spectral interval, the Airy functions can be found all in phase at a certain wavelength. Typically, in some μm wide semiconductor ridge waveguides, the difference between the refractive indices of the horizontal modes is so small that, if only two modes are admitted, the beating period is of some tens of nm. In such a case, a tunable laser diode can be employed to find the maximum contrast.

In practice, these conditions can seldom be perfectly satisfied. Standard ridge semiconductor waveguides usually admit more than two modes in the horizontal direction. In addition, their reflectivity and attenuation are in general not identical. However, if most of the input power is coupled into the fundamental mode, the more these conditions are approximated, the better is the accuracy attained.

2.3.2 Experimental results

Our experimental setup to measure the waveguide transmission fringes is based on an external-cavity semiconductor laser (Tunics MC 100), tunable without mode hops between 1500 nm and 1600 nm. Its emission linewidth, narrower than 1 MHz (less than 0.01 pm), is basically monochromatic with respect to the period of the transmission fringes (> 0.1 nm). The 2 mW TE polarized laser beam is collimated and then coupled into the waveguide by means of a 60X microscope objective, with the waveguide output collimated with an identical 60X objective. Coupling into the fundamental mode is achieved and optimized by monitoring the output with an IR Vidicon camera and a power meter, while the waveguide is carefully positioned with respect to the objectives by means of nanometric piezo-actuators.

Measurements have been performed on both A and B samples, in 3 μm wide ridges, with similar results. In such waveguides, admitting TE_{ij} modes with i=0,1 and j=0,1,..,5 at 1.55 μm, the Fabry-Perot technique should not provide reliable results. However, due to the symmetry of both the guiding structure and the input beam, input coupling can be limited to even-parity modes, i.e. TE_{0j} with j=0,2,4, as has been verified with the IR camera. In addition,

the propagation losses of the different horizontal modes excited can be considered reasonably equal. This is because, in our case, the contribution of the sidewall roughness (2 nm rms) to propagation loss is negligible compared to that of AlOx interfaces. Under these two assumptions, all the requirements for an accurate loss measurement are reasonably satisfied. On the contrary, this is not true for unoxidized samples, where three TE vertical modes are guided at 1.55 μm.

Figure 2.21 shows the transmission fringes of an oxidized B sample waveguide, acquired in four different spectral regions of the laser tuning interval: a different contrast between them can be readily appreciated. The maximum contrast value K = 0.501, measured around 1545 nm, corresponds to R' = 0.268.

To achieve the best accuracy on the corresponding attenuation coefficient, the facet reflectivity is calculated by means of 3D FDTD simulations. [Taflove, 2000] These are based on the integration of Maxwell equations on a non-uniform mesh, as required by a guiding structure alternating layers with very different thicknesses (AlOx = 37.5 nm, claddings = 1000

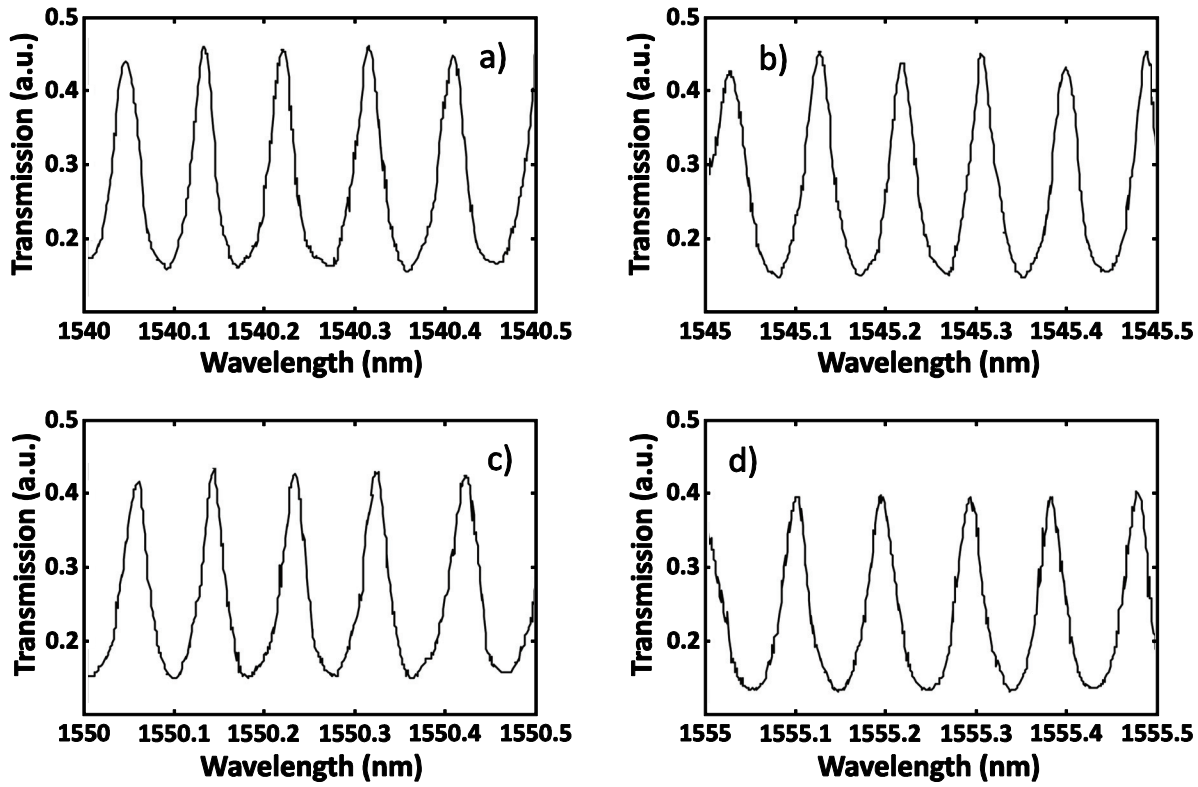

Figure 2.21 Experimental waveguide transmission fringes at different wavelengths: the contrast is K = 0.472 (a), K = 0.501 (b), K = 0.458 (c), K = 0.495(d). Its variation stems from the interference between the fundamental and the higher-order modes.

nm). At first, we calculate the fundamental mode profile by means of 2D FDFD[26] modeling. Then, we make propagate an ultrashort (few-optical-cycle) pulse with the same spatial distribution towards the waveguide facets. Finally, we calculate the projection of total back-reflected field on the fundamental mode. [Gwarek, 2003] Note that, as the spectrum of the excitation is very broad, the reflectivity is readily obtained on a wide wavelength interval around that of interest.[27]

Modeling results for structure B are shown in Fig 2.22 for four different ridge widths at 1.55 μm. The facet reflectivity for the TE_{00} mode is smaller for a narrower ridge. This can be explained by considering the wave vector distribution of the mode in the waveguide plane. For a very wide ridge such distribution is concentrated at normal incidence to the facet. As the ridge width decreases the wave vector spectrum spreads on larger angle interval, and its value for incidence angles around Brewster angle increases, resulting in a lower modal reflectivity. [Ikegami, 1972]

Figure 2.23 shows the attenuation coefficient inferred from the R/R' ratio, for the four transmission spectra of Figure 2.21. Here the effects of the interference between different modes are stressed. The superposition of several Airy functions can lead to overestimate the attenuation coefficient, especially in case of low attenuation, as suggested by the differential of Eq. 2.10

$$\frac{\Delta(\alpha L)}{\alpha L} = -\frac{1}{\alpha L}\frac{\Delta R'}{R'} \tag{2.13}$$

The lowest value measured in this case, α = 0.5 cm^{-1}, is representative of the performances we have achieved with our devices. Thanks to the processing optimization described in Section 2.2, propagation losses between 0.4 cm^{-1} and 0.7 cm^{-1} have been systematically measured on several different samples. Note that the measured attenuation coefficient could be overestimated, as the high number of lateral modes probably prevents the exact in-phase measurement of the different Airy functions, and the contrast of these reasonably depends on the modal order. The above values and in general those obtained with the multimode Fabry-Perot technique can be considered rather as an upper bound to the actual value.

[26] Finite-difference frequency domain.
[27] By neglecting the dependence on wavelength of the modal profile.

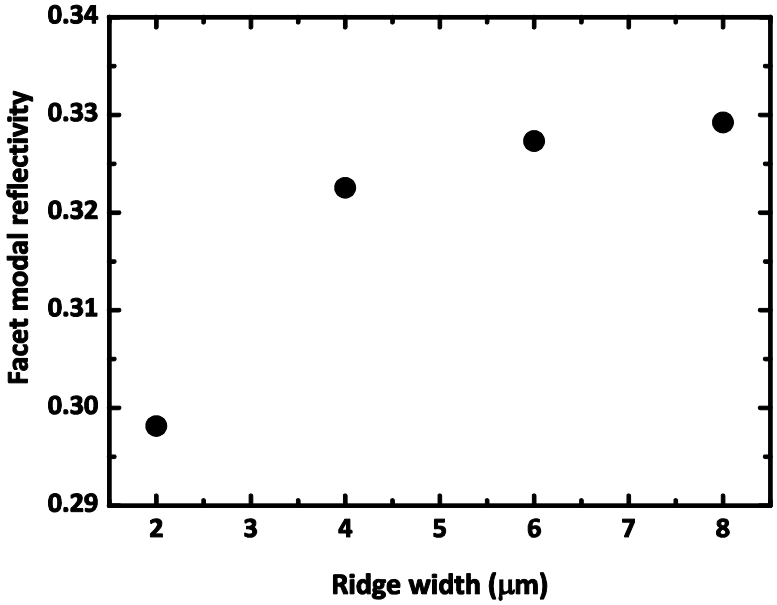

Figure 2.22 TE_{00} facet modal reflectivity at 1.55 μm, as calculated by 3D FDTD modeling.

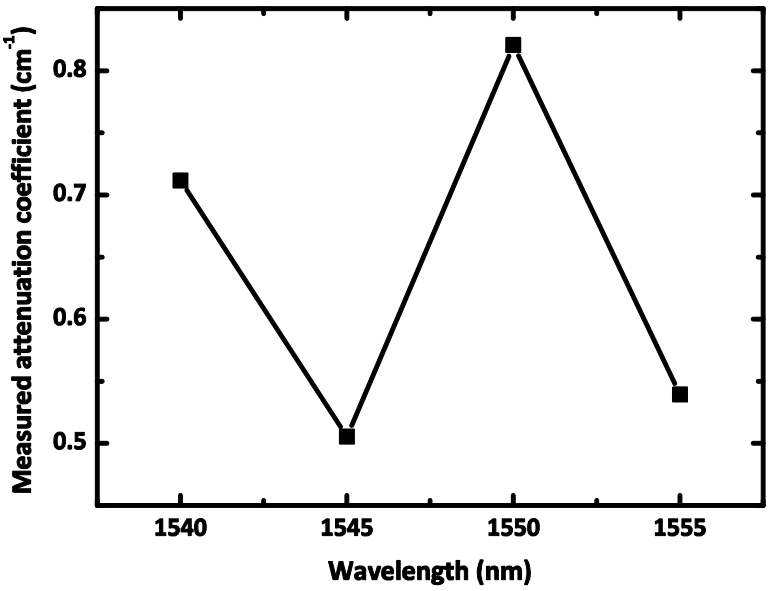

Figure 2.23 Attenuation coefficients corresponding to the transmission spectra of Figure 2.21. We stress how the measurement of the fringes contrast on a wide wavelength interval allows one to find a constructive interference between the excited modes, as in this case at 1545 nm.

2.4 Chapter conclusion

In this Chapter we have detailed the design and fabrication procedures that have led to AlGaAs form-birefringent PM waveguides for parametric generation at 2 μm.

Waveguide design has been addressed primarily to make birefringence compensate the dispersion between the interacting frequencies, through the insertion of thin AlOx layers in the

GaAs core. Overlap integral maximization and scattering losses reduction are further criteria that have led to the final design.

Multilayer structures have been grown by MBE. The processing strategy has aimed at improving the ridge surface quality (a roughness of 2 nm rms has been achieved), and at minimizing the oxidation time (reduced to a few minutes). The latter has been identified as the key issue to reduce the scattering from AlOx/GaAs interfaces. This has induced us: firstly, to introduce a novel processing scheme, based on a single ridge for both oxidation and guidance; secondly, to carefully calibrate oxidation rates on every sample, in order to set an oxidation time just sufficient to entirely cover the ridge width.

With respect to processing optimization, the systematic evaluation of the waveguide losses (Fabry-Perot transmission method) provides a useful feedback. Propagation losses, at present the weak point of this technology, are reproducibly achieved on several samples at a level of 2 dB/cm. This is, to our knowledge, the lowest ever reported for any phase-matched AlGaAs nonlinear waveguides.

3 Waveguide nonlinear characterization: conversion efficiency and tuning

In a second-order nonlinear interaction, the phase-matching condition defines the set of frequencies (ω_1, ω_2, and $\omega_3=\omega_1+\omega_2$) of the three fields that can be efficiently coupled by the $\chi^{(2)}$ tensor. [28] Under this condition, the direction of the energy transfer between the three fields is determined only by their initial phases. In other words, it is equally possible to inject in the crystal the fields at ω_1 and ω_2 and generate the field at ω_3 by a SFG process or alternatively to inject the fields at ω_1 and ω_3 and generate the field at ω_2 by a DFG process: the photon efficiencies of up- and down-conversion are equal. This allows one to exploit the most convenient interaction, as regards e.g. the available sources, to experimentally characterize the nonlinear device.

Such a possibility is particularly useful in the case of integrated frequency converters. Indeed, the characterization of these devices concerns not only the nonlinear coefficient of the material, but also the waveguide structure. The conversion efficiency is connected to the nonlinear overlap integral, and the tunability to the effective indices of the interacting modes, rather than the refractive indices of the medium. Moreover, as the fields propagation and their transverse distributions are fixed by guidance, the characteristics of up- and down-conversion are related in a straightforward way.

In this Chapter we present our extensive nonlinear characterization of the guiding structure introduced in Chapter 2, comparing the results obtained in different configurations. In Section 3.1, we present the experimental performances of parametric fluorescence in terms of conversion efficiency and tunability. In Section 3.2, we describe a frequency doubling experiment, the inverse process of PF at degeneracy, performed to infer the parametric gain coefficient of the device. Finally, in Section 3.3, we provide a further and more accurate measurement of this crucial parameter, obtained through an experiment of seeded down-conversion.

3.1 Parametric fluorescence experiments

After its first demonstration in bulk crystals, which traces back to the birth of nonlinear optics in

[28] See Section 1.1.2.

the early 1960's, [Harris, 1967] PF was obtained in guided-wave geometry in the 1980's, in $LiNbO_3$. [Hampel, 1986] In semiconductor waveguides it has been accomplished in the last decade, and only three demonstrations have been reported to date, all in GaAs, based on:

1) form birefringent phase matching; [De Rossi, 2001]

2) quasi phase matching; [Tachibana, 2003]

3) counterpropating phase matching. [Lanco, 2006a]

Hence, in order to have a term of comparison for our device, we find it more appropriate to refer to a highly efficient QPM H^+:$LiNbO_3$ waveguide. [Chanvillard, 2000] This 2 cm long device, pumped by a CW Ti:Sapphire laser, delivers temperature-tuned signal and idler beams between 1.48 and 2.01 μm. 1 nW of signal power was achieved with 1.95 mW of injected pump power, corresponding to a conversion efficiency $\eta_{PF} = P_S / P_P = 5\times10^{-7}$.

3.1.1 Experimental setup

The experimental setup for PF experiments is shown in Figure 3.1. The pump source is a Spectra-Physics 3900S CW Ti:Sapphire laser (tunable between 685 nm and 1130 nm) pumped by a Spectra Physics Millennia 15 W. The linewidth of the source is 40 GHz.[29]

Several elements are aligned along the optical axis:

- a long-focal lens, to shape the beam spot for matching the TM_{00} mode profile after the input objective;
- a Faraday isolator, to avoid back-reflections onto the pump source, in particular from the waveguide input facet;
- the combination of a half-wave plate and a polarizer, to attenuate the pump power, plus a second motorized half-wave plate, to finally select the waveguide input polarization;
- a beam splitter, extracting 50 % of the input beam to monitor in real time: its power, with a power meter plus Ge photodiode; its intensity profile, by means of a CCD camera; its linewidth and wavelength, with a spectrum analyzer and a spectrometer, respectively;
- the coupling stage: waveguide input and output couplings are obtained with two 60X microscope objectives, mounted on three-axis nanopositioners and aligned on the optical

[29] The 3900S can be equipped with a pair of etalons that limit the operation to 2 or 3 longitudinal modes, with a corresponding linewidth ≈ 1.5 GHz. However, in this configuration, the laser is not continuously tunable. As for PF experiments such a narrow linewidth is not necessary, due to the large acceptance band of this process, [De Rossi, 2001] we have worked without the etalons.

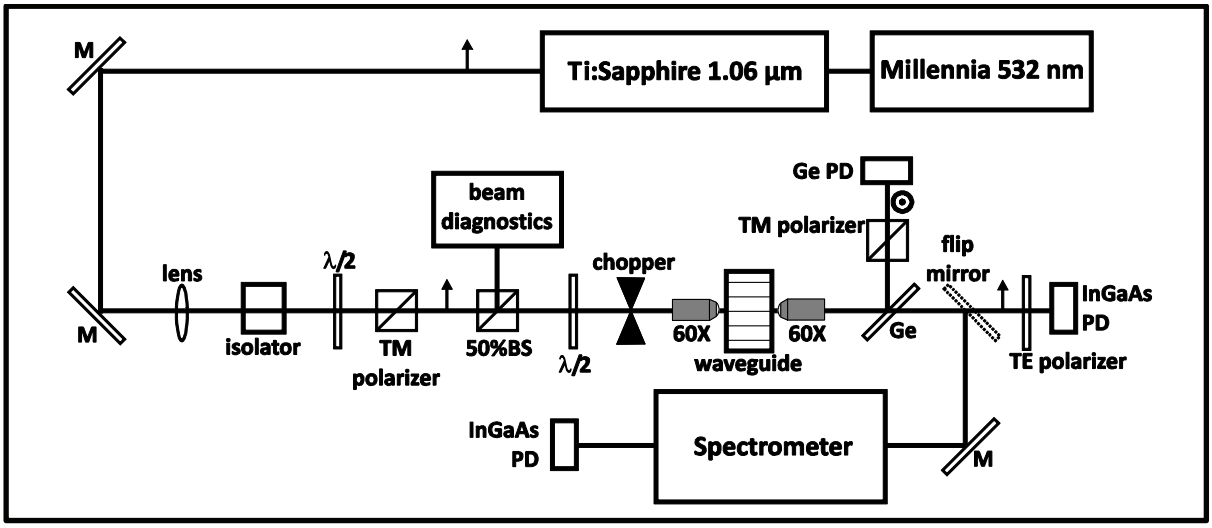

Figure 3.1 PF experimental setup.

axis. A third, four-axis, translator is responsible for tilting and translating the waveguide between the objectives. The sample is fixed on an Invar mount (preferred to copper because of its better thermo-mechanical properties) equipped with a Peltier cell and a thermistor to set and stabilize the waveguide temperature;

- a Ge filter acting like a dichroic mirror, which reflects a part of the pump field on a Ge photodiode. The transmitted PF field is focused on an InGaAs strained photodiode with a cut-off wavelength of 2400nm, which is connected to a lock-in amplifier. The polarization of both pump and PF outputs is checked by means of polarizers placed in front of the two detectors. In addition, the generated field at 2 µm is focused into a high-resolution spectrometer, to acquire PF spectra.

All the experimental setup is sheltered by a laminar flux hood producing a class 10000 clean environment, to protect the laser sources and the sample from dust.

3.1.2 Conversion efficiency measurements

PF experiments are usually performed with a pump power up to 200 mW, measured before the input objective. Typical throughputs, measured after the ouput objective, are 20%-30%, mainly depending on Fabry-Perot transmission fringes.[30] In addition, the throughput is limited by

[30] As discussed in Section 2.3.1, coupling efficiency vs. wavelength of our waveguides strongly oscillates due to the high reflectivity of the facets. The linewidth of the Ti:Sapphire laser, although much larger than that of the telecom laser employed for loss measurements, is still comparable with the FSR of our waveguides. For this reason, in the following we always refer to internal power values, which are inferred from what measured after the output objective.

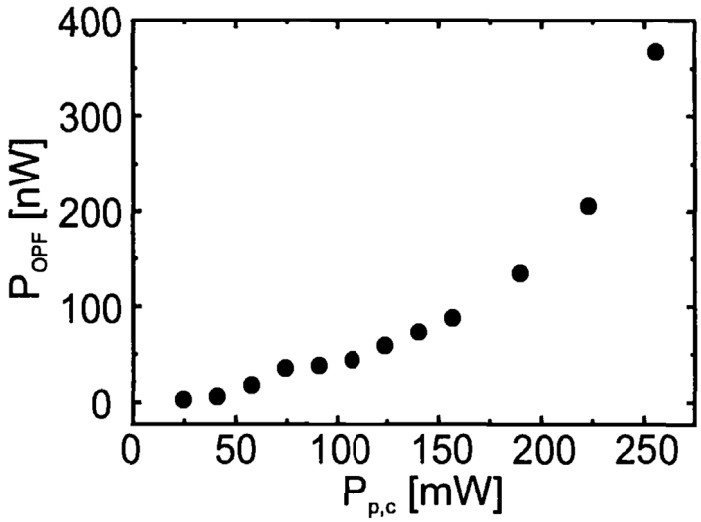

Figure 3.2 Degenerate PF at 1.55 μm vs pump power in highly efficient $LiNbO_3$ waveguides. Thanks to an interaction length L = 5 cm and a coupled pump power up to 250 mW, parametric generation goes beyond the low-gain regime and exhibits a nonlinear dependence on the pump intensity. The normalized parametric gain of the waveguide is $g/\sqrt{P_P} \approx 0.4\ cm^{-1}W^{-1/2}$ (from Ref. [Schreiber, 2001]).

objective transmission, propagation losses and mismatch between the pump beam spot and the TM_{00} mode profile. Maximum input power is dictated by the irreversible damage of the input facet: a power higher than 200 mW generally results in a reduced waveguide transmission, the lower the higher is the intensity of the pump. More rarely the transmission falls suddenly to zero due to dust particles burned on the facet by an intense pump field. Although sometimes it is possible to focus up to 1 W on the input facet, with $P_P \approx 200$ mW coupled into the TM_{00} mode, 200 mW has been conservatively established as the maximum input power. In these conditions, at degeneracy, the power of the generated signal is $P_S \approx 100$ nW.

Such limitation on P_P prevents to obtain a significant generation efficiency in a non-resonant, single-pass configuration: with an input pump beam power of 200 mW, we estimate a power coupled on the TM_{00} mode $P_P \approx 80$mW, corresponding to $gL \approx 0.4$. Our motivation to maximize P_P is to go beyond the low-gain regime ($gL \ll 1$), so as to observe and study a nonlinear relation between signal and pump power, as in the example shown in Figure 3.2. These measurements of conversion efficiency are always performed at degeneracy, where parametric gain is maximum and type I phase matching exhibits a huge spectral broadening (see Figure 2.10), with a resulting larger quantum noise effective input.

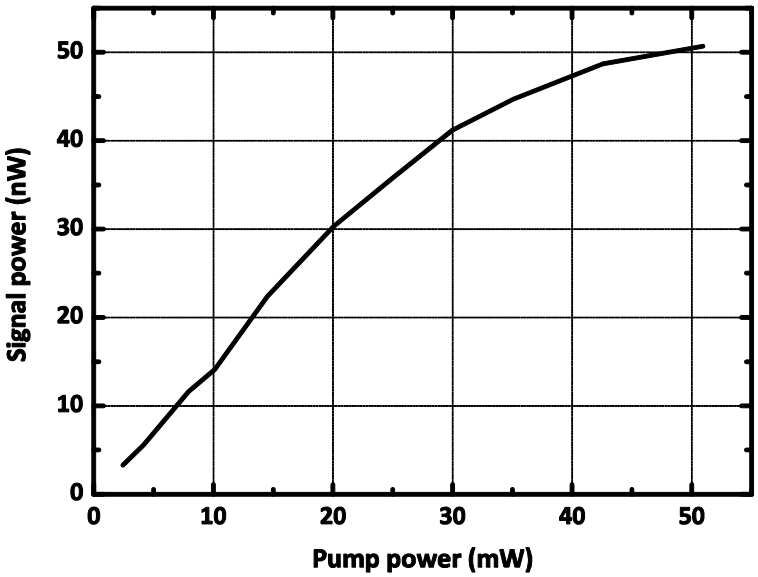

Figure 3.3 Generated signal versus pump power (preliminary measurement): increasing pump intensity warms the waveguide, shifting degeneracy wavelength toward higher values (see Fig. 3.9): consequently, the conversion efficiency is reduced as the pump power is raised.

All the experimental results presented in this Section have been obtained in a waveguide B with ridge width w = 3 μm and length L = 3 mm.[31] Structure A has been grown later than structure B and has been employed in particular for the experiments of seeded down-conversion (Section 3.3).

Our first P_S vs. P_P measurements have resulted in curves as the one shown in Figure 3.3, with an unexpected sub-linear dependence. Such a behavior arises from waveguide heating induced by the intense pump, which we estimate at a few degrees for P_P = 80 mW and we ascribe to absorption due to below-band-gap energy levels. Waveguide heating results in an off-degeneracy-shift of the phase-matching condition, as shown in Figure 3.9. Accordingly, the PM spectrum gets narrower and the spectrally integrated PF power lower, thus preventing a correct measurement of the P_S vs. P_P characteristic. The solution we have adopted to overcome this problem is to keep constant the pump power and progressively rotate its polarization, based on the fact that only its TM component is useful for the nonlinear generation. By means of the motorized half-wave plate, the input polarization is gradually turned from TE to TM, while the PF and the TM pump component are measured at the waveguide output.

Figure 3.4 shows both P_S and the TM pump component P_P vs. the half-wave plate angle.

[31] On this waveguide we have measured an attenuation coefficient α = 0.5 cm^{-1} at 1.55 μm.

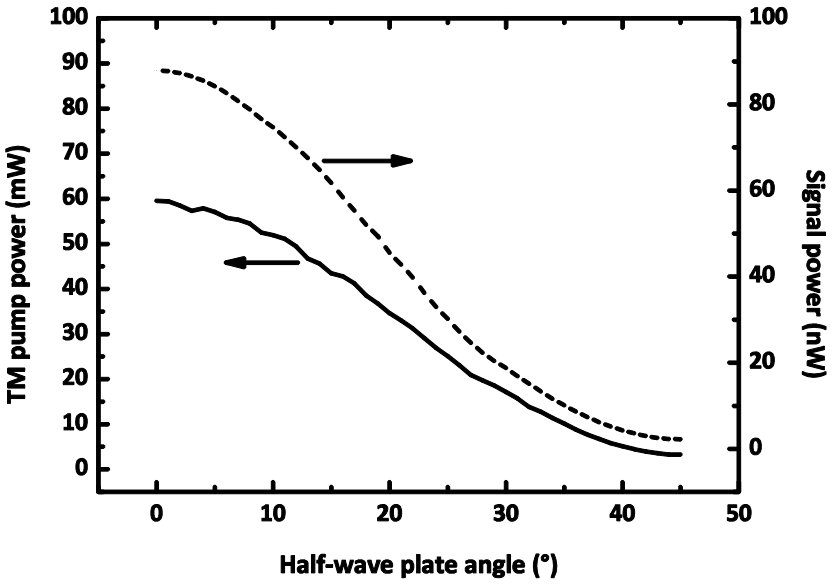

Figure 3.4 TM pump and TE signal power versus half-wave plate angle.

We stress that the angular position of the output-pump analyzer is critical: a misalignment with respect to the actual TM polarization would produce an angular shift of one curve respect to the other, introducing an artificial nonlinearity in the relation between the P_P and P_S. In Figure 3.5, P_S and P_P are plotted one versus the other: a slight superlinear evolution is appreciable, as stressed by the tangent at the origin. Through a linear fit[32] we infer an internal conversion efficiency $\eta_{PF} = (1.5 \pm 0.2)\times10^{-6}$, after careful setup calibration[33]: objective transmission, measured at λ_P and $\lambda_{S,I}$, as well as facet reflectivity (24% at λ_P and 29% at $\lambda_{S,I}$, by 3D FDTD numerical modeling) are taken into account.

With respect to our benchmark performances in $LiNbO_3$ waveguides, [Chanvillard, 2000] we have thus obtained a higher η_{PF} with an interaction length 7 times shorter. Moreover, thanks to a considerably higher pump power injected, we have achieved a two-order-of-magnitude higher signal power. The reproducibility of these results in several experiments, performed with different waveguides, confirms the reliability of this novel measurement procedure.

[32] As the relation between P_P and P_S is nonlinear, the conversion efficiency varies with P_P. More precisely it increases from 1.3×10^{-6} at low power, to 1.7×10^{-6} at high power. The best fit of all the data points with a straight line returns the average value.

[33] The uncertainty reported arises mainly from that of detector calibration. More precisely, a 2.5% uncertainty on the power measured with both the InGaAs photodiode at 2 μm and the Ge photodiode at 1 μm. In addition, we have considered a 0.5% uncertainty on the transmission calibration of all the optics involved. The same considerations are valuable for all the experiments described in this chapter.

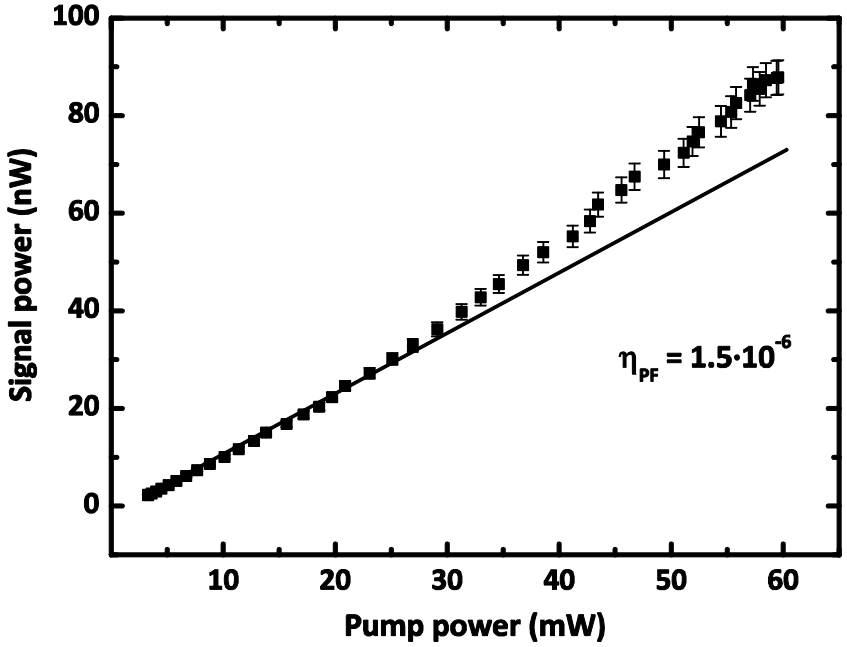

Figure 3.5 Generated signal versus pump power: the nonlinear trend of experimental data (squares) is pointed out by the linear fit of the low power points (solid line).

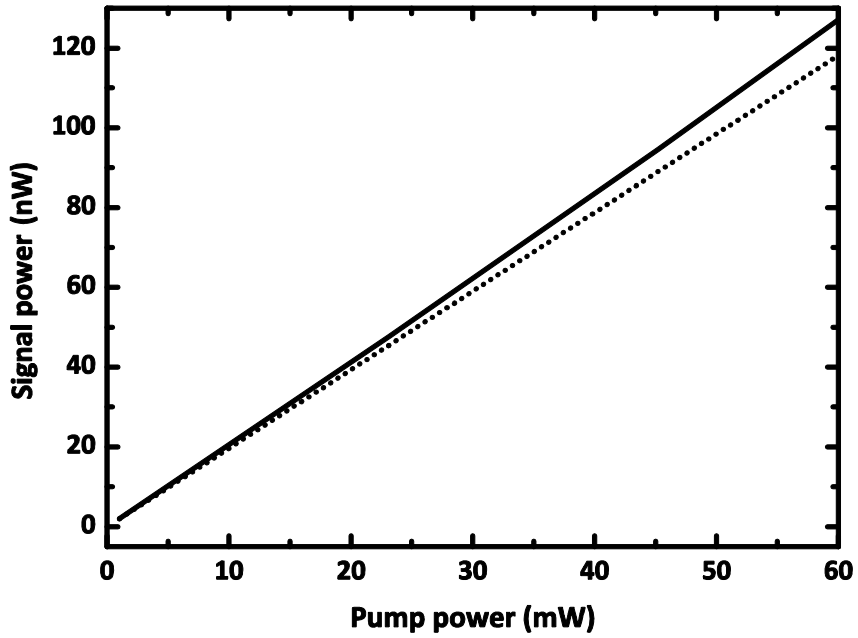

Figure 3.6 Signal versus pump power calculated on the basis of experimental SHG conversion efficiency (solid line) and linear fit at low power (dotted line).

To compare the experimental P_S vs. P_P curve with its theoretical counterpart, we have performed a simulation based on the PF model described in Section 1.1.3. According to Eqs. 1.19, 1.24 and 1.25, we have calculated the quantum-noise effective input and the nominal parametric gain coefficient. The so-obtained P_S vs. P_P curve, shown in Figure 3.6 exhibits a

superlinear dependence of P_S on P_P, consistently with what observed experimentally.

The calculated conversion efficiency, $\eta_{PF} = P_S / P_P = 2.26\times10^{-6}$, is slightly higher (50%) than the experimental value. Such discrepancy can arise from a lower value of either the experimental parametric gain or the quantum noise effective input with respect to their calculated counterparts. An experiment of PF does not allow to single out these contributions, and thus to infer a reliable value of the parametric gain coefficient. This can be precisely investigated by performing an SHG or a DFG process, as reported in Sections 3.2 and 3.3.

3.1.3 Parametric fluorescence spectra

PF spectra are acquired with a Jobin Yvon Triax 550 high resolution spectrometer plus an InGaAs strained photodiode. The wavelength detection range has an upper limit at 2400 nm due to the detector cutoff, and a lower limit at 1300 nm due to the high-pass interferential filter employed to block the pump.[34] Nevertheless, this setup allows one to study the whole tuning range, as idler wavelengths longer than 2400 nm can be inferred from measured signal and pump wavelengths, through frequency conservation.

Two PF spectra from a structure B sample, at degeneracy and 0.2 nm off degeneracy, are reported in Figure 3.7. Besides the good signal-to-noise ratio, their sinc^2 shape demonstrates the high uniformity of the waveguide over a few millimeter length. Note that, due to the broad PM band, spectrum acquisition near degeneracy is affected by chromatic dispersion of the output microscope objective, which makes the waveguide out-coupling critical. Of course, this is not an issue far from degeneracy, where PM bandwidth decreases to tens of nanometers.

By acquiring PF spectra for different values of λ_P we have reconstructed the tuning curve shown in Figure 3.8 (crosses). A tuning range between 1.69 μm and 2.75 μm has been obtained, limited by the losses experienced by the idler mode beyond 2.75 μm.[35] Such interval has been covered by varying λ_P over a 12 nm interval, with degeneracy at λ_P = 1060.5 nm, slightly shorter than the nominal value (λ_P = 1064 nm). These data can be reasonably fitted by a curve (solid line) obtained from effective-index calculations, with the thickness t of GaAs layers

[34] In order to extend the wavelength detection range, here such interferential filter is preferred to the Ge filter used in other PF experiments.

[35] See Section 5.1.1.

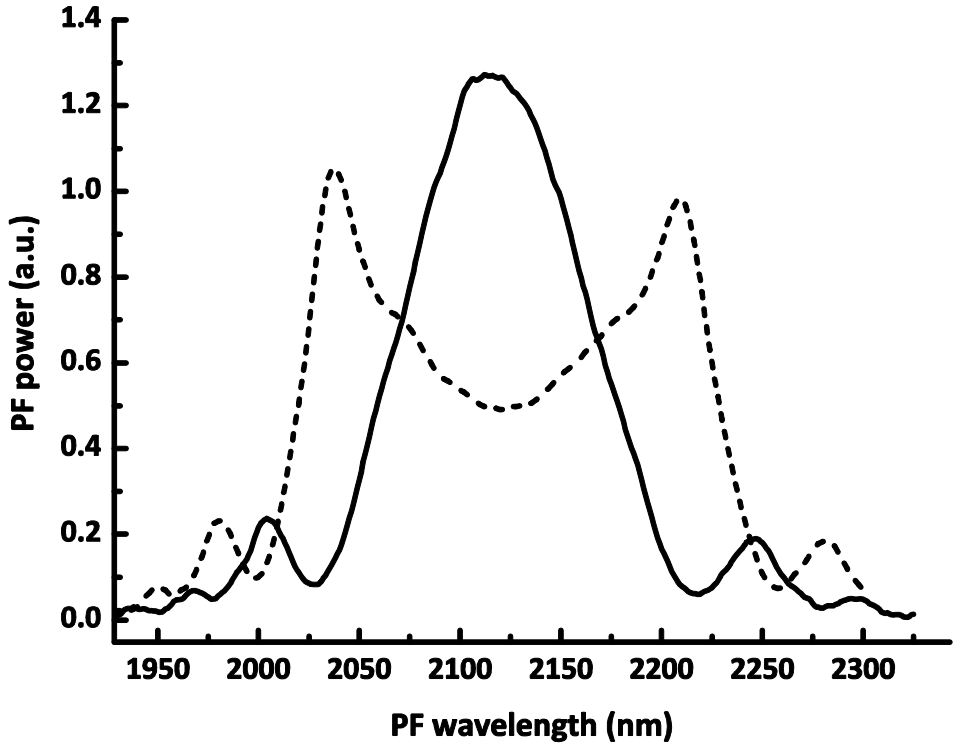

Figure 3.7 PF experimental spectra: at degeneracy (solid line) and 0.2 nm off degeneracy (dashed line).

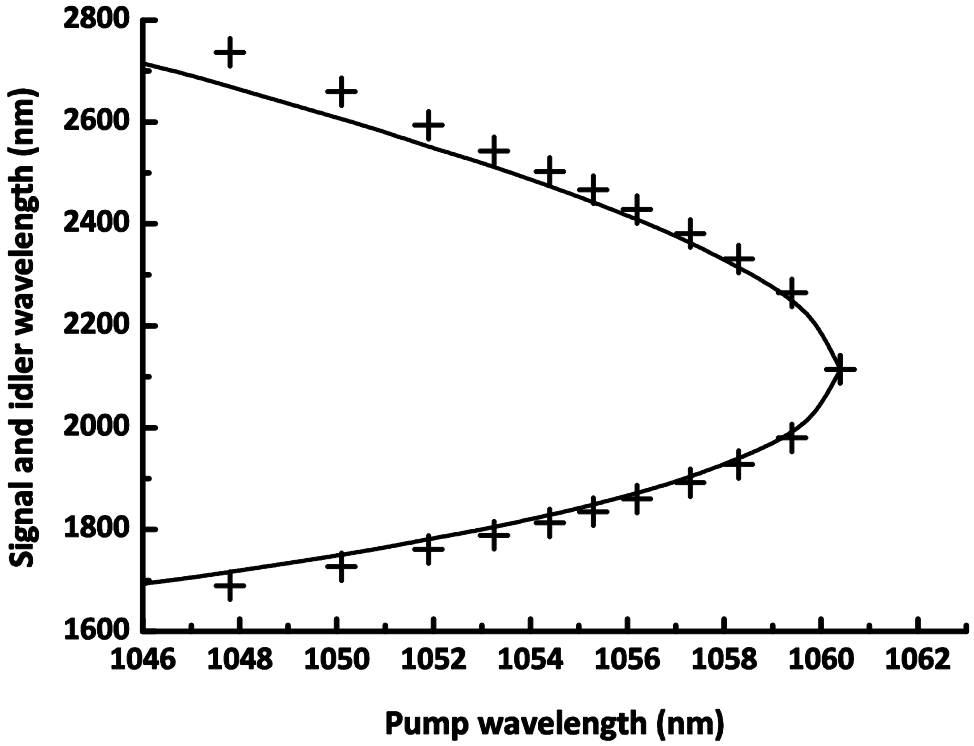

Figure 3.8 PF tuning curve: experimental data (+) and fitting curve for a GaAs thickness t = 271 nm (solid line).

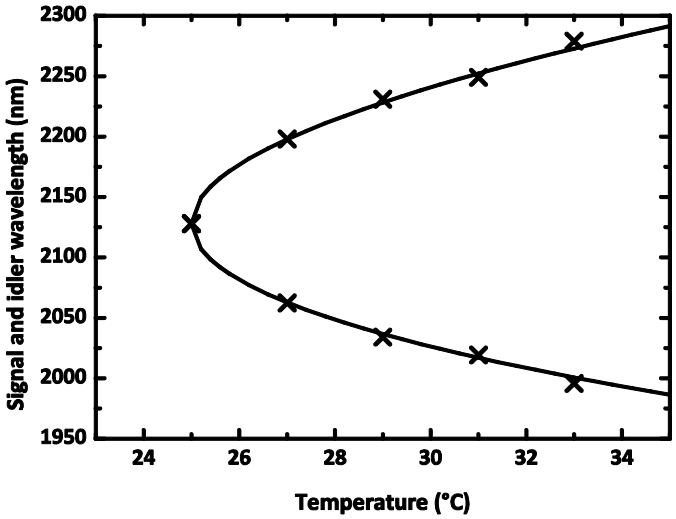

Figure 3.9 Temperature tuning for λ_P = 1062 nm: experimental data (crosses) and calculated curve (solid line).

as fit parameter (t_{fit} = 271 nm, instead of nominal t = 273 nm).[36] This calculated tuning curve differs from its experimental counterpart for a slightly lower tuning aperture, as determined with Eq. 2.3: α = 2.14 for the experimental points, versus α = 1.92 for the fitting curve. We ascribe such difference to the narrow lateral confinement of the ridge, which increases the dispersion of the waveguide (see Section 2.1.2) and thus the aperture of the tuning curve, with respect to the results of 1D modeling.

Parametric tuning can also be obtained by changing the sample temperature, as shown in Figure 3.9. Here experimental data are compared with a simulated curve based on AlGaAs thermorefractive coefficients. [Gehrsitz, 2000]

3.2 Second-harmonic generation experiments

SHG is the reverse of degenerate PF. Both are obtained by injecting just one excitation beam, at ω and 2ω respectively. While in SHG both input photons at ω are provided by the injected field, in PF one of the two input photons is provided by zero-point vacuum fluctuations at ω. As a consequence, while the conversion efficiency of PF depends also on the phase-matching band, that of SHG depends only on the nonlinear overlap integral Γ. Note that the normalized parametric gain coefficient can be directly inferred by Γ through the expression (see Eqs. 1.19 and 1.34)

[36] See Section 2.1.2 for the considerations on the fabrication tolerances.

$$g/\sqrt{P_P} = \sqrt{\frac{8\pi^2|\Gamma|^2}{\varepsilon_0 n_P n_s n_I \lambda_S \lambda_I c}} \ [\mathrm{cm}^{-1}\mathrm{W}^{-1/2}] \tag{3.1}$$

Moreover, for a given injection level, PF power is much lower than SHG power, which grows quadratically with the power at ω. For these reasons, the frequency doubling of a 2 μm field is more suitable than PF to first determine the normalized parametric gain coefficient of our waveguides.

3.2.1 Fundamental frequency source

The 2-3 μm wavelength range does not offer a large choice in terms of laser sources. Available commercial sources, with the exception of recent GaInAsSb/AlGaAsSb and InGaAs/InGaAsP laser diodes, are essentially OPOs. In order to obtain a pump at fundamental wavelength (2 μm) we resorted to DFG in a PPLN crystal. The corresponding inputs are provided by an ELS Versadisk CW Yb:YAG laser (tunable between 1020 nm and 1040 nm) and the Spectra-Physics 3900S Ti:Sapphire laser. The former has a linewidth < 5 MHz, while the latter, with its set of etalons installed, has a linewidth ≈ 1.5 GHz. Ti:Sapphire wavelength is set around 0.7 μm to obtain a DFG field around 2.1 μm. The MgO doped, z-cut PPLN crystal (produced by HCPhotonics) is 4 cm long and 0.5 mm thick, with QPM periods Λ = 15, 15.35, 15.7, and 16.05 μm. Its facets are both AR-coated around 700, 1030, and 2100 nm. Figure 3.10 shows the calculated DFG tuning curves vs. crystal temperature. In practice, the crystal temperature is always kept above 100°C, to reduce the risk of photorefractive damage, due to the intense CW red pump. The calculated phase-matching spectrum (1 nm FWHM) for an idler wavelength of 2128 nm is shown as well. The linewidth of the DFG field is limited by those of PPLN pumping lasers, and thus approximately coincides with that of the Ti:Sapphire.

DFG conversion efficiency is given by Eq. 1.15 for plane waves in an infinite medium. This is a reasonable approximation only if the Gaussian beams focused into the crystal have a broad transverse distribution, staying basically unvaried along the crystal length L. Usually, however, pump beams are strongly focused into the crystal, so as to enhance their intensity: in such cases the plane-wave assumption is not correct. Typically, the beams waist w_0 is set so that the resulting Rayleigh range, $z_0 = \pi n w_0^2/\lambda$, is approximately equal to L/2 (confocal focusing). An exact analysis for optimum focusing leads to z_0 = L/5.68: [Boyd, 1968] for L = 4 cm

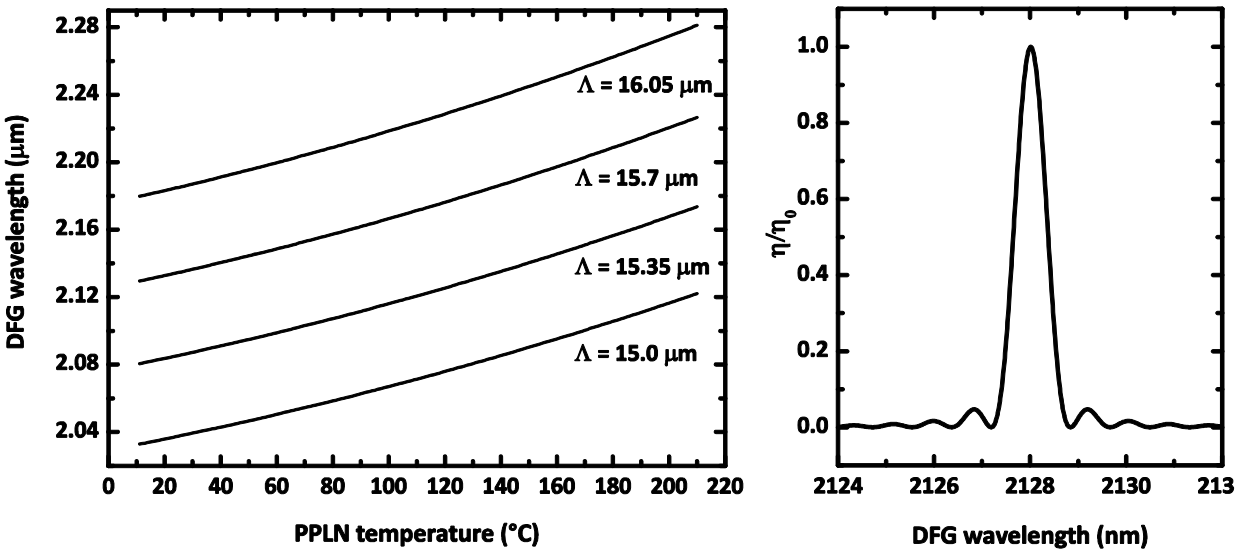

Figure 3.10 Left: PPLN DFG temperature tuning curves for 4 different QPM grating period, λ_S = 1030 nm and 683 nm < λ_P < 709 nm. Right: normalized conversion efficiency vs. wavelength, for Λ = 15.35 μm and T = 125.3 °C.

this corresponds to w_0 = 27 μm at 0.7 μm and w_0 = 33 μm at 1.03 μm. In this configuration, the expected efficiency at phase matching is

$$\frac{P_I}{P_s} \approx \frac{16\pi^2 d_{eff}^2 L P_p}{\varepsilon_0 n_i n_p c \lambda_s \lambda_i^2} \tag{3.2}$$

This value holds true (within 10%) over the range L/3 < z_0 < L/10, [37] making waist adjustment not critical. Accordingly, we simply focus both beams with an f = 200 mm BK7 lens, obtaining w_0 = 30 μm at λ = 0.7 μm, and w_0 = 34 μm at λ = 1.03 μm.[38] By injecting 1 W from each source into the crystal we obtain about 3 mW of generated power at 2.1 μm, rather than the calculated 20 mW. Such discrepancy can be ascribed to the different shapes of the beams before the lens, resulting in a 14 mm shift of one waist respect to the other along the propagation direction. Still, 3 mW are largely sufficient to perform the SHG experiment. With a coupling efficiency as low as 10%, a 3 mW pump is supposed to produce 100 nW of second harmonic power at 1 μm, easily detectable with a standard lock-in amplifier.

3.2.2 Experimental setup

The experimental SHG setup, including the PPLN DFG source, is shown in Figure 3.11. The

[37] Corresponding to 19 μm < w_0 < 35 μm at 0.7 μm, and to 24 μm < w_0 < 45 μm at 1.03 μm.
[38] The spot-size values have been measured by knife-edge beam profiling. [Arnaud, 1971]

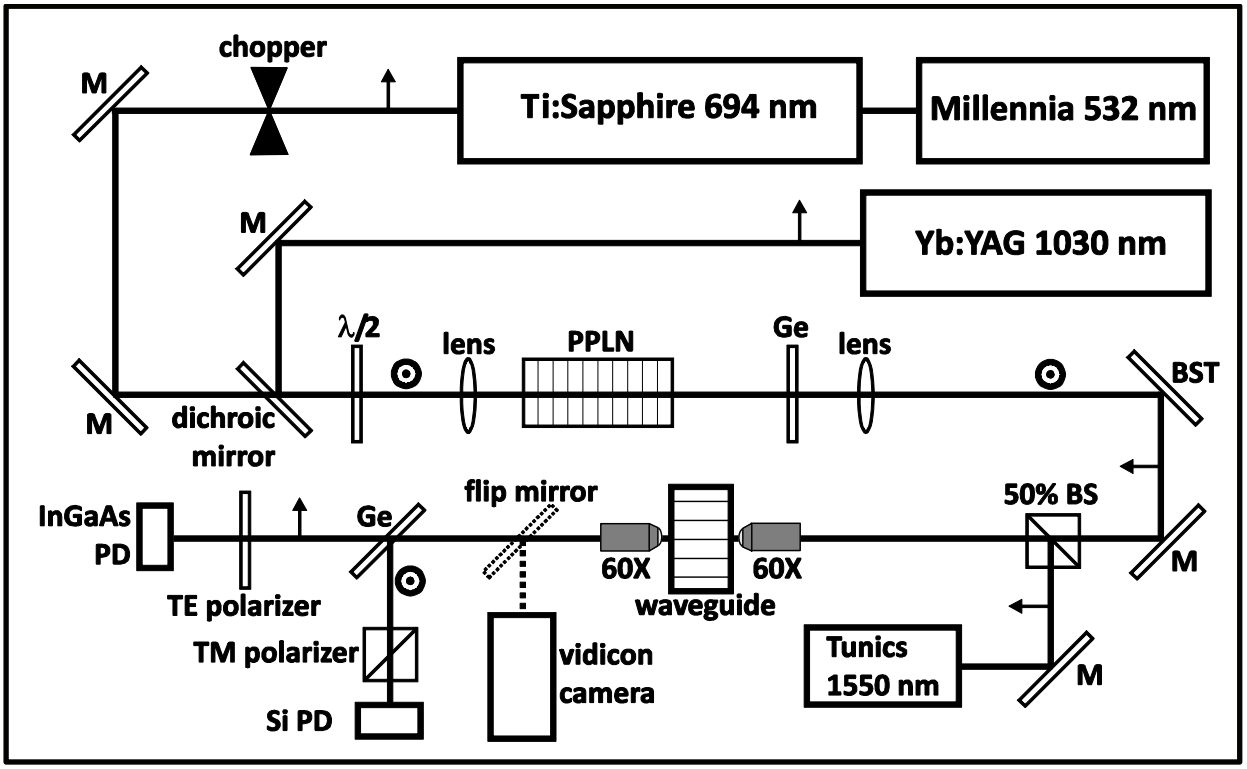

Figure 3.11 Experimental setup for second harmonic generation.

Ti:Sapphire and Yb:YAG sources provide signal (1.03 μm) and pump (0.7 μm) beams to generate the DFG at 2.1 μm in the PPLN. The two beams are combined onto a dichroic mirror and their polarization is aligned along the extraordinary axis of the PPLN with an achromatic wave-plate. At the crystal output, a 3 mm thick Ge window blocks signal and pump. The vertical polarization of the DFG field is then rotated by 90° with a beam steerer, as required for the following interaction in the GaAs waveguide. Finally, the DFG beam at 2 μm is aligned on the optical axis of the waveguide coupling stage. The fields at ω and 2ω at the waveguide output are detected as in PF experiments.

As no imaging facilities at λ = 2.1 μm are available in our laboratory, we resort to an auxiliary beam at 1.55 μm to assist the waveguide input coupling. The two beams at 2.1 μm and at 1.55 μm are combined with a 50% beam-splitter and aligned on the optical axis. With the aid of an IR vidicon camera, the 1.55 μm beam is coupled into the waveguide and successively replaced by the collinear one at 2.1 μm.

3.2.3 Results

The results presented hereafter have been obtained on the same waveguide used for PF

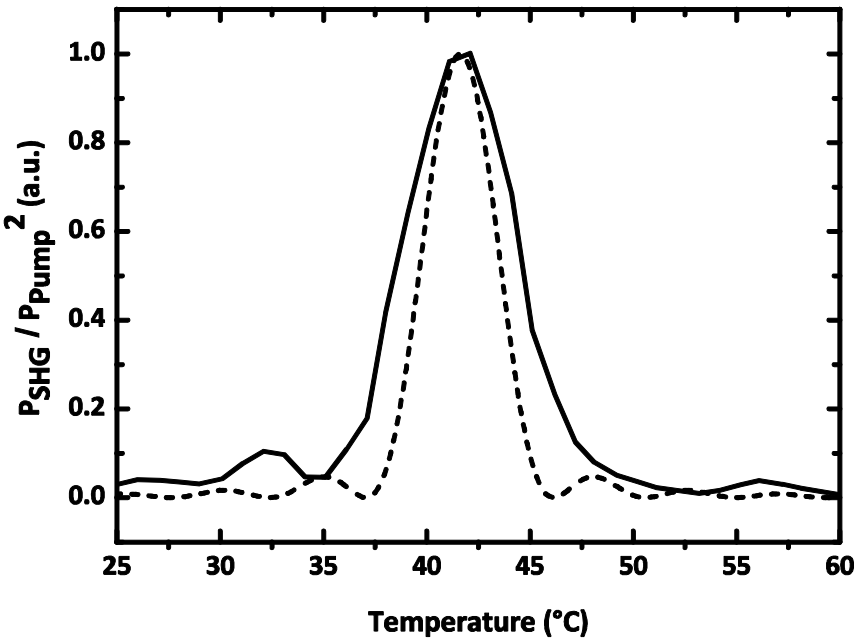

Figure 3.12 SHG normalized temperature detuning curve (L = 3 mm): experimental (solid line) and calculated (dashed line).

experiments of Sections 3.1.2 and 3.1.3 (sample B). The power of the TE polarized input beam at 2120 nm was 1.5 mW, measured before the input objective, with more than 100 μW at the waveguide output. The throughput, lower than that obtained with the Ti:Sapphire at 1.06 μm, is affected: firstly by poor microscope objectives transmission at this wavelength (66%); secondly, by the non Gaussian profile of the ω beam, which stems from the different shape of two beams mixed in the PPLN crystal.

The second-harmonic signal has been found and maximized by tuning the GaAs waveguide temperature. Figure 3.12 shows the normalized temperature detuning curve, compared to its lossless counterpart calculated on the basis of AlGaAs thermorefractive coefficients. [Gehrsitz, 2000] In principle, the deviation from the ideal $sinc^2$ shape may stem from temperature or waveguide inhomogeneities along the propagation direction, as well as propagation losses. However:

1) The drift of the ridge width w is estimated as $\Delta w \approx 100$ nm after SEM observation. Since $\Delta T_{PM}/\Delta w \approx 0.05$ °C/nm for w = 3 μm, this results in a PM temperature shift $\Delta T_{PM} \approx 5$ °C. Such shift is consistent with the experimental broadening, shown in Figure 3.12.
2) The contribution of losses can be neglected, based on the assumption that their value at

λ_ω = 2120 nm and $\lambda_{2\omega}$ = 1060 nm is of the same order than that measured at 1550 nm. [39]

3) We cannot give any quantitative estimate of the effects of temperature inhomogeneity, as we can by no means locally measure the waveguide temperature with sufficient accuracy.

Therefore, the deviation from the $sinc^2$ shape is likely to stem from the only ridge drift, but a contribution of temperature inhomogeneity cannot be excluded.

With the waveguide temperature set for perfect PM, the input power at ω has been varied by means of a variable neutral density filter, and its throughput measured at the waveguide output along with the power at 2ω. The resulting curve, shown in Figure 3.13, exhibits a parabolic trend, as expected, with an internal conversion efficiency $\eta = (130\pm20)\%$ W^{-1}. To our knowledge, this is the highest ever reported for frequency doubling in AlGaAs waveguides and it is comparable with the best results in PPLN waveguides. [Kintaka, 1996] Nevertheless, it is slightly lower than the calculated value η = 210% W^{-1} and such difference can be mainly attributed to three factors:

1) **Propagation losses.** If we suppose these losses equal to the experimental value at 1.55 μm, we obtain η = 170% W^{-1}, closer to the measured one.
2) **Waveguide and temperature inhomogeneity.** The same factors that cause PM-band broadening results also a in lower peak conversion efficiency.
3) **Input coupling.** The non Gaussian profile of the input beam is not perfectly matched to the TE_{00} profile and the waveguide is multimode at ω in the horizontal direction. Accordingly, even if after optimization most power at ω is coupled to the TE_{00}, a fraction of it gets coupled to higher-order modes, which are not phase matched. The power at ω measured at the waveguide output is thus higher than the effective one, resulting in an underestimated conversion efficiency.

The normalized counterpart of the experimental efficiency is η_{norm}=1500±200% $W^{-1}\,cm^{-2}$, which corresponds to a normalized parametric gain $g/\sqrt{P_P}$ = 3.9±0.3 $W^{-1/2}cm^{-1}$. For the above reasons, this value is somewhat lower than the calculated $g/\sqrt{P_P}$ = 4.83 $W^{-1/2}\,cm^{-1}$ (see Section 2.1.2).

[39] See section 5.1.1.

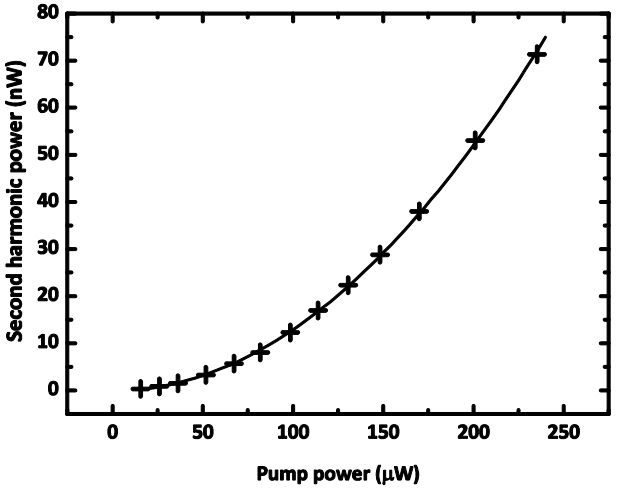

Figure 3.13 Second-harmonic vs. pump internal power: experimental data (crosses) and quadratic fit (solid line).

3.3 Parametric amplification measurements

A DFG experiment can provide a precise knowledge of the two most relevant parameters of a parametric generator: the tuning curve and the gain. Several examples in literature demonstrate the usefulness of such characterization towards the fabrication of integrated parametric devices. This is the case for the first OPOs, in birefringent Ti:diffused [Sohler, 1980; Sohler, 1981] and in QPM proton-exchanged $LiNbO_3$ waveguides, [Bortz, 1995]; and for twin photon sources, namely in proton-exchanged $LiNbO_3$ [Baldi, 1996] and in GaAs waveguides. [Lanco, 2006a; Lanco, 2006b]

In AlOx based frequency converters, so far DFG was only performed in waveguides designed to generate MIR tunable radiation. [Fiore, 1997a; Bravetti, 1998] What we present here is the first exploitation of DFG to characterize the parametric generation in GaAs/AlOx waveguides.

In our waveguides we have already characterized the tunability (with PF) as well as the parametric gain (with SHG). DFG cannot provide any better knowledge on tunability than PF spectra. Conversely, it offers a far better precision than SHG in evaluating the parametric gain. According to Eqs. 1.22 and 1.23, the parametric gain coefficient in the low-gain regime can be written as

$$g = \frac{1}{L}\sqrt{\frac{\lambda_I P_I(L)}{\lambda_S P_S(L)}} \ [\mathrm{cm}^{-1}\mathrm{W}^{-1/2}] \tag{3.3}$$

Near degeneracy, with $\lambda_I \approx \lambda_S$, the measurement of $P_I(L)$ and $P_S(L)$ can be carried out with the same detector so that the ratio $P_I(L)/P_S(L)$ is not affected by calibration uncertainties.

3.3.1 Experimental results

The DFG experimental setup is shown in Figure 3.14. In order to simultaneously inject a 1 μm pump beam and a 2 μm signal beam into the waveguide, we resort to the following configuration. The Yb:YAG beam (1.03 μm) is split by a 50% beam-splitter. The one half pumps the nonlinear waveguide; the other half is mixed in the PPLN crystal with the Ti:Sapphire beam at 0.7 μm to generate the 2 μm signal. As a consequence, the experiment can be carried out only on a sample A, with phase matching at 1.03 μm. The ridge waveguide employed has width w = 3 μm and length L = 3 mm.

The Yb:YAG wavelength and the sample temperature have been chosen so as to set the parametric interaction at degeneracy, in order to achieve the maximum gain, with a very large bandwidth. Accordingly, the Ti:Sapphire wavelength and the PPLN temperature have been set to generate a signal field around 2.06 μm, suitable to be amplified. More in detail, the Yb:YAG wavelength has been set at 1036 nm and that of the Ti:Sapphire at 687 nm, resulting in a 2046 nm beam generated in the PPLN crystal. Both pump and signal beams are collinearly aligned on

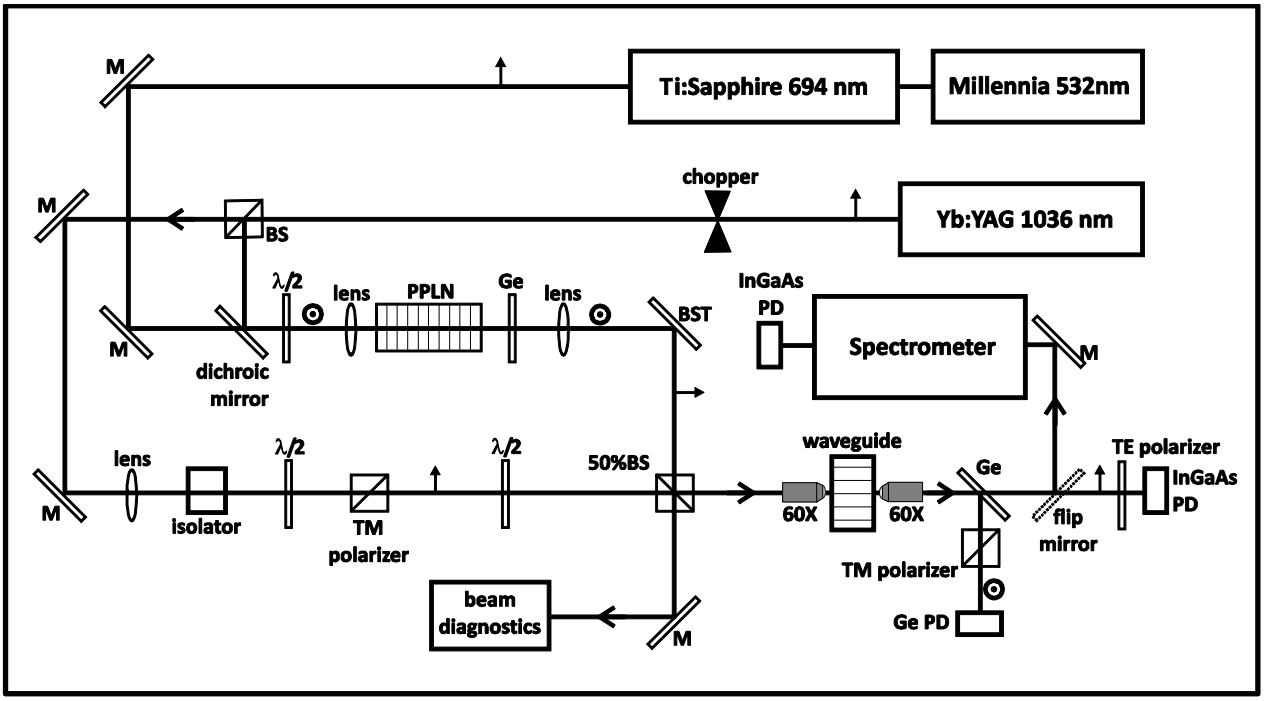

Figure 3.14 DFG experimental setup.

the coupling-stage axis. At the waveguide output, the pump is filtered by a Ge window, whose reflection, after passing through a TM polarizer, is detected by a calibrated Ge photodiode. The 2 μm output, after passing through the Ge filter, is focused into the spectrometer. This is used: firstly, to acquire PF spectra and check the gain band; secondly, to separately measure the power of signal and idler outputs.

At first, a 100 mW TM polarized pump beam at 1030 nm was injected in the waveguide, with its temperature finely tuned to exactly set parametric gain at degeneracy, as shown in Figure 3.15 (dotted line). Then, a 500 μW TE signal beam at 2046 nm was coupled, obtaining the output spectrum reported in the same figure at a different scale (solid line). This shows the amplified signal and a clear idler peak at 2099 nm.

Finally, the powers of signal and idler, filtered with the spectrometer, were measured as a function of the coupled pump power.[40] Figure 3.16 shows the idler-to-signal ratio vs. TM coupled pump power, which is well fitted by a straight line as expected from Eq. 3.3. The slope,

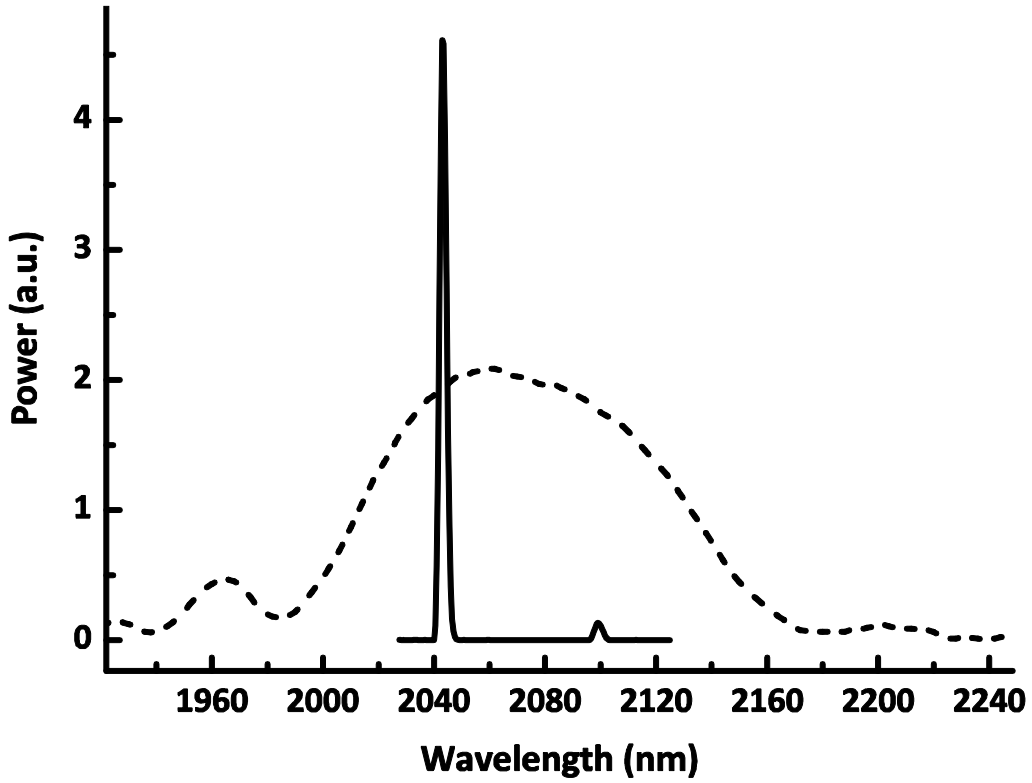

Figure 3.15 Waveguide output spectra: amplified signal and idler (solid line) resulting from pump and signal simultaneous coupling, and PF obtained with the only input pump (dashed line).

[40] In order to keep fixed the waveguide temperature, we have varied the pump polarization rather than its power (as also done in PF experiments).

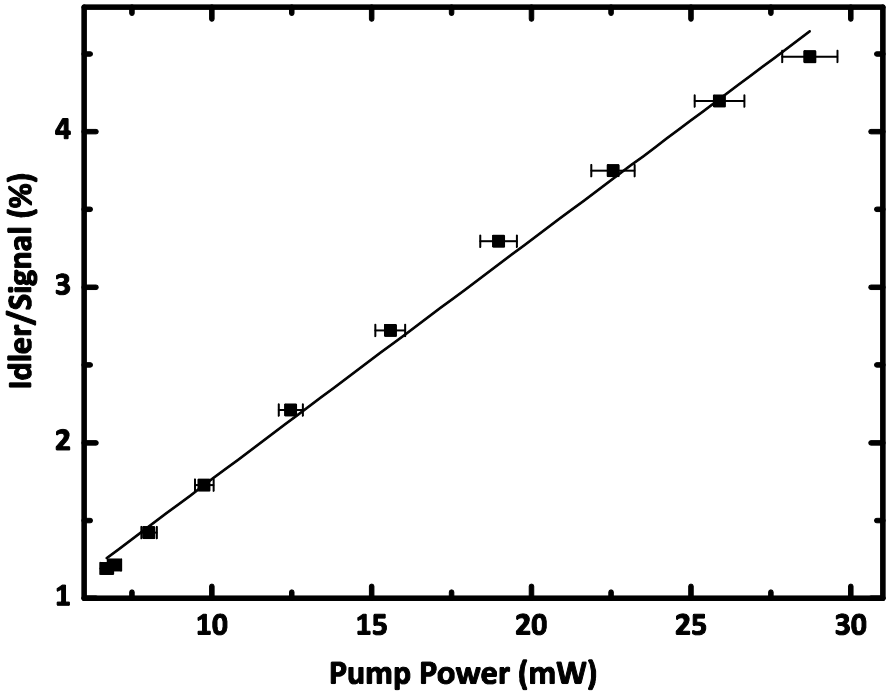

Figure 3.16 Output idler-to-signal percentage, i.e. parametric amplification, vs. coupled pump power.

scaled to the waveguide length L, gives the normalized gain coefficient $g / \sqrt{P_P} = 4.1 \pm 0.1$ cm^{-1} W$^{-1/2}$ in good agreement with the value obtained in the SHG experiment, and with a far better accuracy. The corresponding parametric amplification is $G = P_S(L)/P_S(0) - 1 \approx (gL)^2 = 4.5$ %, which is the highest value ever reported in a semiconductor waveguide.

3.4 Chapter conclusion

In order to explore the features of parametric generation in our AlGaAs/AlOx waveguide, i.e. efficiency, tunability and bandwidth, we have performed a few crossed experiments of frequency conversion.

At first, we have studied PF, in terms of efficiency and tunability. In agreement with expectations, signal and idler wavelengths can span a few-micron range, by tuning pump wavelength or sample temperature. The high waveguide quality, verified at first by SEM observations, has been confirmed by the acquired generation spectra. Thanks to high-power pumping we have obtained PF beyond the low gain regime and observed a nonlinear dependence of signal and idler on the pump intensity. The corresponding conversion efficiency is in good agreement with the expected value.

To measure the parametric gain coefficient, we have first performed a frequency doubling experiment. To this end, a 2 μm DFG source based on a PPLN crystal has been designed and assembled. We have obtained a record SHG conversion efficiency (normalized conversion efficiency) for GaAs waveguides, of 130 W^{-1} (1500 $W^{-1}\,cm^{-2}$), in good agreement with the calculated values. This confirms our technology as the most performing at present in the field of semiconductor integrated nonlinear optics.

Finally we have reported the first demonstration of parametric amplification in semiconductor waveguides. On a 3 mm interaction length a signal amplification of 4.5% has been obtained with 30 mW of pump power. In passing, this experiment has provided us with a more accurate evaluation of parametric gain coefficient.

All the experiments have provided consistent results: a parametric gain coefficient $g / \sqrt{P_P} \approx 4\ cm^{-1}\ W^{-1/2}$ has been determined in both up- and down- conversion, close to the calculated 5 $W^{-1/2}cm^{-1}$. This experimental value is fully compatible with the measured PF efficiency. The performances achieved in all the above experiments are encouraging towards the achievement of a monolithic parametric oscillator around 2 μm.

4 Towards a GaAs/AlOx integrated OPO

Besides compactness, integrated OPOs offer a series of further advantages in comparison to their bulk counterparts, namely: a lower oscillation threshold, a higher stability with respect to ambient fluctuations, and guaranteed single-spatial-mode emission. Moreover, they lend themselves to monolithically integrate components such as electro-optical tunable filters, phase and amplitude modulators, wavelength-selective Bragg reflectors etc. Moreover, for an integrated OPO based on a direct band-gap semiconductor like GaAs, there is the exciting perspective of pump-laser integration.

To date, all the existing integrated OPOs have been fabricated in $LiNbO_3$, whose mature technology has allowed the exploitation of a high nonlinear coefficient in several-cm-long, low-loss waveguides. Several examples of these devices have been reported in the last 30 years, from two groups: Fejer's at Stanford University (USA) and Sohler's at the University of Paderborn (Germany). While the former group has chosen an approach based on proton-exchanged waveguides, the latter has focused on the Ti-diffused counterparts.

Hereafter, in Section 4.1 we briefly illustrate the history of integrated OPOs and the present state of the art. In Section 4.2 we discuss a possible configuration for a GaAs/AlOx integrated OPO, providing an estimation of its oscillation threshold and describing its tuning characteristics. Finally, in Section 4.3 we detail the design and the fabrication of our first integrated mirrors, discussing the related results and perspectives.

4.1 $LiNbO_3$ integrated OPO: state of the art

Guided-wave parametric oscillation was firstly obtained in 4 cm long birefringently phase-matched Ti:$LiNbO_3$ waveguides, in a singly-resonant OPO (SROPO), with a 7.6 W (peak) threshold. [Sohler, 1981] Tunable frequency conversion was obtained from the visible (λ_P = 0.6 μm) to the near infrared (0.95 μm < λ_S, λ_I < 1.6 μm), by varying the waveguide temperature between 170 and 230 °C. The measured nonlinear efficiency was η_{norm} = 0.5% $W^{-1}cm^{-2}$. The same waveguide design was employed eight years later in a doubly-resonant OPO (DROPO), with an oscillation threshold of only 27 mW (CW). [Suche, 1988]

The first QPM-based integrated OPO was demonstrated in proton-exchanged waveguides. Such phase-matching scheme, besides room-temperature operation, allows to

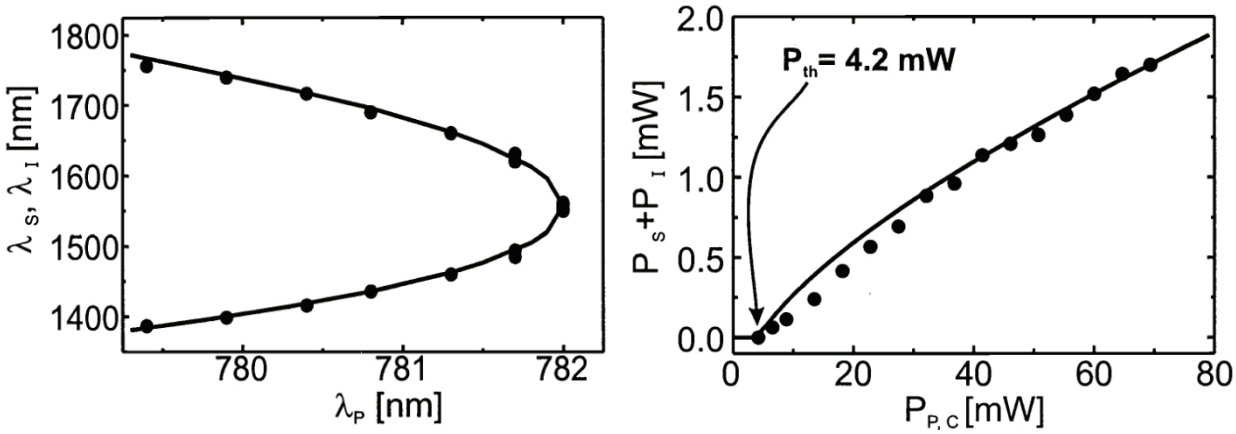

Figure 4.1 Experimental tuning curve (left) and output power vs. pump power (right) for the Ti:diffused QPM OPO in the NIR (from Ref. [Schreiber, 2000]).

exploit the χ_{zzz} $LiNbO_3$ diagonal nonlinear coefficient, far larger than the χ_{xxz} employed in birefringent PM ($\chi_{zzz} \approx 6\times\chi_{xxz}$). After the first reported threshold of 4 W, affected by non-optimized waveguide processing and pump source broad linewidth, [Bortz, 1995] a considerably lower threshold was obtained in 1997, with η_{norm} = 43% $W^{-1}cm^{-2}$ and waveguide propagation losses of 0.6 dB/cm. In a 2.4 cm long cavity, the corresponding oscillation threshold was 1.6 W, still severely affected by non-optimum coupling of the pump beam.[41] By varying λ_P between 0.75 μm and 0.77 μm, signal and idler were tuned between 1.2 μm and 2.1 μm, with maximum P_S = 220 mW. [Arbore, 1997]

The last ten years have witnessed the success of a novel technology, based on QPM Ti:$LiNbO_3$ waveguides, with losses as low as 0.1 dB/cm in the NIR and 0.03 dB/cm in the MIR, and high waveguide homogeneity over up to 10 cm of length. The excellence of such features, combined with the deposition of dielectric coatings on the waveguide facets,[42] has allowed to reduce the oscillation threshold of integrated OPOs of almost one order of magnitude. [Schreiber, 2000] The first DROPO based on this technology was pumped at 780 nm, had an oscillation threshold of 4.2 mW (coupled power) and a slope efficiency of 3%. As shown in Figure 4.1, signal and idler tuning range went from 1.4 μm to 1.75 μm, limited by the bandwidth of the integrated mirrors.

[41] The waveguide was multimode at λ_P and 60% of the pump power was coupled to non-phase-matched higher-order modes.

[42] In previous demonstrations, the OPO cavity was formed by external mirrors put in contact with the waveguide facets. Ref. [Arbore, 1997] reports additional losses of 2% for each facet, due to this solution.

An additional advantage of Ti-diffused waveguides is the broader transparency region with respect to that of proton-exchanged waveguides, which are affected by an absorption peak around 2.7 μm, related to the O-H stretching vibrations. [Korkishko, 2003]

Solher's group has benefited from such available transparency range to demonstrate guided-wave parametric oscillation in the MIR, with a 1.55 pump and a tuning range between 2.7 and 3.5 μm. The singly-resonant configuration had a pump threshold of 275 mW and a slope efficiency of 30%, with maximum output power P_I+P_S = 300 mW for P_P = 1.25 W. [Hofmann, 2000] The doubly-resonant version had a pump threshold of 14 mW, with maximum output power P_I+P_S = 6.5 mW for P_P = 300 mW. [Hofmann, 1999]

4.2 GaAs/AlOx integrated OPO: design and expected performances

In the above overview we have emphasized the key role of optical losses in integrated OPOs, due to the typical weakness of parametric gain in CW and quasi-CW regimes. In GaAs/AlOx waveguides, attenuation coefficients one order of magnitude higher than in $LiNbO_3$ have prevented so far the demonstration of an integrated OPO, in spite of their far higher nonlinearity. Note that, in all the examples previously mentioned, η_{norm} ranges from 0.5 to 43 $W^{-1}cm^{-2}$, to compare with η_{norm} = 1500 $W^{-1}cm^{-2}$ of our waveguides. However, low $LiNbO_3$ losses allow using several-cm-long waveguides, with an overall conversion efficiency around 100 W^{-1}, comparable with that obtained in our few-millimeter-long waveguides (see Section 3.2.3). In addition, low losses result in a high damage threshold, allowing pump powers up to a few Ws. On the basis of the experimental features of our FB parametric generators, hereafter we describe the design criteria and the possible characteristics of an integrated GaAs/AlOx OPO.

4.2.1 Cavity configurations and oscillation threshold

The first choice to deal with for the design of the OPO cavity, is between a singly- or doubly-resonant configuration. While the former solution has well-known advantages in terms of stability and tunability,[43] the latter exhibits a far lower oscillation threshold. [Sutherland, 1996] With our parametric gain coefficient and propagation losses, the steady-state pump threshold of a SROPO (Eq. 1.27) is $P_P^{(th)}$ = 250 mW, for a waveguide length L = 3 mm and a facet reflectivity

[43] This subject will be discussed in detail in Section 4.2.2.

R = 95%.[44] For a DROPO (Eq. 1.28), in the same conditions, the pump threshold is one order of magnitude lower: $P_P^{(th)}$ = 23 mW. The maximum power we can couple in our waveguide, at present limited to about 100 mW, prevents the adoption of the former configuration. Conversely, it is perfectly adapted to the latter, as, theoretically, the maximum conversion efficiency (50%) in a DROPO is reached at four times threshold pumping. [Siegman, 1962]

For a symmetric integrated resonator, with equal signal and idler losses, the pump power threshold of an integrated DROPO can be expressed as: [Bava, 1987]

$$P_P^{(th)} = \frac{1}{\eta_{norm}}\left[\frac{\alpha_P/2}{1-\exp(-\alpha_P L/2)}\ln\left(Q+\sqrt{Q^2-1)}\right)\right]^2 \tag{4.1}$$

where η_{norm} is the waveguide normalized conversion efficiency and

$$Q = \frac{1+R_S R_I \exp(-2\alpha L)}{(R_S+R_I)\exp(-\alpha L)} \tag{4.2}$$

with $R_{S,I}$ the facet reflectivity at signal and idler wavelength, and $\alpha = \alpha_I$, α_S the signal and idler losses. With respect to Eqs. 1.27 and 1.28, Eq. 4.1 introduces the pump losses through a position-dependent gain function

$$G(x) = g\left[\frac{1-\exp(-\alpha_P L/2)}{\alpha_P/2}\right] \tag{4.3}$$

with G(x) = gL in the limit $\alpha_P \to 0$. In such limit the threshold gets lower for increasing length L of the nonlinear medium and vanishes for $L \to \infty$. Conversely, for $\alpha_P \neq 0$, there's an optimum length for which the threshold is lowest. Such behavior is illustrated in Figure 4.2 where, assuming $\alpha = \alpha_P$, α_I, α_S, we have plotted the calculated pump threshold at degeneracy of our waveguides, for three typical values of the attenuation coefficient and R = $R_{S,I}$ = 95%. For 0.7 $cm^{-1} > \alpha > 0.4\ cm^{-1}$ the optimum length increases from 6 mm to more than 1 cm, and the corresponding $P_P^{(th)}$ decreases from 55 mW to less than 20 mW. However the curves are quite flat around the minimum, making L value not critical. Since fabricating waveguides longer than

[44] R > 95% at 1.55 μm is the value reported by Schreiber et al. [Schreiber, 2000] for the facet dielectric coating of the 4.2 mW threshold $LiNbO_3$ integrated DROPO.

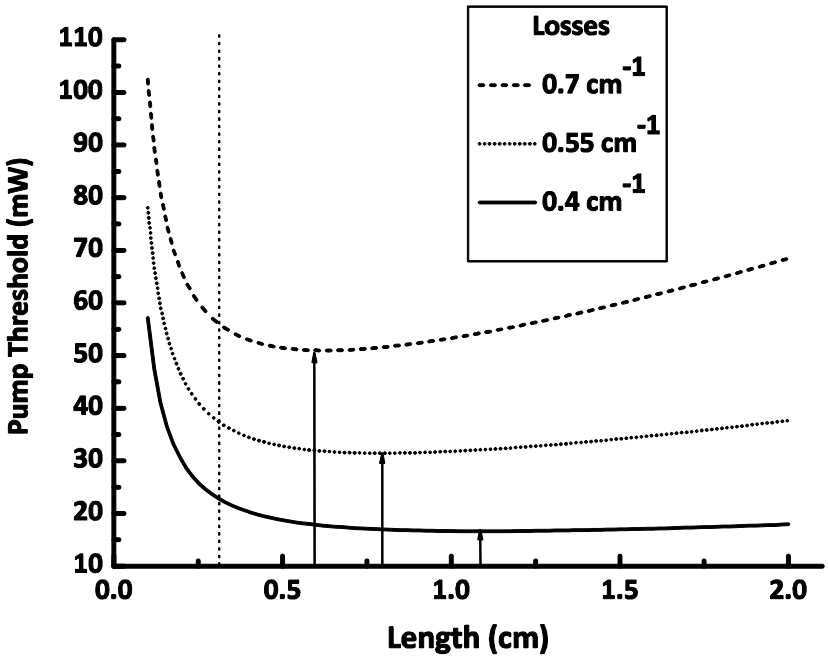

Figure 4.2 Expected pump threshold of the GaAs/AlOx integrated DROPO vs. waveguide length, for three typical values of the attenuation coefficient and R = 95%. We pointed out the lengths corresponding to threshold minima and the typical length of our samples L = 3 mm.

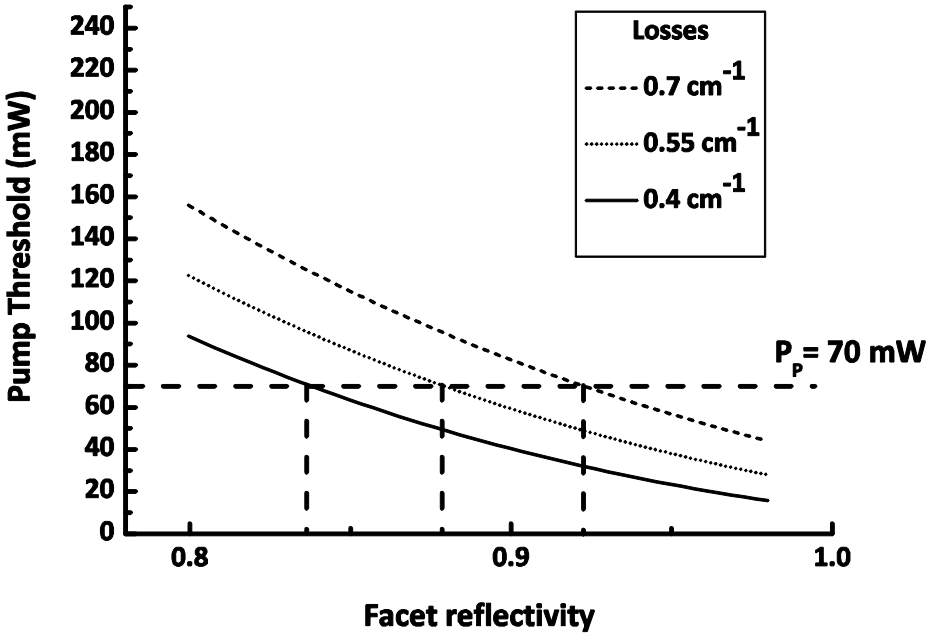

Figure 4.3 Expected pump threshold of the GaAs/AlOx integrated OPO vs. facet reflectivity, for three typical values of the attenuation coefficient and L = 3mm. The horizontal dashed line indicates the pump power we can safely couple without damaging the waveguide facet.

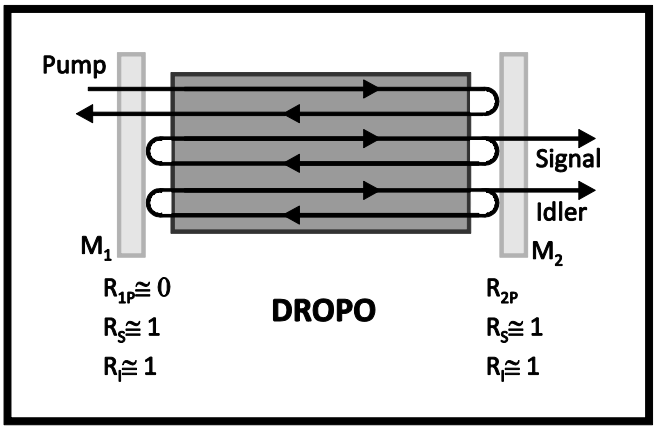

Figure 4.4 Scheme of double-pass DROPO.

few mm with a good uniformity is made difficult by wet etching intrinsic drawbacks,[45] in practice we opted for a length L = 3 mm.[46] We stress that in a non-uniform waveguide the effective nonlinear interaction length is shorter than L, while losses are experienced all along the waveguide length L. Therefore, in such a case, a longer cavity results in a higher threshold.

In Figure 4.3 $P_P^{(th)}$ is traced versus the facet reflectivity R, for the same three values of losses and L = 3 mm. Here we have pointed out the pump level P_P = 70 mW, i.e. the typical value we can couple without exposing the waveguide facet to the risk of optical damage. For 0.4 $cm^{-1} > \alpha > 0.7$ cm^{-1}, the minimum reflectivity required for oscillation ranges between 84% and 92%. In other words, in the typical range of attenuation coefficient of our waveguides, threshold is expected to be within reach with a reasonable facet reflectivity.[47]

An interesting means to lower the OPO threshold, in both singly- and doubly-resonant configuration, is to double pass the pump through the cavity, as shown in Figure 4.4. This can be readily obtained by employing the pump input cavity mirror M1 highly transmitting at λ_P and the opposite one (M2) highly reflective. In this configuration, parametric amplification is experienced in both propagation directions in the nonlinear crystal. Accordingly, with respect to Eq. 1.27, the SROPO threshold condition becomes [Bjorkholm, 1970]

$$(g_{th}L)^2 = \frac{2\left[1 - R_S \exp(-\alpha_S L)\right]}{1 + R_{2P}} \tag{4.4}$$

[45] Etching large wafer portions generally results in an inhomogeneous etched depth. In particular the etching rate is higher on the sample edges, where the etching solution refresh is faster with respect to the center.

[46] In the most critical case considered, i.e. for α = 0.7 cm^{-1}, the threshold for L = 3 mm is only 10% higher than for the optimum length, while for α = 0.55 cm^{-1} the relative increase is 20%.

[47] Several diode lasers manufacturers report facet dielectric coatings with a reflectivity > 95% in the NIR.

with R_{2P} the pump reflectivity of M_2. For R_{2P} = 1 the threshold of the double-pass SROPO is lowered of a factor 2 with respect to the single-pass case. The analysis of a double-pass DROPO is more complicated, due to key role of the relative phases of the three interacting waves upon reflection. In this case the threshold condition, for $\Delta k \neq 0$, is expressed by [Bjorkholm, 1970]

$$(g_{th}L)^2 = \frac{\left[1 - R_S \exp(-\alpha_S L)\right]\left[1 - R_I \exp(-\alpha_I L)\right]}{1 + r_{2P}^2 + 2r_{2P}\cos(\Delta\varphi + \Delta kL/2)}\left[\frac{\sin\left(\frac{\Delta kL}{2}\right)}{\left(\frac{\Delta kL}{2}\right)}\right]^{-2} \tag{4.5}$$

where r_{2P} is the reflection coefficient of M2 and $\Delta\varphi = \varphi_P - \varphi_S - \varphi_I$ the relative phase shift upon reflection. Let us consider the case r_{2P} = 1 and Δk = 0: if $\Delta\varphi$ = 0, i.e. the phase relation between the three waves is maintained upon reflection, the overall interaction length is 2L and the round-trip gain is four times the single-pass gain; hence the corresponding threshold is four times lower than for r_{2P} = 0. Conversely, if $\Delta\varphi = \pi$ the round trip net gain is zero and the threshold infinite. In this case, however, the round-trip gain is not zero for $\Delta k = (k_P - k_S - k_I) \neq 0$,

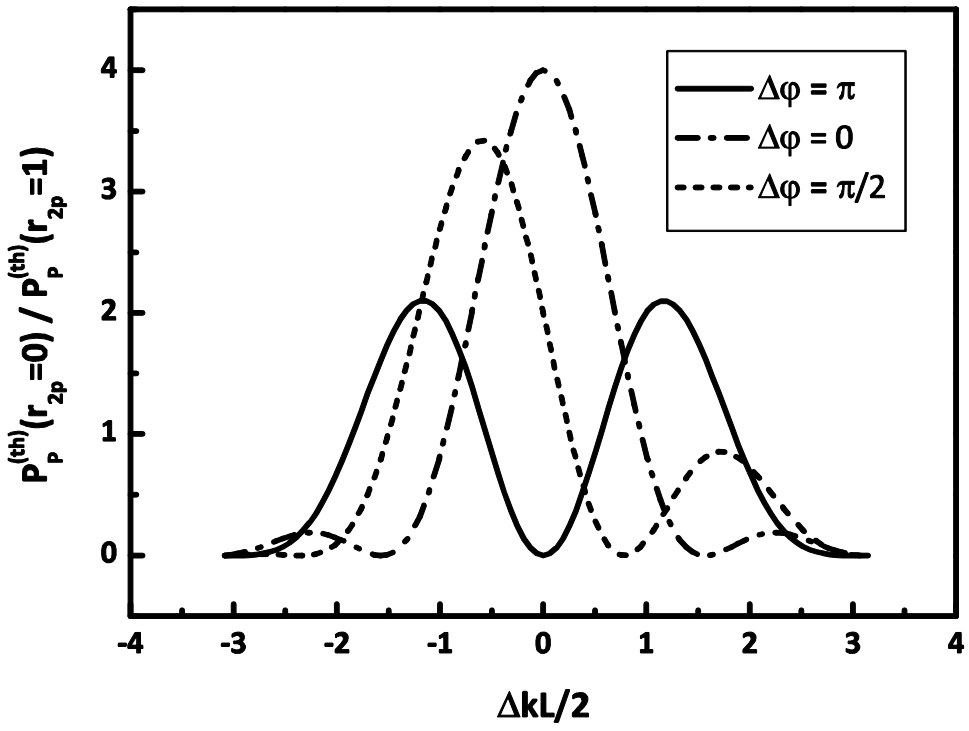

Figure 4.5 The ratio of the single pass DROPO threshold (Δk=0) to the double pass DROPO threshold vs. $\Delta kL/2$ for r_{2p}=1 and three values of $\Delta\varphi$.

and it is maximum for $\Delta kL/2 \approx -0.375\Delta\varphi$. [Bjorkholm, 1970] In any case, the oscillation will occur for the value of $\Delta kL/2$ that minimizes the threshold. Figure 4.5 shows the relative threshold reduction factor with respect to the single pass case, for $r_{2P} = 1$ and for a few values of $\Delta\varphi$: in the worst case, i.e. for $\Delta\varphi = \pi$, the oscillation threshold is half than in the single-pass configuration. Also the conversion efficiency benefits from the double pass for the pump: for $R_{2P} = 1$ and $\Delta\varphi = 0$, the maximum theoretical conversion efficiency, reached for $P_P = 4P_P^{(th)}$, is 100%, i.e. twice the value attainable for $R_{2P} = 0$. The main disadvantage of the double-pass DROPO is that the threshold and the Δk optimum value (i.e. the oscillation frequency) vary with $\Delta\varphi$. In other words, the threshold depends on the mirror employed and can vary when the output wavelengths are tuned. However, the significant reduction in terms of pump threshold achieved with this scheme has induced us to adopt it as our first cavity configuration.

4.2.2 Tunability

As mentioned in Section 1.1.4, the emission wavelengths of an OPO are determined by frequency ($\omega_S+\omega_I=\omega_P$) and momentum ($k_S+k_I=k_P$) conservation. In this respect, singly- and doubly-resonant configurations exhibit considerable differences. Let us consider first the case of the SROPO. Momentum conservation defines the parametric gain band, which can be tuned by changing the temperature or the orientation of the nonlinear medium, as well as pump wavelength. Within the gain band, the possible frequencies fulfilling energy conservation for the resonant signal field are given by the discrete set of longitudinal modes

$$\omega_S = \pi m_s c/L_s \tag{4.6}$$

with m_s the mode number and L_s the optical length of the cavity at ω_S. Hence, SROPO operation is only possible at such frequencies and at the corresponding idler frequencies $\omega_I = \omega_P - \omega_S$. These frequencies are typically tuned by changing the length of the cavity. As in a laser with homogeneous line broadening, the signal oscillating mode is simply the one which minimizes the phase mismatch and thus experiences the maximum gain. In practice, the energetic pulsed pump sources required to reach the threshold of a SROPO[48] hardly operate on a single mode and with a stable emission wavelength, especially if not appropriately isolated from OPO

[48] Due to their high threshold, SROPOs are typically pumped by high peak-power pulsed sources, unlike DROPOs, whose threshold is generally accessible with a CW pump. [Sutherland, 1996]

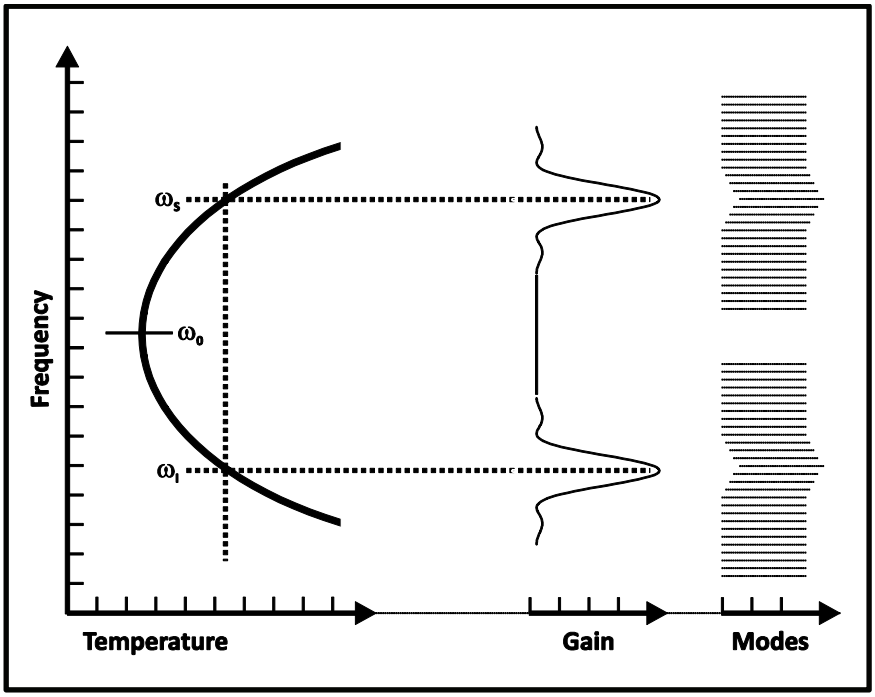

Figure 4.6 Typical DROPO tuning curve near degeneracy. Signal and Idler frequencies are shown as a function of the tuning parameter, in this case temperature. For a fixed value of temperature, single-pass parametric gain exists in bands that are centered on the phase-matching wavelengths, as shown on the gain column. Frequencies available for oscillation belong to the discrete set of cavity resonances. Oscillation thus requires that a pair of signal and idler axial modes in the gain band fulfills frequency conservation. (adapted from Ref. [Eckardt, 1991])

reflections. In addition, the often inadequate degree of mechanical stability of bulk OPO cavities results in continuous frequency shifts of the cavity resonances, and thus mode hops. As a consequence, SROPOs are in general multimode sources, where stable single-mode operation can only be obtained with the additional use of a frequency-selective element, namely an etalon. [Sutherland, 1996] Only after the advent of stable monochromatic ns pump sources and the improvements in cavity design and fabrication, spontaneous singly-resonant oscillation on a single mode has become practically attainable. [Kozlovsky, 1988; Yang, 1993; Yang, 1994]

DROPOs are more complicated, since the frequencies available for oscillation form a discrete set in both signal and idler gain bands

$$\omega_S = \pi m_s c/L_s \, , \, \omega_I = \pi m_I c/L_I \qquad (4.7)$$

as shown in Figure 4.6. Hence, a DROPO is overconstrained, and in general phase matching, frequency conservation and Eq. 4.7 cannot be satisfied simultaneously. [Ebrahim-Zadeh, 2000] A useful tool for understanding the requirement for simultaneous cavity resonances is a

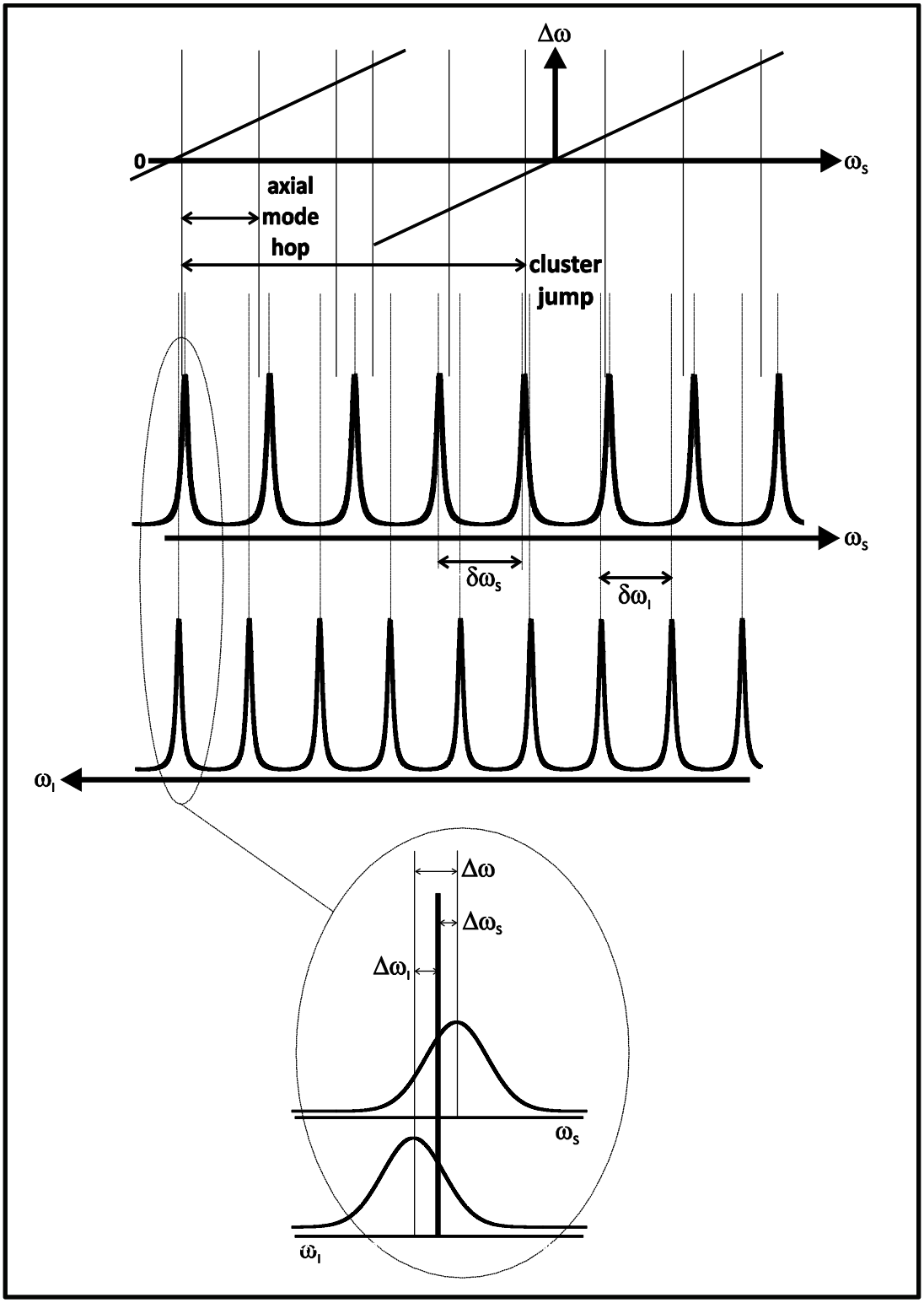

Figure 4.7 Relationship between the DROPO signal-idler resonance frequencies and the condition of energy conservation. The detail shows the frequency mismatch $\Delta\omega$ for a mode pair and its components $\Delta\omega_s$ and $\Delta\omega_i$, which are the frequency displacements from the centers of signal and idler cavity resonances to the frequency most favorable for parametric oscillation (adapted from Ref. [Eckardt, 1991]).

diagram of the type used in Ref. [Giordmaine, 1966]. In this diagram, reported schematically in Figure 4.7, the cavity resonances near the oscillating signal and idler frequencies are plotted as a function of the respective frequencies. Let the signal frequency increase from left to right on a linear scale. The idler frequency scale is determined by $\omega_I = \omega_P - \omega_S$, such that a vertical line drawn through the diagram will give the signal and idler frequencies that satisfy energy conservation.

If a signal-idler resonance pair is perfectly aligned on a vertical line it fulfills the simultaneous resonance condition. Still, such pair is not necessarily phase matched: therefore the corresponding steady state oscillation condition is given by Eq. 4.5 for $r_{2P} = 0$, with a key role of the sinc^{-2} factor.

In general, the condition of simultaneous resonance is not fulfilled. However, due to the finite linewidth of the cavity resonances, oscillation can occur also for a signal-idler mode pair not perfectly aligned. In this case, the corresponding oscillation threshold is in general higher. Let us define the frequency mismatch $\Delta\omega$ as the signal-idler-pair frequency shift that is required to bring the two resonances into perfect coincidence. Due to the different FSR for signal and idler, $\delta\omega_I$ and $\delta\omega_s$, frequency matching occurs at frequency intervals, with "clusters" of well matched adjacent mode pairs, as shown in Figure 4.7.

A mismatch $\Delta\omega \neq 0$ results in a round trip dephasing, i.e. an intensity reduction for both signal and idler modes. Then the oscillation threshold of a given mode pair depends on the degree of both frequency matching and PM. It is convenient to express the frequency mismatch as the sum of two components: $\Delta\omega = \Delta\omega_S + \Delta\omega_I$. $\Delta\omega_S$ ($\Delta\omega_I$) is the frequency shift from the peak of the signal (idler) resonance to the frequency that is most favorable for oscillation for that mode pair. For a given mode pair, the steady state oscillation condition can then be expressed as [Padgett, 1994]

$$(g_{th}L)^2 \approx \frac{\pi^2}{F_S F_I}\left[1+\left(\frac{2\Delta\omega F_S F_I}{F_S\Delta\omega_I + F_I\Delta\omega_S}\right)^2\right]\left[\frac{\sin\left(\frac{\Delta kL}{2}\right)}{\left(\frac{\Delta kL}{2}\right)}\right]^{-2} \tag{4.8}$$

where F_S (F_I) is the finesse of the cavity at signal (idler) wavelength. According to Eq. 4.8, modal selection can be dominated either by the PM condition, or by frequency matching.

At or near degeneracy, where $\omega_S \approx \omega_I$, each cluster contains many mode pairs and the central mode pair will always have a good overlap. In this case, the mode pair at the center of the cluster with the lowest Δk will have the lowest threshold. Far from degeneracy the situation is more complicated, as the cluster with the lowest phase mismatch may not necessarily include the pair with the lowest frequency mismatch.

DROPO tuning may be accomplished by changing the crystal temperature or the pump wavelength. These parameters affect both the PM spectrum and the alignment of signal-idler mode pairs, thus resulting in a hop from a mode pair to different one. Frequency tuning can occur in two possible ways: through an axial mode hop or through a cluster jump. As a tuning parameter is varied, a better frequency matching can be attained with adjacent signal and idler axial modes (i.e. in the same cluster). In this case it becomes advantageous for the oscillation frequencies to hop to the adjacent modes, i.e. to one higher and the other lower in frequency. For larger variations of the tuning parameter, the signal and idler oscillation frequencies progress along adjacent mode pairs within a cluster, in a series of mode hops, until another cluster more closely fulfills phase matching. At that point, the oscillation is shifted to the next cluster, resulting in a larger discontinuous frequency shift, referred to as cluster jump.

Let us consider now the resonator composed by a GaAs/AlOx parametric generator and two integrated mirrors with $R_I = R_S = 95\%$. We assume L = 3 mm and $\alpha_I = \alpha_S = 0.5$ cm^{-1}, resulting in a finesse $F_{S,I} \approx 16$. By calculating the effective indices of signal and idler modes in the PM bands, we have determined the cavity FSRs, $\delta\omega_I$ and $\delta\omega_S$ all over the tuning range of interest. Figure 4.8 shows the number of the phase-matched signal resonances vs. λ_S. As expected, the number of axial modes significantly increases getting close to degeneracy, because of the corresponding broadening of the PM spectrum. This curve is independent of the waveguide length L, because both PM bandwidth and $\delta\omega_{I,S}$ are inversely proportional to L.[49] Conversely, the number of clusters is almost constant all over the investigated wavelength range. Indeed, it is equal to the ratio between the total number of modes in the PM bandwidth and the number of modes $M_{cl} = \delta\omega_I/(\delta\omega_S - \delta\omega_I)$ included between the centers of two adjacent clusters, which enormously grows at degeneracy, where $\delta\omega_S \approx \delta\omega_I$.

[49] The free spectral range is equal to $\delta\omega_{I,S} = c\pi/n_{I,S}L$ while the PM bandwidth (FWHM) is $\Delta k_{PM} = 2.784/L$. [Sutherland, 1996]

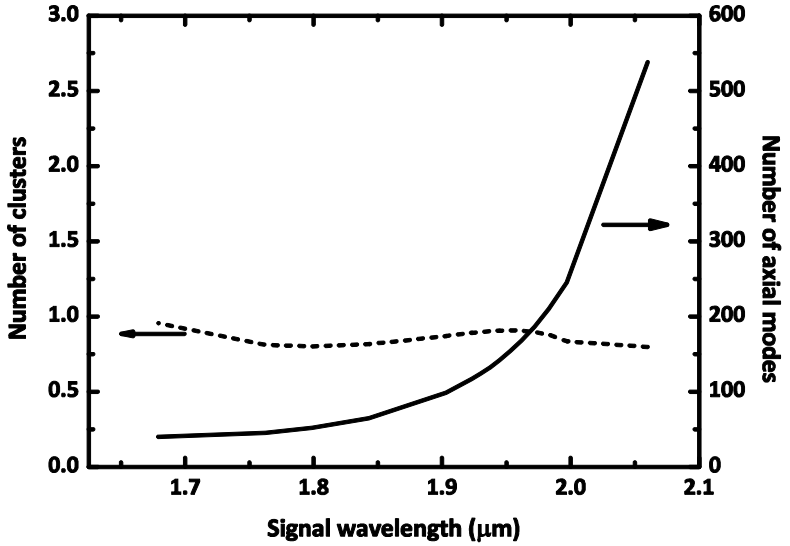

Figure 4.8 Number of phase-matched axial modes (solid line) and clusters (dashed line) in the OPO resonator formed by a sample A with $R_S = R_I = 95\%$, L = 3 mm and $\alpha_S = \alpha_I = 0.5\ cm^{-1}$.

The number of clusters basically depends on the difference $\delta\omega_S$ - $\delta\omega_I$ between the intermode spacing and the linewidth of the resonances. If this difference is large compared to the width of cavity resonances, the axial modes in the PM band are distributed on a large number of clusters: then the DROPO is prone to cluster jumps. Conversely, if this difference is small, the axial modes in the PM band belong to a few large clusters: then the DROPO is prone to mode hops within the cluster of lowest Δk. [Padgett, 1994]

In our case, with a finesse far lower than in usual OPO cavities, the second regime prevails, with the presence of only one cluster in the PM band. Such spectral configuration results in two markedly different regimes:

1) The center of the cluster is near the center of PM spectrum: a mode pair has simultaneously $\Delta\omega \approx 0$ and $\Delta k \approx 0$, and its oscillation threshold is approximately given by Eq. 1.28. Tuning is accomplished by subsequent mode-hops.
2) The center of the cluster is on the edge of the gain band: the threshold is higher, as the better frequency-matched mode pair is not well phase matched. In this case, while tuning occurs mostly through mode hops, as the oscillating pair gets close to one edge of the gain band a shift to the opposite edge can occur, resulting in a large discontinuity of the emitted wavelengths.

* * *

One of the main points of concern for DROPOs is the wavelength stability. Compared to a

SROPO, the emitted wavelengths are more sensitive to fluctuations of: pump frequency, cavity length, and crystal temperature. [Falk, 1971; Smith, 1973; Nabors, 1990]

In Section 3.2.2 we have shown that the temperature of our waveguides depends on the coupled pump power, due to non negligible absorption at 1 μm. Hence, in the case of our integrated OPO, instabilities are supposed to occur with a prevailing thermal origin. Hereafter we estimate the requirements for stable operation on a single mode pair.

A mode hop requires a frequency shift equal to the FSR mismatch $\delta\omega_S - \delta\omega_I$, i.e. of the order of 100 MHz out of degeneracy.[50] Such a frequency shift of the signal and idler resonances corresponds to a temperature variation $\Delta T \approx 1$ mK, as calculated from the thermorefractive coefficients of signal and idler. We estimate the waveguide heating due to coupled pump $\Delta T/\Delta P_P \approx 0.02$ K/mW.[51] Hence, a temperature stabilization of $\Delta T \approx 1$ mK requires a coupled power stabilization $\Delta P_P \approx 50$ μW, i.e. $\Delta P_P/P_P \approx 10^{-3}$ for our typical working conditions.

At present, such a degree of stabilization on the coupled pump power is not attainable with our experimental setup, which allows $\Delta P_P/P_P \approx 10^{-2}$. Under these experimental conditions, the operation of the integrated GaAs/AlOx OPO is expected to be multimode.

4.3 Design and fabrication of the integrated mirrors

4.3.1 Dielectric mirrors

The solution that we have adopted to place our nonlinear waveguide in a DROPO resonator is the fabrication of integrated mirrors. Indeed, differently from $LiNbO_3$ waveguides, putting external dielectric mirrors in contact with a semiconductor waveguide is not convenient, for several reasons. The main issue is the lack of a suitable index-matching liquid to ensure the contact between the mirror and the facet. The refractive index of available index-matching liquids does not exceed n = 2.3. In addition, the facets of few μm wide semiconductor ridges are very fragile, making the contact with an external mirror hazardous.

The deposit of multilayer mirrors on semiconductor waveguide facets is a well-established technological process for the fabrication of commercial laser diodes. Both dielectric

[50] Hence, this is the frequency stability required for the pump wavelength, which is within the specifications of our Yb:YAG pump laser.

[51] The above $\Delta T/\Delta P_P$ coefficient has been estimated by comparing the experimental dependence of signal and idler wavelength on the coupled pump power with the temperature tuning curve.

or metallic multilayers can be deposited to make the facets of semiconductor lasers high- or low-reflecting. However, the deposit of such multilayers on GaAs/AlOx waveguides presents specific difficulties, related to the contraction of AlOx layers during the oxidation process. AlOx contraction in the waveguide plane causes an irregular surface at the waveguide facet. [Durand, 2003] Moreover, such shrinkage results in mechanical stress for the whole waveguide structure, which makes the adhesion of a coating more critical.

Due to difficult adhesion, the choice of the materials to deposit has been mainly dictated by the reduction of the total coating thickness. Note that, as the thickness of dielectric mirrors increases in general with the operation wavelength, a reflecting coating at 2 μm requires thicker layers than standard coatings for the NIR. We have singled out the combination of Si and low-index Al_2O_3 as the most convenient material system in this respect, although Si is not completely transparent at our pump wavelength.[52]

As mentioned before, the type of resonator we are dealing with is a doubly-resonant cavity with a double pump pass. Such scheme is based on two mirrors with high reflectivity at both signal and idler wavelength. In our case, this corresponds to a broad reflection band around degeneracy. Clearly, the input mirror (M_1) must be highly transparent at pump wavelength. This allows to increase the coupled pump power and, above all, to prevent a resonant behavior at λ_P, which would affect the OPO stability.[53] Finally, the reflectivity of the output mirror (M_2) at λ_P must be as close as possible to 100%, so as to reduce the oscillation threshold, according to Eq. 4.5. In order to obtain a $R_2 \geq 97\%$ around 2 μm, we have set to six the number of layers to deposit. Rather than a simple $\lambda/4$ periodic multilayer, we have designed two aperiodic structures, to optimize the performances of the coatings at λ_P. [Zheng, 1987]

The mirrors have been designed with the 1D transfer matrix method, [Yeh, 1988] using standard values for Si index. [Adachi, 1988] We have optimized the thickness of individual layers with an algorithm for the minimization of a merit function. Such function takes into

[52] The absorption of a 1 μm thick Si layer is about 4% in the 1.03-1.06 μm range. On the other hand, due to its high refractive index ($n \approx 3.5$ in the NIR) the required thickness of Si layers is lower than for alternative materials, like TiO_2 ($n \approx 2.5$).

[53] A non-vanishing reflectivity of the input mirror at λ_P would result in a triply-resonant cavity. Stable operation of triply-resonant OPO, due to the discretization of frequencies at λ_P, λ_S, and λ_I, is far more critical than for DROPO. [Richy, 1995]

account the reflectivity or the transmission of the multilayer at the wavelengths of interest, as well as the total thickness of structure.

The final structure of M_1 and M_2 is reported in tables 4.1 and 4.2

M_1	
Material	**Thickness (nm)**
Substrate	
Al_2O_3	342
Si	185
Al_2O_3	369
Si	167
Al_2O_3	227
Si	139
Air	

Table 4.1 Structure of the mirror M1.

M_2	
Material	**Thickness (nm)**
Substrate	
Al_2O_3	235
Si	189
Al_2O_3	228
Si	190
Al_2O_3	228
Si	189
Air	

Table 4.2 Structure of the mirror M2.

The corresponding reflection spectra are shown in Figure 4.9: the broad high-reflectivity band around 2 μm is very similar to that of a λ/4 Bragg mirror. However, thanks to our optimization procedure, both the expected transmission of M_1 and the expected reflectivity of M_2 at λ_P are higher than 95%. The overall thickness is kept below 1.5 μm for both coatings.

The dielectric Si/Al_2O_3 multilayers have been deposited at Al-Technologies (Darmstadt, Germany) a factory specialized in facet coating for semiconductor lasers. In order to calibrate

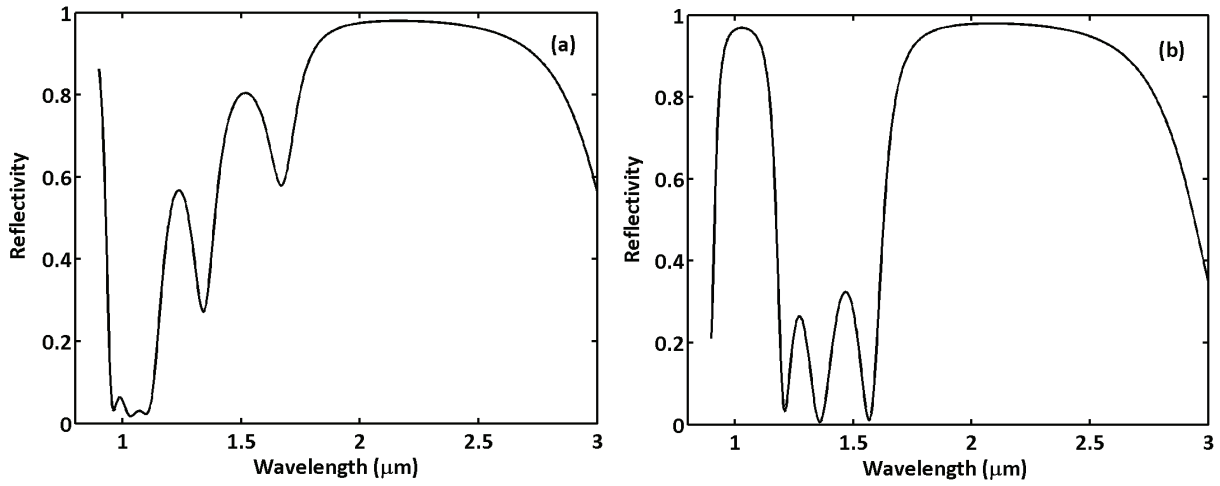

Figure 4.9 Calculated reflection spectra for the mirrors M1 (a) and M2 (b).

the deposition process, a test multilayer with the structure of M_1 was previously deposited on a Si substrate. Figure 4.10 shows the reflectivity spectrum at normal incidence of this sample, measured by Fourier-transform IR (FTIR) spectroscopy. In good agreement with the calculated spectra, $R_1 \geq 95\%$ all over the interval between 1.9 and 2.8 μm, with a maximum $R_1 \approx 98\%$, while at pump wavelength $R_1 \approx 15\%$. However, the latter value has to be considered as an upper bound to the actual one, since at 1 μm the spectrometer is at the edge of its spectral range of operation.[54]

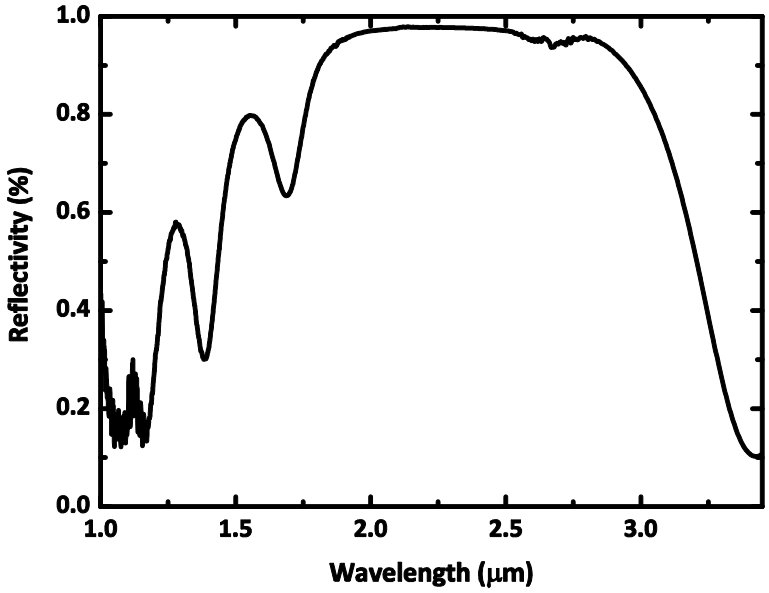

Figure 4.10 FTIR reflectivity spectrum of the mirror M1 deposited on a Si substrate.

The same type of multilayers have then been deposited on the facets of three bars of waveguides. A detail of a coated facet observed at SEM is shown in Figure 4.11. Regretfully, the coated samples have not provided satisfying results. While for $R_1 = 5\%$, $R_2 = 95\%$ and $\alpha = 0.5$ cm^{-1} the pump throughput vs. wavelength is expected to oscillate between 3% and 6%, the experimental value was generally of the order of 0.1%. Since samples had been tested before being coated, we can ascribe the low transmission to losses at the coated facets. In some cases a weak PF signal could be detected anyway, but any attempt to further increase the injected pump resulted in coating damaging. Figure 4.12 shows a SEM image of the input facet with the dielectric coating broken and detached. We attribute such damage to the heat generated by

[54] The above spectrum is obtained as the ratio of the power reflected by M1 and that reflected by a reference Ag mirror. The source employed for both measurements is a blackbody radiator, whose emitted power considerably decreases for wavelengths close to 1 μm. This results in a poor SNR for the detected reflection of both M1 and Ag mirrors, and thus in an overestimated R_1/R_{Ag} value around this wavelength.

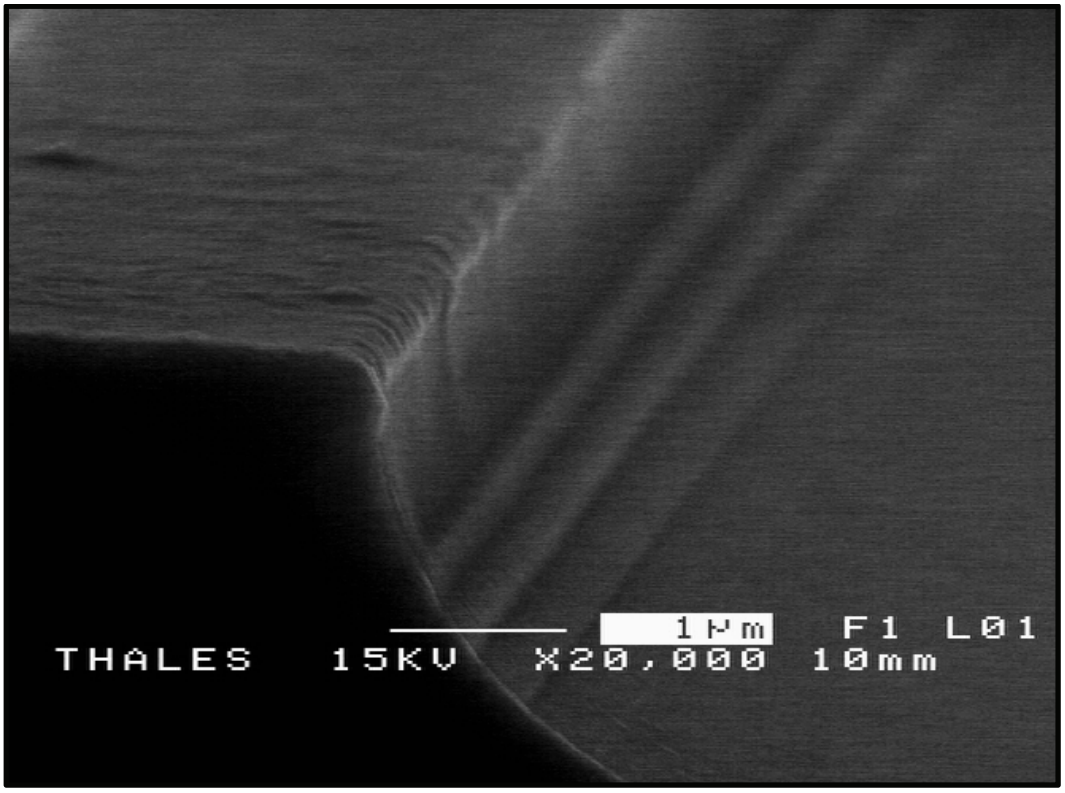

Figure 4.11 SEM detail of the mirror M1.

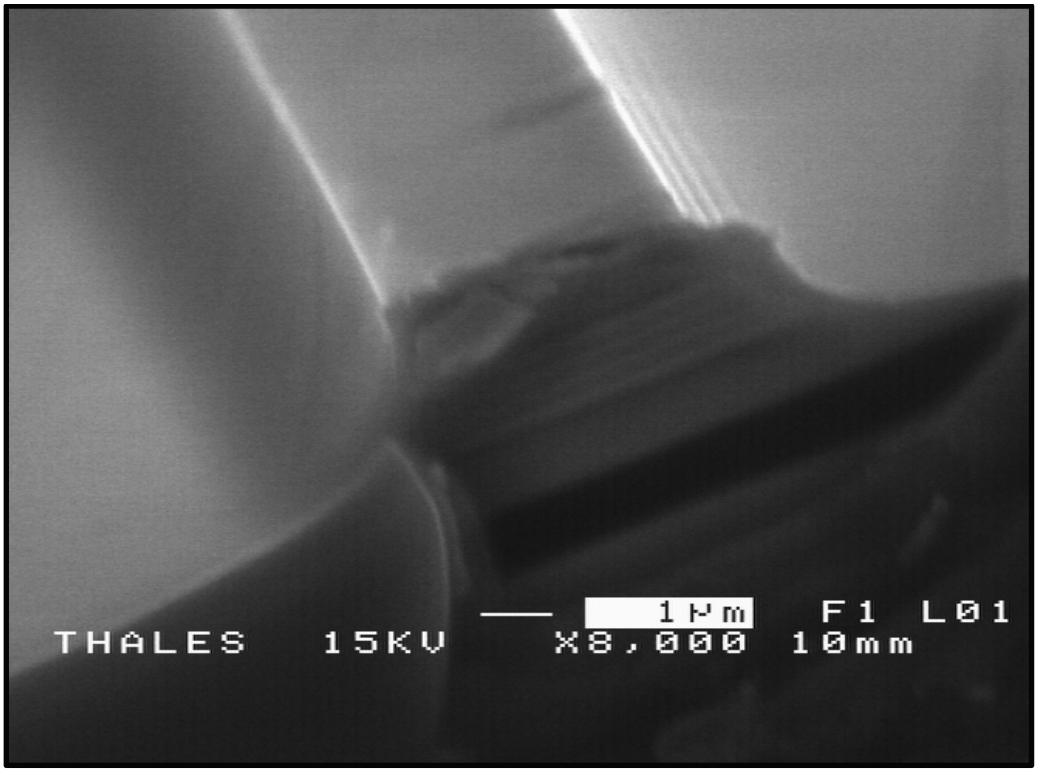

Figure 4.12 SEM image of an input facet with damaged dielectric coating. Such result is ascribed to the heat produced by the intense focused pump on the input facet, possibly due to absorption in the Si layers of the coating.

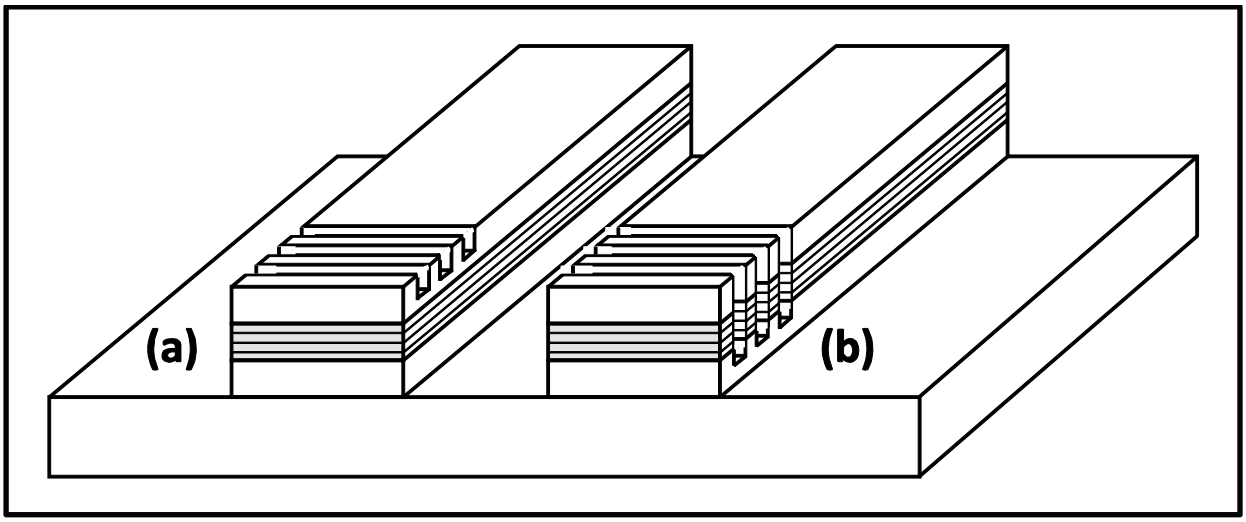

Figure 4.13 Shallow-etched (a) and deep-etched (b) distributed Bragg reflectors on GaAs/AlOx waveguides.

the 200 mW intense (≈ 10 MW/cm^2) pump beam focused onto the input facet. According to Al-technologies such type of coatings is successfully employed on laser diodes at 1.55 μm emitting up to 100 mW.[55] Hence, the detachment of the mirrors is supposed to arise from elements specific to our waveguides and experimental conditions, namely absorption in Si layers or the poor adhesion of the coating to the facet.

4.4 Chapter conclusion

In this chapter we have discussed the fabrication of an integrated OPO based on our GaAs/AlOx waveguides. Firstly, we have reviewed the state of the art of integrated OPOs, so far all based on $LiNbO_3$ waveguides. Secondly, we have briefly detailed the main features of most common OPO configurations: threshold, stability and tuning. Such features have been theoretically investigated for a GaAs/AlOx DROPO. Thirdly, we have described the design and fabrication of our first integrated dielectric mirrors

The problems emerged from the deposition of dielectric coatings have induced us to start working on alternative solutions for the insertion of our waveguides in a resonant cavity. In particular we are at present investigating the possibility of fabricating distributed planar reflectors. Two approaches are under study at present within the DON group of the MPQ

[55] Corresponding to an intracavity power = 100 mW/(1-R).

laboratory, in collaboration with the LPN laboratory (Marcoussis). Both are based on e-beam lithography and reactive ion etching:

1) the fabrication of shallow-etched Bragg mirrors, after the example of DBR laser diodes. In this scheme, reflection of the guided modes is achieved through a weak periodic perturbation of the effective index along the propagation direction. As shown in Figure 4.13a, in our parametric generator the perturbation could be introduced by partially etching the waveguide upper cladding. Such modification of the guiding structure has a limited influence on the profiles and the effective indices of the guided modes, with a maximum index perturbation $\Delta n \approx 5\times10^{-3}$ obtained with the complete cladding removal. As a consequence, the number of repetitions necessary to achieve R > 90% is of the order of 1000, which corresponds to a propagation length of few hundreds of microns. For this reason it is crucial to keep the losses introduced by this etching process much lower than the present level (≈ 0.5 cm^{-1}), such to avoid an increase of the oscillation threshold.
2) The fabrication of deep-etched Bragg mirrors, with a technological process analogous to those employed for photonic crystal waveguides. [Krauss, 1996] In this approach, modal reflectivity is obtained with a strong periodic perturbation, following from the periodic complete removal of the guiding film along the propagation direction, as shown in Figure 4.13b. Thanks to the strong index contrast n_{eff}/air only a few repetitions are sufficient to reach a reflectivity higher than 90%. Whereas in this case additional losses are limited to a much shorter propagation distance, scattering is expected to be locally much more intense, in particular at the interfaces between the guiding core and air along the waveguide axis.

5 Second-order nonlinear processes as characterization tools

Tunability, nonlinear efficiency and optical losses are the most relevant parameters for an integrated parametric generator. In a nonlinear waveguide, the tunability is related to the effective indices of the interacting modes, while the conversion efficiency is determined by the nonlinear overlap integral. Propagation losses stem from scattering at the waveguide interfaces or from bulk absorption.

In this Chapter we detail a few techniques that we have developed to investigate such features. Such techniques are based on a common principle: the use of a $\chi^{(2)}$ process as a characterization tool. Section 5.1 describes the exploitation of PF to measure the optical losses of the nonlinear medium on a broad wavelength interval. This technique, suitable for both bulk and integrated devices, allows one to measure propagation losses in spectral ranges not accessible with available laser sources and detectors.

The last two Sections address two applications of counterpropagating interactions: Section 5.2, the investigation of the PM condition in nonlinear waveguides through SESHG and surface-emitted SFG (SESFG); Section 5.3, the experimental study of the conversion efficiency of a counterpropating parametric generator through SESHG and backward DFG (BDFG).

5.1 Parametric fluorescence for MIR spectroscopy

As discussed previously, optical losses have a strong impact on $\chi^{(2)}$ nonlinear interactions: reduction of the conversion efficiency and increase of the phase-matching bandwidth (see Figure 5.1). These effects can be exploited to quantitatively estimate the attenuation coefficient of a lossy nonlinear medium. Such exploitation is especially useful when the direct transmission measurement, which is in general the most straightforward technique, cannot be adopted in practice.

In this section we propose a novel technique to measure the attenuation coefficient of a nonlinear medium in spectral regions where transmission measurements are made difficult by the lack of sources and detectors. Our approach relies on parametric down-conversion: we exploit the wide tuning range of the generated signal and idler to investigate the losses of the nonlinear medium in the same region. Firstly, this configuration allows to explore a wide spectrum not attained by the pump source (note that the same principle can be applied with a

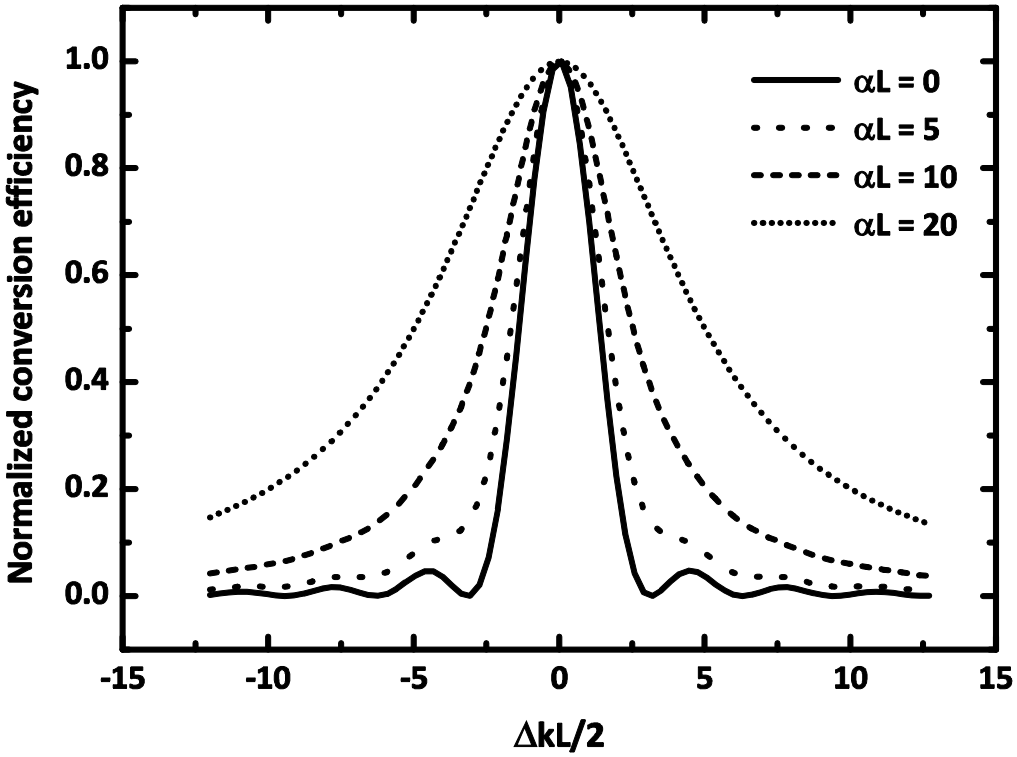

Figure 5.1 Phase-matching broadening due to linear losses: DFG detuning curve for three different values of idler losses.

frequency doubling experience, by investigating the generated SH to measure the attenuation at 2ω). Secondly, our approach allows to get round the lack of a detector at the wavelength concerned. Indeed, as attenuation at λ_S or at λ_I identically affects both generated fields, all the spectrum covered by the idler can be studied by detecting only the signal field, and vice versa. In practice, this spectroscopic technique can find application, with a 1 μm pump, to measure the optical losses of either nonlinear crystals or nonlinear waveguides in the MIR, beyond 2 μm.

5.1.1 MIR absorption spectrum of GaAs form-birefringent waveguides

In the NIR spectrum (<2 μm), the presence of losses in GaAs/AlOx waveguides lies mainly on scattering at GaAs/AlOx interfaces, with attenuation constants in the dB/cm range. Besides Fabry-Perot measurements in the telecom range, [De Rossi, 2005a] this was demonstrated by surface scattering measurements between 1.3 μm and 2 μm. [Rao, 2002] However, very few data can be found in the longer wavelength range, from 2 to 4 μm, where Rayleigh scattering at the ridge sidewalls or at GaAs/AlOx interfaces is expected to decrease. Such information is potentially interesting for applications of our integrated parametric source in the MIR range,

which e.g. contains important absorption lines for gas sensing, like CO_2 (4230 nm) and CH_4 (3260 nm). While GaAs optical properties in the MIR have been widely studied in the past, [Palik, 1985] very few data are available for AlOx. The transmission of 1 μm thick superficial AlAs layer was studied one decade ago in the 2-12 μm range by FTIR spectroscopy, before and after oxidation. [Fiore, 1997c] Qualitative transmission measurements in the same range were then carried out on planar oxidized AlGaAs waveguides by FTIR guided-wave spectroscopy. [Bravetti 1998] In these works AlOx transparency in the IR was found to extend up to 10 μm, limited by an absorption peak due to Al-O vibrations.[56] Moreover, a resonance around 3 μm, ascribed to oxidation residuals, was reported.

In Section 3.1.3 we have shown that PF tuning range of our waveguides is included between 1.69 and 2.75 μm. In order to verify whether such range is actually limited by the above absorption peak, we have performed a series of spectral measurements in this spectral range. The acquisition of such spectra allowed us to develop our loss measurement technique and to quantitatively characterize AlOx absorption around 3 μm.

We remind that the detection range of our spectrometer is included between 1.3 μm and 2.4 μm, preventing idler measurement. Accordingly, we monitored the idler losses beyond 2 μm by investigating the features of the accessible co-generated signal, exploiting it as a MIR probe.

The PF experiments have been performed on a sample A, with the experimental setup described in Section 3.1.1. The acquired signal spectra off degeneracy are reported in Figure 5.2, and the resulting tuning curve in Figure 5.3. As λ_P is tuned down from degeneracy, the signal bandwidth is initially in good agreement with the calculated values for the lossless case (Figure 5.4a). Conversely, in the 1.4-1.6 μm region, our experimental spectra rapidly broadens (Figure 5.4b), with a considerably weaker peak power. Finally, for λ_P < 1.4 μm the signal power increases and the linewidth starts to narrow again.

In the presence of optical losses, the conversion efficiency decreases, while the shape of

[56] Note that AlOx transparency range is much more extended in the IR with respect to other oxides commonly used in nonlinear optics. The transparency region of $LiNbO_3$, KTP and BBO extends only up to 5 μm, 4.5 μm and 3.5 μm, respectively, limiting their applications for frequency generation in the MIR. Indeed, since the bond vibration frequency of two atoms depends on their reduced mass, the Al-O resonant energy is further in the IR compared to the other oxides just mentioned, composed of lighter atoms. Thanks to this feature, the employment of AlOx layers only partially limits the GaAs IR wide transparency region, extended up to 17 μm.

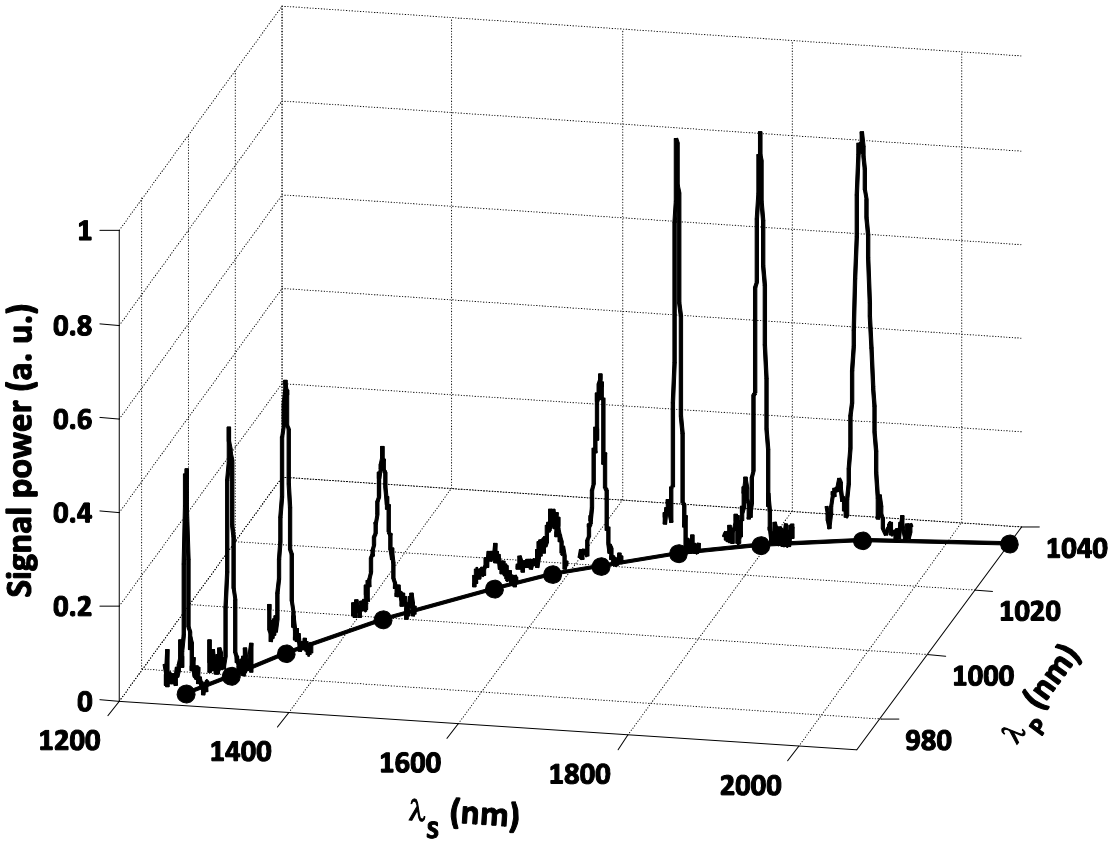

Figure 5.2 Off-degeneracy PF spectra vs. signal wavelength. In the lossless case, getting far from degeneracy, both the amplitude and the width of the peaks are expected to gradually decrease. The abrupt evolution found here in the 1.4-1.6 μm range is the signature of a strong attenuation band for one of the three interacting fields.

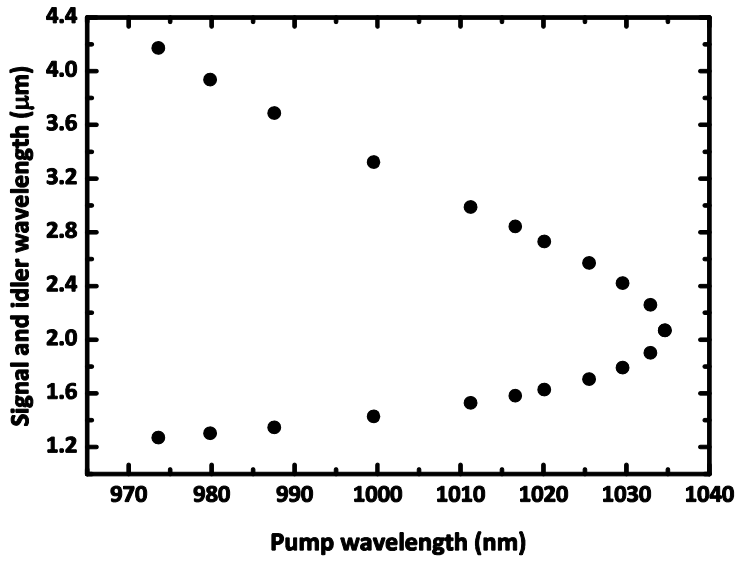

Figure 5.3 Experimental tuning curve, showing signal and idler wavelengths versus pump wavelength. Signal and idler data points in the 1200-2400 nm range come from direct measurement of the emitted spectrum. Idler data points beyond 2400 nm have been deduced by energy conservation.

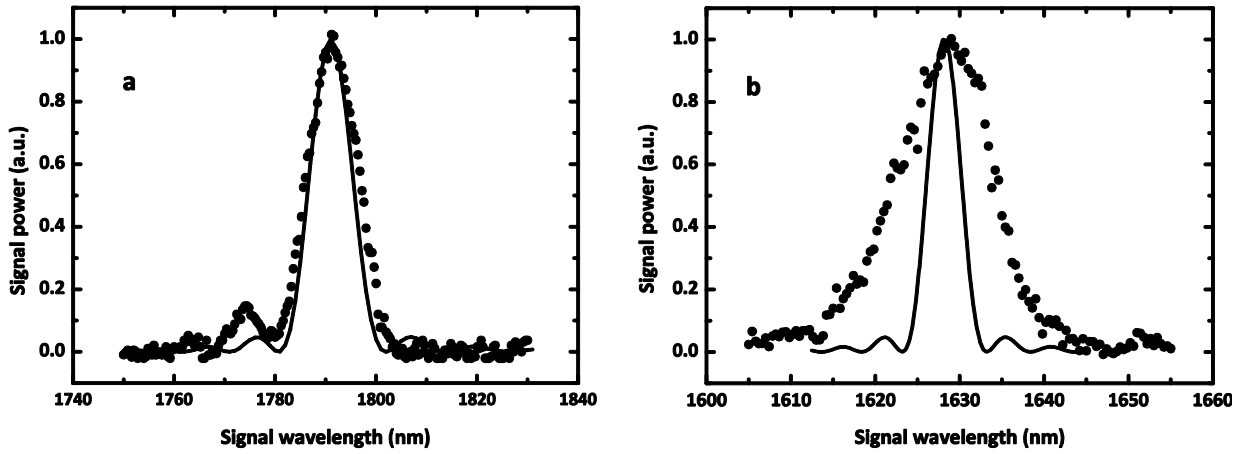

Figure 5.4 Experimental (points) and lossless calculated (solid line) signal spectra, outside (a) and inside (b) AlOx absorption range for the idler.

the phase-matching spectrum

$$\psi(\Delta kL, \alpha_{P,S,I}) = \frac{\sin^2(\Delta kL/2) + \sinh^2\left[(\alpha_P + \alpha_S - \alpha_I)L/4\right]}{(\Delta kL/2)^2 + \left[(\alpha_P + \alpha_S - \alpha_I)L/4\right]^2} \tag{5.1}$$

broadens and changes from $sinc^2$ to lorentzian (Figure 5.1), depending on a combination of the attenuation coefficients of pump, signal and idler modes $\alpha_{P,S,I}$. [Sutherland, 1996]

According to Eq. 5.1, the anomalous behavior of Figure 5.2 could arise from the presence of an attenuation band for any of the three interacting modes. However, from pump transmission measurements we infer $\alpha_P \approx 1$ cm^{-1}, whereas the value $\alpha_S = 0.45$ cm^{-1} has been precisely measured in the 1.5-1.6 μm range. Since Eq. 5.1 predicts that attenuation coefficients of the order of a few cm^{-1} only result in a relative broadening around 1% (i.e. much smaller than the stretching of our spectra in the 1.4-1.6 μm region) we can conclude that α_P, $\alpha_S << \alpha_I$. This confirms that the tunability of our parametric generator is limited by a strong attenuation experienced by the idler in the 2.5-4.2 μm region. Because of the expected decrease of scattering losses with wavelength, and because we know from complex eigenvalue calculations that the idler mode becomes leaky only for $\lambda_I > 4$ μm, we can safely ascribe such attenuation to absorption in the AlOx layers.

The idler modal attenuation $\alpha_I(\lambda)$ has been inferred by fitting the normalized experimental spectra with Eq. 5.1. Note that $\alpha_I(\lambda)$ could alternatively be evaluated through an

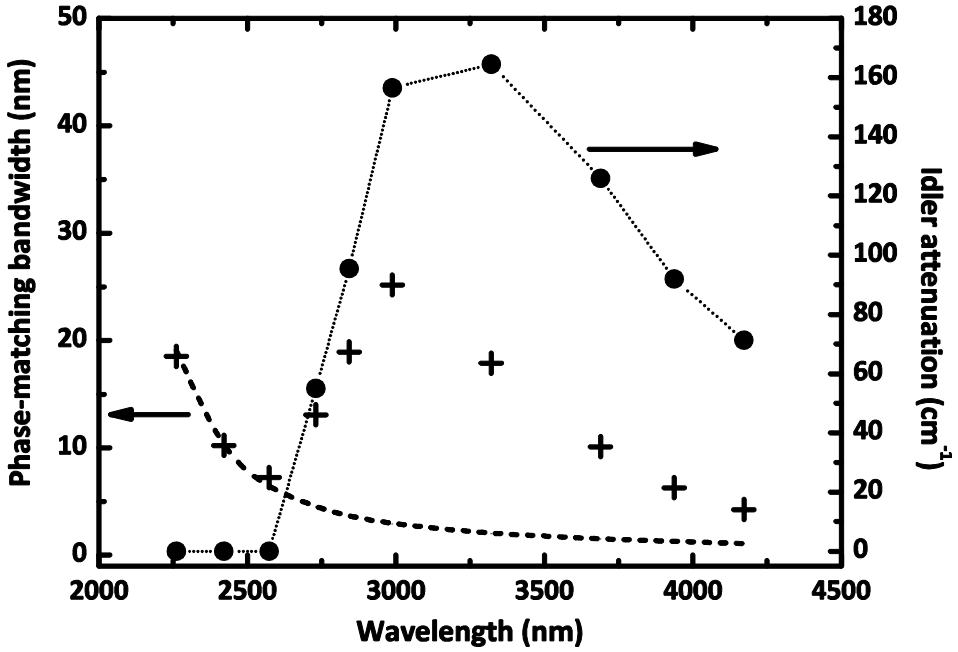

Figure 5.5 On the left axis: signal bandwidth vs. idler wavelength: experimental values (crosses) and calculated curve in the lossless case (dashed line). On the right axes: experimental idler attenuation (dots; here the dotted line is a mere guide to the eyes).

estimation of the peak PF efficiency [Sutherland, 1996]

$$\eta' = \eta \exp(-\alpha_I L) \sinh^2(\alpha_I L/4) / (\alpha_I L/4)^2 \tag{5.2}$$

with η the lossless efficiency at phase matching. However, the accuracy of such method would be affected by the uncertainties, over a wide wavelength range, of: detector calibration, optics transmission, pump input coupling, and waveguide nonlinear overlap integral.

Figure 5.5 (left axis) shows the experimental signal phase-matching bandwidths corresponding to Fig. 5.2, along with their calculated counterparts in the lossless case, versus idler wavelength. On the right axis, it also reports the attenuation coefficient of the idler mode, inferred by fitting these experimental data with Eq. 5.1: an attenuation band is apparent, with a peak of α_I = 164 cm^{-1} at about 3.3 μm. The absorption coefficient α_{AlOx} can be deduced by scaling the idler attenuation with its confinement factor in the AlOx layers

$$\Gamma \equiv \int_{AlOx} |\phi_I|^2 dxdy \Big/ \int_{\infty} |\phi_I|^2 dxdy \tag{5.3}$$

According to our simulations, 9.5% < Γ < 10.9% for 2.5 μm < λ_I < 4.2 μm. Because of this weak wavelength dependence of Γ, α_{AlOx} has roughly the same spectral shape as the idler

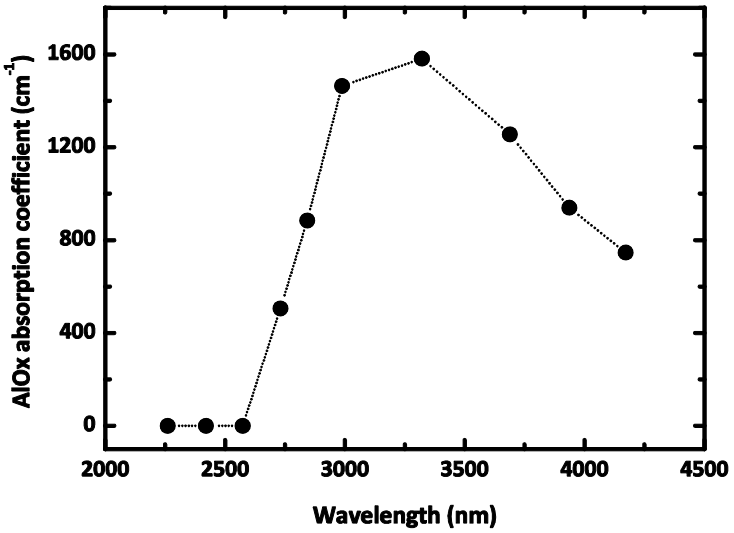

Figure 5.6 Experimental AlOx absorption coefficient vs. wavelength

attenuation. This can be appreciated in Figure 5.6, where α_{AlOx} is shown to peak at (1600±100) cm^{-1}.

The shape of the absorption-spectrum of Figure 5.6, is similar to those of Figure 5.7, from Ref. [Bravetti, 1998] (a) and from Ref. [Fiore, 1997c] (b), with an abrupt front at about 2.7 μm and a more gradual one between 3 and 4 μm. While from the former we cannot quantitatively infer a value of α_{AlOx}, from latter we deduce a peak $\alpha_{AlOx} \approx 1300\ cm^{-1}$ at $\lambda \approx 3$ μm, in qualitative agreement with our result. Such consistence confirms the common origin of the

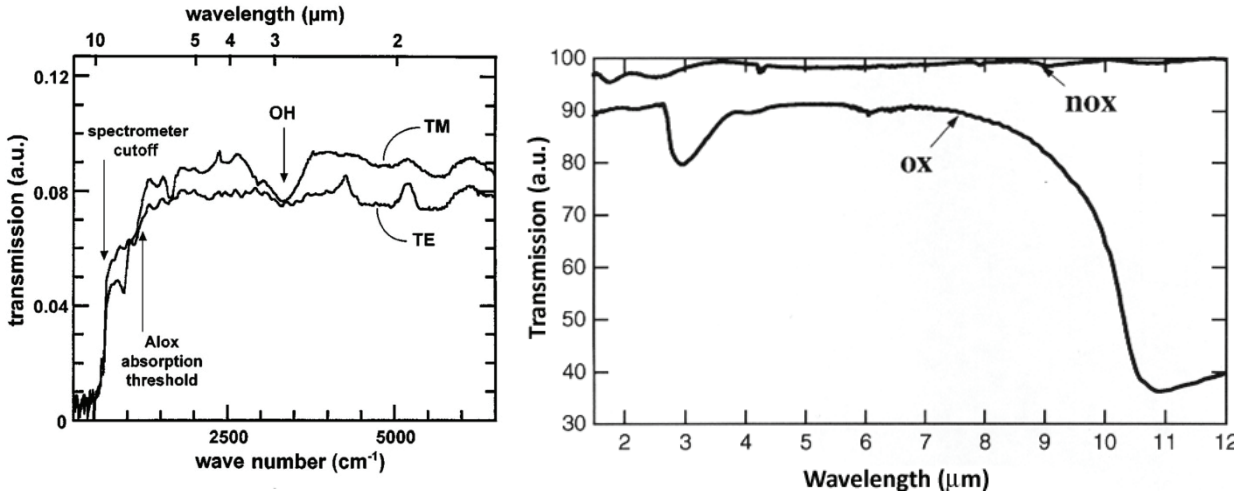

Figure 5.7 Two different studies of AlOx transparency in the MIR: a) FTIR transmission measurements in a 4-mm long, 100-μm wide GaAs/AlOx waveguide for TE and TM polarization (from Ref. [Bravetti, 1998]) b) FTIR transmission measurements at the Brewster angle of a 1 μm thick AlAs layer on a GaAs substrate, before (nox) and after oxidation (ox) (from Ref. [Fiore, 1997c]).

absorption peaks measured: such broad resonance, present in several oxides, is attributed to the presence of O-H ions, which are reported defects in AlOx layers due to the wet-oxidation process. [Sugg, 1991] As this detrimental presence is expected to be removed with a thermal annealing, [Bravetti, 1998; Fiore, 1997c] our nonlinear technique of absorption measurement proves a convenient support to single out the most appropriate annealing scheme.

5.2 SESHG for modal birefringence measurements

Modal birefringence is of paramount importance for several kinds of integrated devices. This is the case of frequency converters based on birefringent PM, where birefringence is directly responsible for dispersion compensation. In AlGaAs waveguides, where form birefringence is affected by growth and processing uncertainties, the measurement of modal birefringence represents a key issue.

For those applications that do not require the absolute value of the effective indices, the direct investigation of modal birefringence can prove an advantageous solution. This is the case of birefringence measurements through SESHG[57] in GaAs waveguides. [Vakhshoori, 1988] In such devices effective index measurements are complex, as they require the fabrication of an integrated grating. Conversely, for birefringence measurements through SESHG, a simple experimental setup based on a low-power pump source suffices, thanks to the high nonlinearity of GaAs. SESHG is e.g. the solution of choice to measure the birefringence of GaAs/AlOx waveguides. [Fiore, 1997b; Leo, 2001]

In Section 1.2.6 we have shown that two counterpropating modes in a $\chi^{(2)}$ nonlinear waveguide can generate a second-harmonic field in a mode radiating from the upper surface. According to $\chi^{(2)}$ selection rules, in GaAs waveguides such interaction is allowed only for orthogonally-polarized pump modes. The corresponding 2ω field is TE polarized and is emitted according to an out-of-plane angle $\theta = \arcsin(2\pi(n_{TE}-n_{TM})/\lambda_{\omega})$.

As both guided modes propagate forward and backward, due to Fresnel reflection at waveguide facets, two second-harmonic radiation modes are excited symmetrically with emission angles $\pm\theta$. The period of the corresponding interference pattern, $\Lambda = \lambda_{\omega}/[2(n_{TE}-n_{TM})]$, can be directly measured by near-field (NF) imaging of the waveguide surface. Alternatively, the

[57] See Section 1.2.6.

birefringence can be measured by far-field (FF) imaging with a lens of focal length f: in this case, the acquired image is the Fourier transform of the 2ω field, with the two emitted waves focused on two lines separated by $f/(n_{TE}-n_{TM})$.

5.2.1 Application to counter-propagating parametric devices

In this Section I describe the results obtained by employing SESHG to measure the birefringence of a waveguide designed for counterpropagating PF. This geometry, conceived for the generation of entangled photons for quantum optics experiments [Bouwmeester, 2000] by SPDC, was firstly proposed by De Rossi and Berger, [De Rossi, 2002] and demonstrated in the MPQ laboratory. [Lanco, 2006a]

The operation scheme of the device is shown in Figure 5.8: a pump beam, impinging on top of the guiding structure at an angle θ, parametrically generates two counterpropagating, orthogonally polarized signal/idler guided modes. Momentum conservation is obtained as already described in Section 1.2.6 for SESHG; in this case, based on the wave-vector conservation in the waveguide plane, two processes are simultaneously phase matched

$$\begin{cases} \omega_P = \omega_S + \omega_I \\ \omega_P \sin\theta = \omega_S n_{TE}(\omega_S) - \omega_I n_{TM}(\omega_I) \end{cases}$$
$$\begin{cases} \omega_P = \omega_S + \omega_I \\ \omega_P \sin\theta = \omega_S n_{TM}(\omega_S) - \omega_I n_{TE}(\omega_I) \end{cases} \qquad (5.4)$$

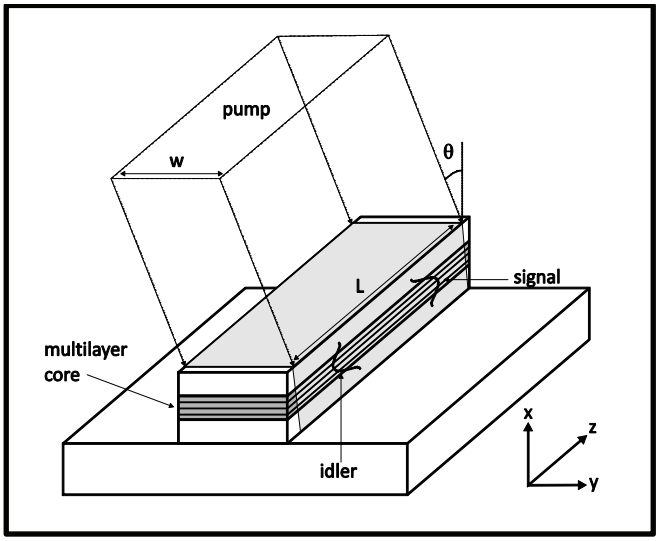

Figure 5.8 Schematic of the counterpropagating entangled photon source. We have pointed out: the pump incidence angle θ, the interaction length L, and the width of the pump beam, considered equal to that of the waveguide.

In the former (interaction 1), the photon copropagating with the z component of the pump beam (signal) is TE polarized, while the photon counterpropating (idler) is TM polarized; in the latter (interaction 2) the polarizations are inverted. Two similar vertical structures have been designed for this interaction: structure "C" [GaAs (100)/$Al_{0.94}Ga_{0.06}As$ (1081 nm)/$Al_{0.25}Ga_{0.75}As$ (110 nm)/4 × [AlAs (128 nm)/ $Al_{0.25}Ga_{0.75}As$ (110 nm)]/$Al_{0.94}Ga_{0.06}As$ (1081 nm)/air], and structure "D" [GaAs (100)/$Al_{0.94}Ga_{0.06}As$ (1081 nm)/$Al_{0.25}Ga_{0.75}As$ (110 nm)/4 × [$Al_{0.80}Ga_{0.20}As$ (124 nm)/$Al_{0.25}Ga_{0.75}As$ (110 nm)]/$Al_{0.94}Ga_{0.06}As$ (1081 nm)/air]. Both multilayers have a guiding core alternating $\lambda/2$ layers with different Al content, resulting in (+/0) QPM propagation in the vertical direction.[58]

Figure 5.9 shows the tuning curves of structure C for the two interactions versus the incidence angle θ. For increasing θ, signal and idler photon energies are progressively split, as the pump wave vector horizontal projection is increased. Due to slight form birefringence, degeneracy occurs for $\theta = \pm 0.57°$ ($\theta = \pm 0.38°$ in structure D) rather than at orthogonal incidence.

The key role played by modal birefringence with respect to these tuning curves points out the importance of an experimental characterization. Especially in this structure, designed and optimized for counterpropagating PM, performing this measurement by means of an SESHG experiment is an obvious choice.

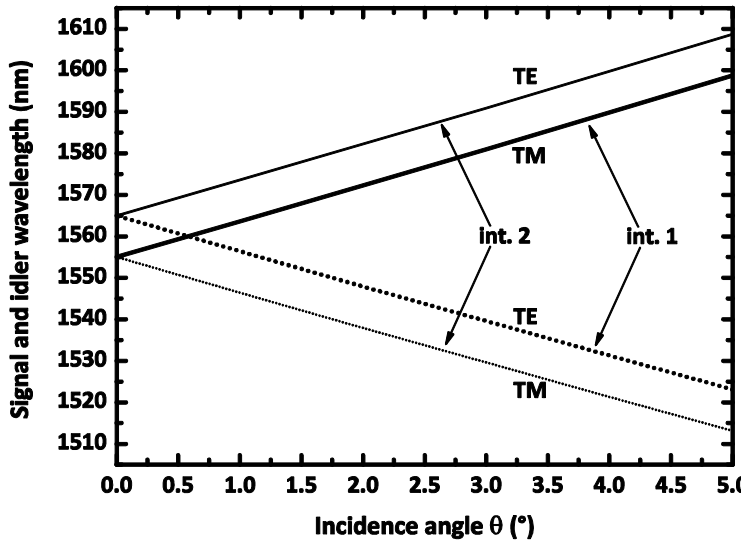

Figure 5.9 Calculated tuning curves for structure C for a pump wavelength of 780 nm. Thick lines: interaction 1; thin lines: interaction 2. The dotted lines represent the photons copropagating with the z component of the pump beam, while the solid lines represent the counterpropagating ones.

[58] $d_{14}(AlAs)/d_{14}(Al_{0.25}Ga_{0.75}As) \approx 3.8$, $d_{14}(Al_{0.8}Ga_{0.2}As)/d_{14}(Al_{0.25}Ga_{0.75}As) \approx 2.6$.

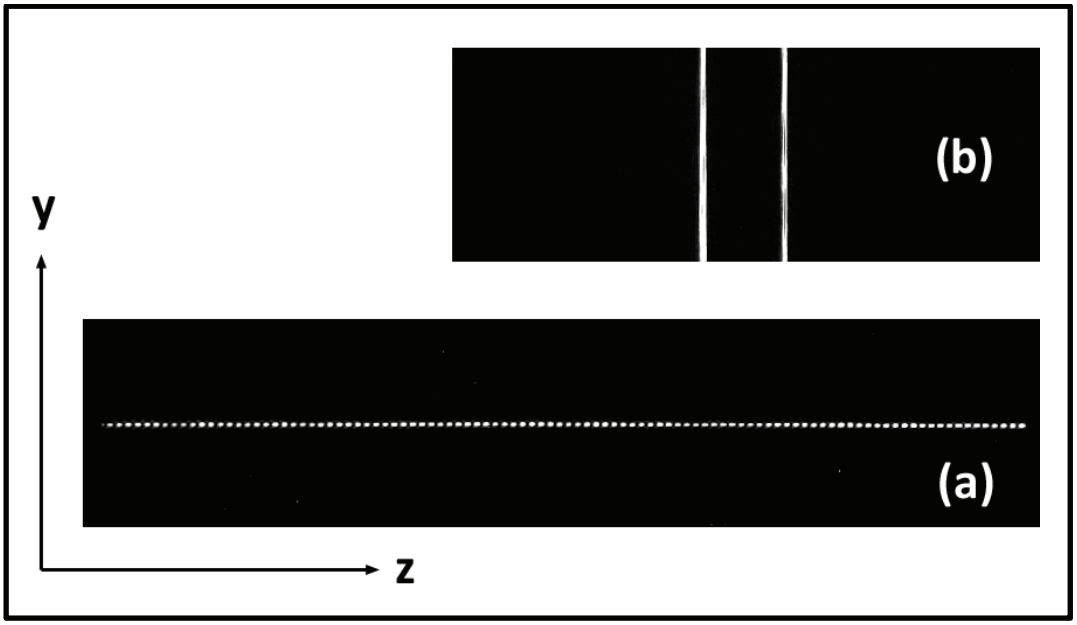

Figure 5.10 NF (a) and FF (b) images of SESHG at 775 nm, emitted from structure C.

The experiment is carried out with a 10 mW CW DFB laser diode oscillating at λ = 1.55 μm. The input beam, linearly polarized at 45° relative to substrate plane, is focused onto the input facet of the L = 4 mm, w = 6 μm ridge waveguide with a standard 40X microscope objective. The waveguide output is collimated with a second 40X objective. Coupling is assisted by an IR vidicon camera and a Ge photodiode that measures the throughput. SESHG is acquired with an optical system mounted above the waveguide, perpendicularly to the plane of that. This is composed by a high-resolution CCD camera (4.5 mm x 4.5 mm, 1024 x 1360 pixel) and, either a Leica MZ12 microscope for NF imaging or a lens with f = 25.4 mm for FF imaging. Figure 5.10 shows the pictures acquired with both optical systems. By counting the number of fringes we infer a modal birefringence ΔN = 0.0181 ± 0.0004, corresponding to an emission angle θ = 0.52° ± 0.01°, in good agreement with the expected value.

Effective index measurements by grating assisted input coupling [Martin, 1995; Leo, 2001] have been successively performed on the planar counterpart of the same sample, to further investigate the characteristics of the epitaxial structure. This gave us the chance to validate our experimental ΔN. The experimental effective indices of the fundamental modes are n_{TE0} = 3.0363±8·10^{-4} and n_{TM0} = 3.0189±8·10^{-4} at 1.55 μm, in perfect agreement with the result of the SESHG measurement. Birefringence experimental and calculated values are summarized in table 5.1

	SESHG	Effective index	Model
$n_{TE0} - n_{TM0}$	$0.0181 \pm 4 \cdot 10^{-4}$	$0.017 \pm 2 \cdot 10^{-3}$	$0.020 \pm 4 \cdot 10^{-3}$

Table 5.1 Summary of experimental and theoretical birefringence values for structure C.

We stress that the SESHG measurement ensures a better accuracy than that of effective index measurements.

5.2.2 SESFG generalization

Encouraged by the reliable results obtained with this method in order to determine the angle of degeneracy, we have extended it to experimentally determine the complete tuning curve versus θ, shown in Figure 5.9. To this end, a non-degenerate surface-emitted SFG interaction is necessary. This experiment, the inverse to non-degenerate PF, requires two pairs of counterpropagating modes at two different wavelengths λ_{TE} and λ_{TM}. Accordingly, two radiation modes are nonlinearly generated at $\lambda = (1/\lambda_{TE} + 1/\lambda_{TM})^{-1}$, at symmetric angles $\pm\,\theta$, with

$$\theta = \arcsin\left(\frac{2\pi n_{TM}(\lambda_{TM})}{\lambda_{TM}} - \frac{2\pi n_{TE}(\lambda_{TE})}{\lambda_{TE}}\right) \tag{5.5}$$

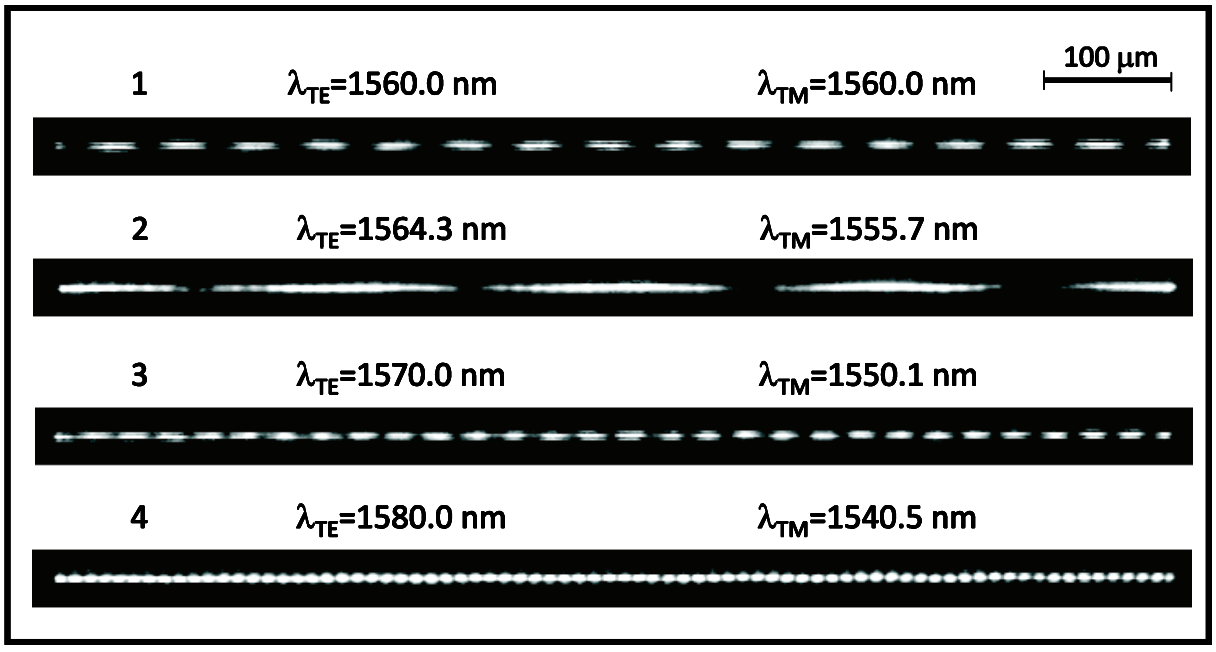

Figure 5.11 NF images of the surface-emitted SFG at $\lambda_P = (1/\lambda_{TE} + 1/\lambda_{TM})^{-1} = 780$ nm from structure D, for different values of λ_{TE} and λ_{TM}.

As for SESHG, a periodic interference appears on top of the waveguide surface. For a given pump wavelength λ_p, the reconstruction of the down-conversion tuning curve is achieved by varying λ_{TE} and λ_{TM} according to frequency conservation, $(1/\lambda_{TE} + 1/\lambda_{TM})^{-1} = \lambda_p$. Further tuning curves, for different λ_p values, can be traced by just changing the relation between λ_{TE} and λ_{TM}.

We stress that the period of the SFG pattern decreases very rapidly as the emission angle increases (Λ is infinite for θ = 0° and decreases down to about 2 μm for θ = 10°), preventing the count of the sinusoidal fringes for high θ. Nevertheless, as our interest is focused on the PM condition near degeneracy, we have opted for a birefringence measurement by NF imaging, because of its higher accuracy. [Leo, 2001]

The experimental setup is based on two external-cavity tunable laser diodes in the telecom range. The two beams, one TE and the other TM polarized, are combined and collinearly aligned by means of a 50% beam-splitter. The resulting beam is then end-fire coupled in the L = 0.87 mm, w = 4 μm ridge waveguide, with the remainder of the setup identical to SESHG case.

The tuning curve has been studied for a pump wavelength λ_P = 780 nm, in a D sample. Some of the fringe patterns acquired are shown in Figure 5.11: as expected, the period Λ decreases very rapidly as the difference between the propagation constants of the two modes grows. The first, top most, acquisition has been obtained at degeneracy, with $\lambda_{TE} = \lambda_{TM}$ =

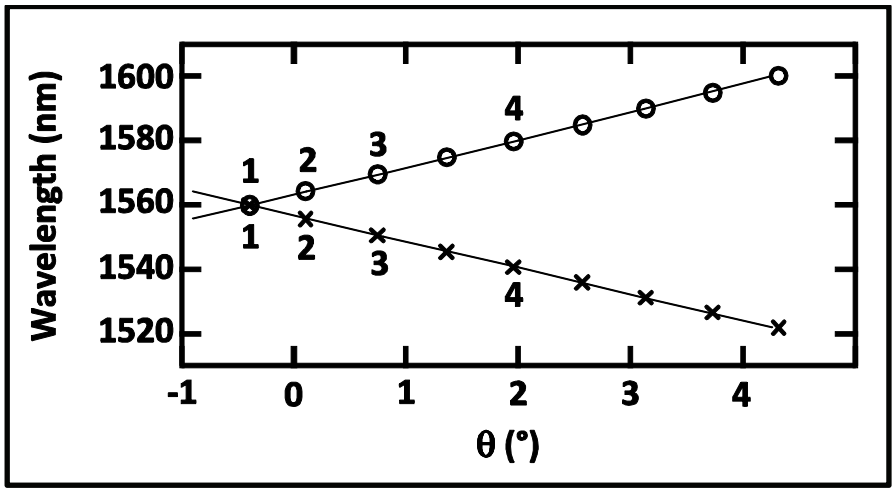

Figure 5.12 Experimental phase matching tuning curve for structure D (interaction 2): the λ_{TE} (circles) and λ_{TM} (crosses) wavelengths are reported versus the corresponding angle θ. The numbered points corresponds to the NF images of Fig. 5.11. The experimental data are here compared with result of 1D simulations (solid line).

1560 nm: an emission angle θ = 0.4° is inferred, in good agreement with the calculated value θ = 0.38°. In the second image, the difference between the two injected wavelengths compensates for the weak birefringence of the waveguide: accordingly, the period is very long, and corresponds to an emission angle of 0.1°. In the successive images, as the split between λ_{TE} and λ_{TM} is increased, the fringe period gets shorter as the emission angle gets larger.

NF acquisitions were obtained for periods down to Λ = 5 μm, corresponding to θ = 4.3°. The experimental PM angles are summarized in Figure 5.12, compared with the calculated tuning curve. The fine agreement is the result of the reliability of the technological processes involved, combined with the intrinsic robustness of the counterpropagating PM condition with respect to tolerances on the nominal structure. [Ducci, 2005]

5.3 Investigation of the efficiency of counterpropagating PF

In the previous Section we have shown how SESHG and SESFG can be exploited to experimentally investigate the PM condition of a waveguide designed for PF in a counterpropagating geometry. For this peculiar configuration, SESHG exhibits an additional functionality: as the efficiency of down- and up-conversion are directly related, a quantitative analysis of SESHG allows one to infer the PF performances.

5.3.1 SESHG conversion efficiency

This approach is similar to that described in Section 3.2 to study the gain coefficient for collinear PF. However, for the counterpropagating geometry, its application plays a more crucial role. The intrinsically lower nonlinear efficiency of this PM scheme makes the detection of the PF fields generated a difficult task, even with photodetectors in the photon-counting regime. Conversely, the SESHG power can be readily measured with standard synchronous detection, thanks to its higher efficiency. Hence, SESHG represents an invaluable tool for design and characterization. In particular it lends itself to compare different structures (e.g. in terms of number of periods and contrast of QPM grating) in order to select the most performing design. In the following, an example of this kind of measurement is described.

The reported experiment has been carried out on a C sample, with ridge width w = 6 μm and length L = 4 mm. Based on the modeling scheme mentioned in Section 1.2.6, we calculate a nonlinear conversion efficiency $\eta = P_{SESHG}/P_{FF}^2 = 2 \cdot 10^{-5}$ W^{-1} for this sample. The pump source is

a 10 mW CW DFB laser diode at λ_ω = 1.55 μm, linearly polarized at 45° relative to waveguide plane. Two 40X microscope objectives are employed for waveguide input and output coupling. The coupled pump power is inferred by its throughput, measured with a Ge photodiode, while the second-harmonic field is detected by means of a large area calibrated Si photodiode plus lock-in amplifier.

Figure 5.13a shows the measured SESHG power versus the coupled power at λ_ω, after calibration of optics: experimental data points nicely follow a parabolic trend, as expected for a frequency-doubling process. In good agreement with predictions, the experimental conversion efficiency is $\eta = P_{SESHG}/P_{FF}^2 = (1.4 \pm 0.6)\cdot 10^{-5}\ W^{-1}$, corresponding to a nonlinear cross section $A_{nl} = 2\cdot 10^{-7}\ W^{-1}cm^{-1}mm$.

In order to experimentally explore the positive impact of the QPM vertical grating, we have performed a further experiment on the same sample, with a pump at λ_ω = 1.32 μm. For a λ_ω different from the nominal one, the in-plane momentum conservation is anyway fulfilled, thanks to the self-adjustment of the SESHG emission angle. However, a lower conversion efficiency is expected, since the QPM period lends itself to compensate the vertical phase mismatch only at λ_ω = 1.55 μm. The source we have adopted for this experiment is a mode-locked Nd:YAG oscillating at 1.32 μm. The choice of a high power pulsed source is motivated by the one-order-of-magnitude lower efficiency calculated at this wavelength. The experimental data of SESHG power versus the coupled power at 1.32 μm are shown in Figure 5.13b: the conversion efficiency following from the quadratic fit is $\eta = (2 \pm 0.8)\cdot 10^{-6}\ W^{-1}$, in perfect

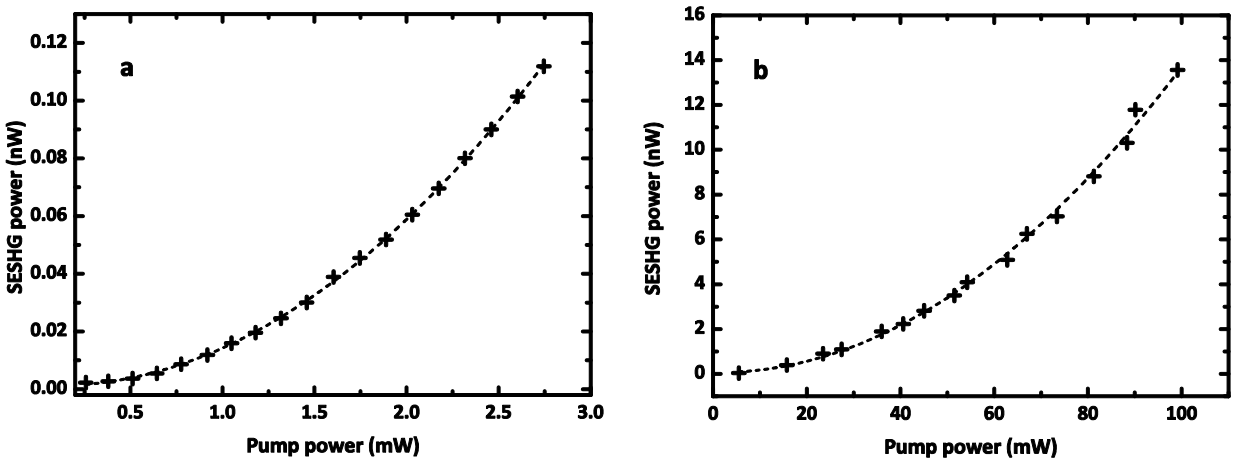

Figure 5.13 SESHG vs pump power in structure C at λ_ω = 1.55 μm (a) and at λ_ω = 1.32 μm (b).

agreement with our expectations.

In both cases, the experimental SESHG rates are consistent with our simulations, and the comparison between the two curves measured at the two different wavelengths points out the positive impact of the QPM vertical grating: the generation efficiency at 1.55 μm is one order of magnitude higher than that experienced at 1.32 μm, and is comparable to the highest values reported in literature. [Degen, 2002]

Unlike in an all-guided $\chi^{(2)}$ process, the generation rates for PF cannot be directly inferred from the SESHG efficiency, since in the counterpropagating geometry the SESHG and the inverse SPDC are not truly reciprocal interactions. The difference concerns the intensity distribution of the 2ω field. For the former process this is determined by the spatial distribution of the nonlinear polarization $P^{(2)}$. Differently, for the latter, it is fixed by the transmission of the pump wave through the multilayer structure, under the effect of the multiple reflections at the layers interfaces.

The question arises whether it is possible to experimentally evaluate the efficiency of counterpropagating PF through a seeded experiment. A positive answer is provided by an experiment of BDFG, since it relies on the same pumping geometry and thus the same overlap integral of counterpropagating PF. Clearly, the comparative advantage of BDFG consists in its higher generated power than in PF. Accordingly, the DFG detection can be accomplished by means of a low-noise photodiode plus lock-in amplifier.

5.3.2 Counter-propagating difference-frequency generation

With respect to SESHG and SESFG, this process requires a more complex setup, with two laser beams in a non-collinear geometry. On the other hand, it allows one to achieve an experimental feedback on two crucial features of the tested device: the overlap integral and the PF phase-matching bandwidth. Both of them are necessary to obtain a reliable prediction of the PF efficiency: the former parameter plays a key a role as regards the nonlinear conversion efficiency, while the latter quantitatively determines the effective input of the quantum noise.

The inputs are provided by a pump beam impinging on the top surface of the ridge waveguide, plus an end-fire injected seed. Through the interaction of these two fields, a counterpropagating mode is generated at the difference frequency. As suggested by the tuning curves shown in Figure 5.9, four different seed-injection choices are possible for a given

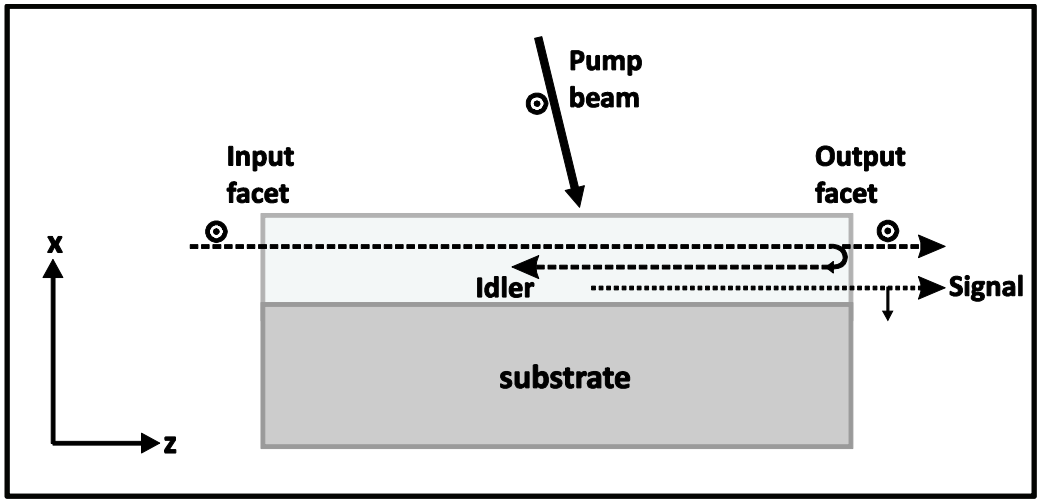

Figure 5.14 DFG experiment scheme: the TE injected beam, after backreflection at the output facet, acts like idler mode, generating a TM signal mode emitted by the output facet.

incidence angle: signal (TE, TM) or idler (TE, TM).[59] Among these we have chosen to seed a TE polarized idler mode, with the practical setup illustrated in Figure 5.14: at the input facet we have end-fire coupled a TE beam copropagating with the pump, relying on the Fresnel back-reflection at the output facet to excite the TE idler. This has been done with the aim of measuring the generated signal at the output facet.

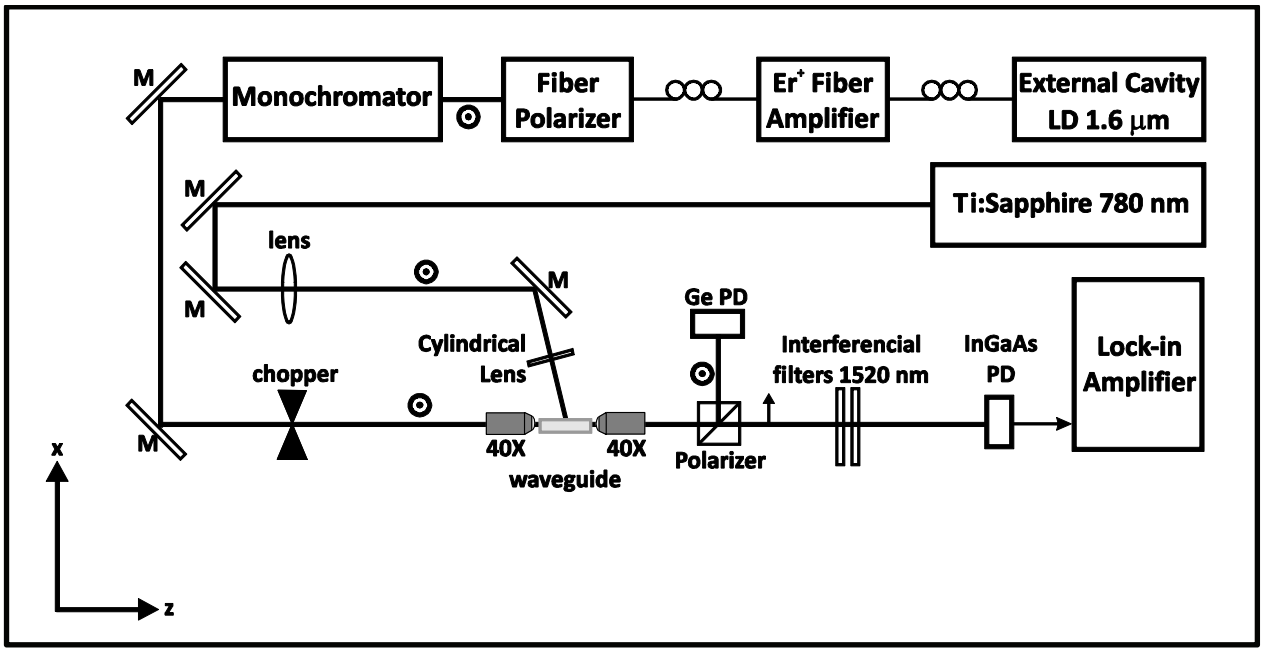

Figure 5.15 Experimental setup for the counterpropating DFG experiment.

[59] We remind that, according to the convention we established for this phase-matching configuration, the term signal refers to the interacting mode copropagating with the pump, while the term idler refers to the interacting mode travelling in the opposite direction.

In order to take advantage of the experimental tuning curve of Figure 5.12, the experiment has been performed on the same ridge waveguide (L = 0.87 mm, w = 4 μm) used for the SESFG experiment.

The complete experimental setup is shown in Figure 5.15: the pump source is the 3900S Ti:Sapphire at 780 nm. The P_P = 70 mW pump beam, strongly focused along y, impinges on the waveguides at an angle θ = 4.3°, far from degeneracy. The idler source is an external cavity laser diode, amplified with an Er^+-doped fiber. The TE polarized beam at λ_I = 1.60 μm is injected into the input facet with a 40X microscope objective. At the waveguide output, its throughput and the generated signal at 1.52 μm are collimated with a second 40X objective and split with a polarizing beam-splitter. The former is measured with a calibrated Ge photodiode. The latter is further filtered with two interferential filters centered at 1520 nm, and detected with an InGaAs low-noise fibered photodiode. This is connected to a lock-in amplifier through a high-gain preamplifier.[60]

Figure 5.16 shows the obtained BDFG spectrum, normalized to the idler power. It exhibits the typical PM $sinc^2$ shape, with a linewidth (FWHM) of 0.30 nm, consistent with the result of our simulations, 0.35 nm. At perfect PM (λ_I = 1601.8 nm) the internal conversion efficiency is $\eta = P_S/P_P P_I = (3.5 \pm 2)\cdot 10^{-6}\ W^{-1}$, in reasonable agreement with the result of our 1D

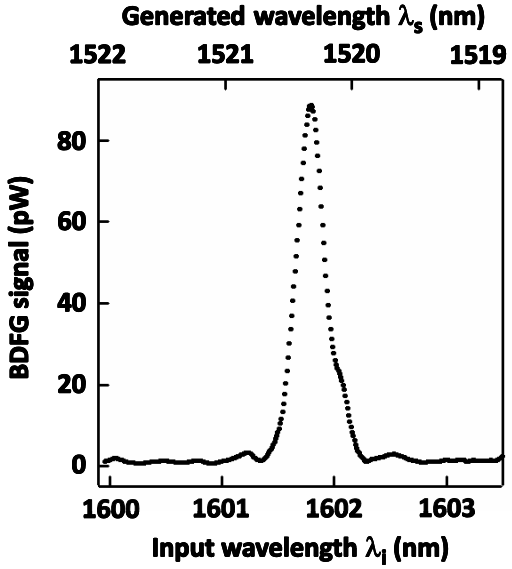

Figure 5.16 Experimental counterpropagating DFG signal, corresponding to P_I = 350 μW and P_P = 70 mW. The generated wavelength is deduced from the input wavelength through energy conservation.

[60] Such detection system is sensitive to an optical power as low as 1 pW.

calculations $\eta = 1.5 \cdot 10^{-5}\ W^{-1}$. The discrepancy between the two values can be mainly ascribed to the non-optimum overlap between the pump spot and the interacting mode profiles along y.

5.4 Chapter conclusion

In this chapter we have described the use of a few $\chi^{(2)}$ processes as characterization tools for nonlinear devices. These have allowed us to investigate the main features of AlGaAs waveguides: effective indices, nonlinear overlap integral, and losses.

Firstly, tunable PF. Here this process has been proposed to measure the losses of a nonlinear medium, especially in wavelength ranges not attainable with common sources and detectors. Such technique has been demonstrated in GaAs/AlOx waveguide, where it has allowed to investigate the AlOx absorption peak around 3 μm.

Secondly, surface-emitted frequency conversion. This interaction, in the degenerate case (SESHG), is well known as the most convenient technique to directly measure the birefringence of GaAs waveguides. Here we have presented its non-degenerate extension (SESFG) which has been exploited to investigate the complete tuning curve of a counterpropagating twin-photon source. The conversion efficiency of the same device has then been quantitatively characterized through SESHG and a novel DFG geometry, the BDFG. These measurements have proven crucial towards the subsequent demonstration of PF in this waveguide, recently reported by Lanco et al. [Lanco, 2006a]

Conclusion

The main goal of this thesis is the development of an integrated source for the near- and mid-IR, based on frequency down-conversion in AlGaAs waveguides. The phase-matching scheme adopted is based on form birefringence in a multilayer guiding core composed of GaAs and AlOx. Such approach has allowed to get round GaAs optical isotropy and to demonstrate several guided-wave nonlinear interactions in the last ten years, until the achievement of parametric fluorescence in 2001. The weak point of GaAs/AlOx integrated frequency converters are scattering losses, which arise from the oxidation of AlAs layers. Optical losses have severely affected the efficiency of most devices reported and, despite the significant technological improvements, are still more than one-order-of-magnitude higher than in lithium niobate waveguides. To date, such drawback has prevented the exploitation of GaAs/AlOx waveguides for the fabrication of an integrated optical parametric oscillator.

In order to pursue this ambitious goal, we have fabricated form birefringent nonlinear waveguides for parametric generation from a 1 μm pump. In this configuration the generated wavelengths span the spectral region between 1.4 and 4 μm, a range of strong interest to the field of spectroscopy, with possible applications in environmental sensing and process monitoring.

Waveguide processing is supposed to play a key role for the further development of GaAs/AlOx frequency converters. In this respect, we have introduced a novel procedure for the definition and the subsequent oxidation of ridge waveguides. At variance with processing schemes adopted to date, this technique is based on a single lithographic step to define mesa for both AlAs lateral oxidation and light confinement. Resorting to chemical etching, this approach has allowed to considerably reduce the oxidation time without increasing the scattering arising from roughness on ridge sidewalls. Accordingly, record propagation losses as low as 0.4 cm^{-1} have been obtained. Losses were systematically checked by measuring the contrast of Fabry-Perot transmission fringes. Such simple technique represents the ideal tool to provide a feedback about the convenience of a given technological process. A further decrease of loss is expected from a deep knowledge of AlAs layers oxidation dynamics, not yet achieved in spite of the numerous successful applications of this material. To this purpose, an extensive study based on TEM observations is actually in progress in the DON group of the MPQ

laboratory.

Besides processing optimization, our work aimed at a full knowledge of the nonlinear features of the final device. This purpose was pursued by performing a few complementary nonlinear measurements.

The first experiment was parametric fluorescence, carried out in order to investigate the generation efficiency and the tuning range of our waveguides. In this process we obtained unprecedented performances in terms of conversion efficiency and tuning range, covering the spectrum between 1.7 and 2.7 μm.

Two additional experiments were then performed, to reliably ascertain the parametric gain coefficient. Firstly, SHG from a pump field at 2 μm, where we achieved the record conversion efficiency for semiconductor waveguides, η_{norm} = 1500% $W^{-1}cm^{-2}$. Secondly, seeded down conversion. Besides being the first demonstration of parametric amplification in semiconductor waveguides, such experiment has confirmed the value obtained in the former measurement, with an increased accuracy. These results have confirmed form birefringence in GaAs/AlOx as the most performing approach to date in nonlinear semiconductor waveguides.

The performances obtained in the experiments mentioned above encouraged us to fabricate the first integrated mirrors, in order to achieve parametric oscillation. On the basis of our experimental values of attenuation coefficient and parametric gain, we estimate doubly-resonant oscillation threshold to be within reach with a facet reflectivity not lower than 84%. Accordingly, we designed and fabricated Si/Al_2O_3 six-layer facet coatings, to obtain a double-pump-pass, doubly-resonant configuration. Regretfully, such integrated mirrors were affected by poor adherence: besides significantly limiting pump coupling, they often get detached for high pumping levels. Work is in progress within the DON group of the MPQ laboratory, to develop both a successful deposition technology and to fabricate planar etched distributed Bragg reflectors, in collaboration with the LPN Laboratory (Marcoussis).

The development of GaAs nonlinear devices has been pursued also through the development of novel characterization techniques. In this respect, we have focused onto the exploitation of nonlinear interactions, like surface-emitted frequency conversion, backward difference frequency generation and parametric fluorescence, towards the investigation of the main features of nonlinear waveguides: phase-matching condition, conversion efficiency and

propagation losses. The practical employment of such tools has e.g. allowed us to precisely measure AlOx absorption between 2 and 4 μm.

List of symbols

1D	One-dimensional
2D	Two-dimensional
3D	Three-Dimensional
AlOx	Non-stoichiometric Aluminum Oxide
AR	Anti-Reflective
AS	Auger Spectroscopy
BBO	β-Barium Borate (BaB_2O_4)
BDFG	Backward Difference Frequency Generation
CCD	Charged-Coupled Device
CW	Continuous Wave
DFB	Distributed Feedback
DBR	Distributed Bragg Reflector
DFG	Difference-Frequency Generation
DROPO	Doubly-Resonant Optical Parametric Oscillator
F	Finesse
FB	Form Birefringence
FDFD	Finite-Difference Frequency Domain
FDTD	Finite-Difference Time Domain
FF	Far-field
FIR	Far Infrared
FSR	Free Spectral Range
FWHM	Full Width at Half Maximum
GaOx	Gallium Oxide
IR	Infrared
KTP	Potassium Titanyl Phosphate ($KTiOPO_4$)
MBE	Molecular Beam Epitaxy
MIR	Mid Infrared
MOS	Metal-Oxide-Semiconductor
MPM	Modal Phase Matching
NF	Near Field
NIR	Near Infrared
NLO	Nonlinear Optics
OPA	Optical Parametric Amplification
OP-GaAs	Orientation-patterned GaAs
OPO	Optical Parametric Oscillator
PF	Parametric Fluorescence
PM	Phase Matching
PPLN	Periodically Poled Lithium Niobate
QCL	Quantum Cascade Laser
QPM	Quasi Phase Matching
SEM	Scanning Electron Microscopy
SESFG	Surface-Emitted Sum-Frequency Generation
SESHG	Surface-Emitted Second-Harmonic Generation

SFG	Sum Frequency Generation
SH	Second Harmonic
SHG	Second Harmonic Generation
SNR	Signal-to-Noise Ratio
SPDC	Spontaneous Parametric Down-Conversion
SROPO	Singly-Resonant Optical Parametric Oscillator
TE	Transverse-Electric
TEM	Transmission Electron Microscopy
TM	Transverse-Magnetic
TPA	Two-photon Absorption
UV	Ultraviolet
VCSEL	Vertical Cavity Surface Emitting Laser
YAG	Yttrium Aluminum Garnet

References

[Adachi, 1988] S. Adachi, "Model dielectric constants of Si and Ge", Phys. Rev. B **38**, 12966 (1988).

[Afromovitz, 1974] M. A. Afromovitz, "Refractive index of $Al_xGa_{1-x}As$", Solid State Commun. **15**, 59 (1974).

[Arbore, 1997] M. A. Arbore and M. Fejer, "Singly Resonant Optical Parametric Oscillation in Periodically Poled Lithium Niobate Waveguides", Opt. Lett. **22**, 151 (1983).

[Armstrong, 1962] J. A. Armstrong, N. Bloembergen, J. Ducuing, and P. S. Pershan, "Interactions between light waves in a nonlinear dielectric", Phys. Rev. **127**, 1918 (1962).

[Arnaud, 1971] J. A. Arnaud, W. M. Hubbard, G. D. Mandeville, B. de la Clavidre, E. A. Franke, and J. M. Franke, "Technique for Fast Measurement of Gaussian Laser Beam Parameters", Appl. Opt. **10,** 2775 (1971).

[Ashby, 1997] C. I. H. Ashby, J. P. Sullivan, P. P. Newcomer, N. A. Missert, H. Q. Hou, B. E. Hammons, M. J. Hafich, and A. G. Baca, "Wet oxidation of $Al_xGa_{1-x}As$: Temporal evolution of composition and microstructure and the implications for metal-insulator-semiconductor applications", Appl. Phys. Lett. **70**, 2443 (1997).

[Baldi, 1996] P. Baldi, M. Sundheimer, K. El Hadi, M. P. de Micheli, and D. B. Ostrowsky, "Comparison between difference-frequency generation and parametric fluorescence in quasi-phase-matched lithium niobate stripe waveguides", IEEE J. Sel. Topics Quantum Electron. **2**, 385 (1996).

[Bava, 1987] G. P. Bava, I. Montrosset, W. Solher, and H. Suche, "Numerical Modeling of Ti:LiNbO3 Integrated Optical Parametric Oscillators", IEEE J. Quantum Electron. **23**, 42 (1987).

[Bjorkholm, 1970] J. E. Bjorkhom, A. Ashkin, and R. G. Smith, "Improvement of Optical Parametric Oscillators by Non resonant Pump Reflection", IEEE J. Quantum Electron. **6**, 797 (1970).

[Born, 1980] M. Born and E. Wolf, *Principles of optics*, Pergamon Press, Oxford (1980).

[Bortz, 1995] M. L. Bortz, M. A. Arbore, and M. M. Fejer, "Quasi-phase-matched optical parametric amplification and oscillation in periodically poled $LiNbO_3$ waveguides", Opt. Lett. **20**, 49 (1995).

[Bosenberg, 1996] W. R. Bosenberg, A. Drobshoff, J. I. Alexander, L. E. Myers, and R. L. Byer, "93% pump depletion, 3.5-W continuous-wave, singly resonant optical parametric oscillator", Opt. Lett. **21**, 1336 (1996).

[Bouwmeester, 2000] D. Bouwmeester, D. Eckert, and A. Zeilinger, *The physics of quantum information*, Springer, New York (2000).

[Boyd, 1968] G. D. Boyd and D. A. Kleinman, "Parametric Interaction of Focused Gaussian Light Beams", J. Appl. Phys. **39**, 3597 (1968).

[Bravetti, 1998] P. Bravetti, A. Fiore, V. Berger, E. Rosencher, J. Nagle, and O. Gauthier-Lafaye, "5.2–5.6 μm source tunable by frequency conversion in a GaAs-based waveguide", Opt. Lett. **23**, 331 (1998).

[Byer, 1968] R. L. Byer and S. E. Harris, "Power and Bandwidth of Spontaneous Parametric Emission", Phys. Rev. **168**, 1064 (1968).

[Chanvillard, 2000] L. Chanvillard, P. Aschiéri, P. Baldi, D. B. Ostrowsky, M. de Micheli, L. Huang, and D. J. Bamford, "Soft proton exchange on periodically poled $LiNbO_3$: A simple waveguide fabrication process for highly efficient nonlinear interactions", Appl. Phys. Lett. **76**, 1089 (2000).

[Chen, 1995] E. I. Chen, N. Holonyak, Jr., and S. A. Maranowski, "$Al_xGa_{1-x}As$–GaAs metal–oxide semiconductor field effect transistors formed by lateral water vapor oxidation of AlAs", Appl. Phys. Lett. **66**, 2688 (1995).

[Choi, 2004] H. K. Choi, *Long-Wavelength Infrared Semiconductor Lasers*, Wiley, New York (2004).

[Choquette, 1995] K. D. Choquette, K. L. Lear, J. R. P. Schneider, K. M. Geib, J. J. Figiel, and R. Hull, "Fabrication and performance of selectively oxidized vertical-cavity lasers", IEEE Photon. Technol. Lett. **7**, 1237 (1995).

[Choquette, 1996] K. D. Choquette, K. M. Geib, H. C. Chui, B. E. Hammons, H. Q. Hou, T. J. Drummond, and R. Hull, "Selective oxidation of buried AlGaAs versus AlAs layers", Appl. Phys. Lett. **69**, 1385 (1996).

[Cohen, 1982] L. G. Cohen, W. L. Mammel, and S. J. Jang, "Low-loss quadruple-clad single-mode light guides with dispersion below 2 ps/km nm over the 1.28 μm-1.65 μm wavelength range", Electron. Lett. **18**, 1023 (1982).

[Dallesasse, 1990a] J. M. Dallesasse, J. N. Holonyak , A. R. Sugg, T. A. Richard, and N. El-Zein, "Hydrolyzation oxidation of $Al_xGa_{1-x}As$-AlAs-GaAs quantum-well heterostructures and superlattices", Appl. Phys. Lett. **57**, 2844 (1990).

[Dallesasse, 1990b] J. M. Dallesasse, P. Gavrilovic, N. Holoniak Jr., R. W. Kaliski, D. W. Nam, E. J. Vesely, and R. D. Burnham, "Stability of AlAs in $Al_xGa_{1-x}As$-AlAs-GaAs quantum-well heterostructures", Appl. Phys. Lett. **56**, 2436 (1990).

[De Rossi, 2001] A. De Rossi, V. Berger, M. Calligaro, G. Leo, V. Ortiz, and X. Marcadet, "Parametric fluorescence in oxidized aluminum gallium arsenide waveguides", Appl. Phys. Lett. **79**, 3758 (2001).

[De Rossi, 2002] A. De Rossi and V. Berger, "Counterpropagating Twin Photons by Parametric Fluorescence", Phys. Rev. Lett. **88**, 043901 (2002).

[De Rossi, 2005a] A. De Rossi, V. Ortiz, M. Calligaro, L. Lanco, S. Ducci, V. Berger, and I. Sagnes, "Measuring propagation loss in a multimode semiconductor waveguide", J. Appl. Phys. **97**, 073105 (2005).

[De Rossi, 2005b] A. De Rossi, V. Berger, G. Leo, and G. Assanto, "Form birefringence phase matching in multilayer semiconductor waveguides: tuning and tolerances", IEEE J. Quantum Electron. **41**, 1293 (2005).

[Degen, 2002] C. Degen, G. Jennemann, I. Fischer, W. Elsäßer, S. Leu, R Rettig, and W. Stolz, "Surface-emitting second-harmonic generation in AlGaAs/GaAs waveguides", Opt. Quantum Electron. **34**, 707 (2002).

[Ducci, 2005] S. Ducci, L. Lanco, Y. Seurin, G. Leo, V. Berger, A. De Rossi, and X. Marcadet, "Semiconductor sources of twin photons for quantum information", J. Opt. B **7**, 158 (2005).

[Ducci, 2004] S. Ducci, L. Lanco, V. Berger, A. De Rossi, V. Ortiz, and M. Calligaro, "Continuous-wave second-harmonic generation in modal phase matched semiconductor waveguides", Appl. Phys. Lett. **84**, 2974 (2004).

[Durand, 2003] O. Durand, F. Wyckzisk, J. Olivier, M. Magis, P. Galtier, A. De Rossi, M. Calligaro, V. Ortiz, G. Leo, and G. Assanto, "Contraction of aluminum oxide thin layers in optical heterostructures", Appl. Phys. Lett. **83**, 2554 (2003).

[Ebrahim-Zadeh, 2000] M. Ebrahim-Zadeh and M. H. Dunn, "Optical Parametric Oscillators" in *Handbook of Optics, Volume IV*, McGraw-Hill, New York (2000).

[Eckardt, 1991] R. C. Eckardt, C. D. Nabors, W. J. Kozlovsky, and R. L. Byer, "Optical parametric oscillator frequency tuning and control", J. Opt. Soc. Am. B **8**, 646 (1991).

[Eyres, 2001] L. A. Eyres, P. J. Tourreau, T. J. Pinguet, C. B. Ebert, J. S. Harris, M. M. Fejer, L. Becouarn, B. Gerard, and E. Lallier, "All-epitaxial fabrication of thick, orientation-patterned GaAs films for nonlinear optical frequency conversion", Appl. Phys. Lett. **79**, 904 (2001).

[Falk, 1971] J. Falk, "Instabilities in the Doubly Resonant Parametric Oscillator: A Theoretical Study", IEEE J. Quantum Electron. **7**, 230 (1971).

[Fiore, 1997a] A. Fiore, V. Berger, E. Rosencher, P. Bravetti, N. Laurent, and J. Nagle, "Phase-matched mid-infrared difference frequency generation in GaAs-based waveguides", Appl. Phys. Lett. **71**, 3622 (1997).

[Fiore, 1997b] A. Fiore, V. Berger, E. Rosencher, S. Crouzy, N. Laurent, and J. Nagle, "$\Delta n = 0.22$ birefringence measurement by surface emitting second harmonic generation in selectively oxidized GaAs/AlAs optical waveguides", Appl. Phys. Lett. **71**, 2587 (1997).

[Fiore, 1997c] A. Fiore, PhD Thesis 4819 at the University of Paris-XI (1997).

[Fiore, 1998a] A. Fiore, J. Sanz, L. Delobel, P. van der Meer, P. Bravetti, V. Berger, E. Rosencher, and J. Nagle, "Second-harmonic generation at $\lambda = 1.6$ μm in AlGaAs/Al_2O_3 waveguides using birefringence phase matching", Appl. Phys. Lett **72**, 2942 (1998).

[Fiore, 1998b] A. Fiore, V. Berger, E. Rosencher, P. Bravetti, and J. Nagle, "Phase-matching using an isotropic nonlinear material", Nature **391**, 463 (1998).

[Franken, 1961] P. A. Franken, A. E. Hill, C. W. Peters, and G. Weinreich, "Generation of Optical Harmonics", Phys. Rev. Lett. **7**, 118 (1961).

[Gehrsitz, 2000] S. Gehrsitz, F. K. Reinhart, C. Gourgon, N. Herres, A. Vonlanthen, and H. Sigg, "The refractive index of $Al_xGa_{1-x}As$ below the band gap: Accurate determination and empirical modeling"**,** J. Appl. Phys. **87**, 7825 (2000).

[Giordmaine, 1966] J. A. Giordmaine and R. C. Miller, "Optical parametric oscillation in $LiNbO_3$", in *Physics of Quantum Electronics*, R. L. Kelley, B. Lax, and P. E. Tannenwald, eds., McGraw-Hill, New York (1966).

[Guha, 1996] S. Guha, F. Agahi, B. Pezeshki, J. A. Kash, D. W. Kisker, and N. A. Bojarczuk, "Microstructure of AlGaAs-oxide heterolayers formed by wet oxidation", Appl. Phys. Lett. **68**, 906 (1996).

[Gwarek, 2003] W. K. Gwarek and M. Celuch-Marcysiak, "Wide-Band S-Parameter Extraction From FD-TD Simulations for Propagating and Evanescent Modes in Inhomogeneous Guides", IEEE Trans. Microwave Theory Tech. **51**, 1920 (2003).

[Hall, 1999] D. C. Hall, H. Wu, L. Kou, Y. Luo, R. J. Epstein, O. Blum, and H. Hou , "Refractive index and hygroscopic stability of $Al_xGa_{1-x}As$ native oxides", Appl. Phys. Lett. **75**, 1110 (1999).

[Hampel, 1986] B. Hampel and W. Sohler, "Optical parametric fluorescence in Ti:$LiNbO_3$ channel waveguides", in *Integrated Optical Circuit Engineering* III, R. T. Kersten, ed. Proc. SPIE **651**, 229 (1986).

[Harris, 1967] S. E. Harris, M. K. Oshman, and R. L. Byer, "Observation of tunable optical parametric fluorescence", Phys. Rev. Lett. **18**, 732 (1967).

[Herzinger, 1993] C. M. Herzinger, C. C. Lu, and T. A. Temple, "The semiconductor waveguide facet reflectivity problem", IEEE J. Quantum Electron. **29**, 2273 (1993).

[Hofmann, 1999] D. Hofmann, H. Herrmann, G. Schreiber, W. Grundkötter, R. Ricken, and W. Sohler, "Continuous-wave mid-infrared doubly resonant optical parametric oscillator with periodically poled Ti:$LiNbO_3$ waveguide", OSA Annual Meeting, Santa Clara (USA), September 26-29 1999.

[Hofmann, 2000] D. Hofmann, G. Schreiber, W. Grundkötter, R. Ricken, and W. Sohler, "Mid-infrared continuous-wave singly resonant optical parametric oscillator with periodically poled Ti:$LiNbO_3$ waveguide," in CLEO Europe 2000, Nice (France), September 10-15 2000.

[Hunsperger, 2002] R. G. Hunsperger, *Integrated Optics*, Springer, New York (2002).

[Ikegami, 1972] T. Ikegami, "Reflectivity of Mode at Facet and Oscillation Mode in Double-Heterostructure Injection Lasers", IEEE J. Quantum Electron. **8**, 470 (1972).

[Janz, 1998] S. Janz, Y. Beaulieu, A. Fiore, P. Bravetti, V. Berger, E. Rosencher, and J. Nagle, "Surface emitted second-harmonic generation from a quasi-phase matched waveguide in an $Al_xGa_{1-x}As/Al_2O_3$ microcavity", Opt. Express **2**, 462 (1998).

[Kaminow, 1978] I. P. Kaminow and L. W. Stulz, "Loss in cleaved Ti-diffused $LiNbO_3$ waveguides", Appl. Phys. Lett. **33**, 62 (1978).

[Kim, 1996] J.-H. Kim, D. H. Lim, K. S. Kim, G. M. Yang, K. Y. Lim, and H. J. Lee, "Lateral wet oxidation of $Al_xGa_{1-x}As$-GaAs depending on its structures", Appl. Phys. Lett. **69**, 3357 (1996).

[Kintaka, 1996] K. Kintaka, M. Fujimura, T. Suhara, and H. Nishihara, "High-efficiency $LiNbO_3$ waveguide second-harmonic generation devices with ferroelectric-domain-inverted gratings fabricated by applying voltage", J. Ligthwave Technol. **14**, 462 (1996).

[Kleinman, 1962] D. A. Kleinman, "Nonlinear Dielectric Polarization in Optical Media", Phys. Rev. **126**, 1977 (1962).

[Knopp, 1998] K. J. Knopp, R. P. Mirin, D. H. Christensen, K. A. Bertness, A. Roshko, and R. A. Synowicki, "Optical constants of $(Al_{0.98}Ga_{0.02})_xO_y$ native oxides", Appl. Phys. Lett. **73**, 3512 (1998).

[Korkishko, 2003] Yu. N. Korkishko, V. A. Fedorov, S. M. Kostritskii, E. I. Maslennikov, M. V. Frolova, and A. N. Alkaev, "Proton-exchanged waveguides in MgO-doped LiNbO3: Optical and structural properties", J. Appl. Phys. **94**, 1163 (2003).

[Kozlovsky, 1988] W. J. Kozlovsky, E. K. Gustafson, R. C. Eckardt, and R. L. Byer, "Efficient monolithic MgO:LiNbO3 singly resonant optical parametric oscillator", Opt. Lett. **13**, 1102 (1988).

[Krauss, 1996] T. F. Krauss and M. R. De la Rue, "Optical characterization of waveguide based photonic microstructures", Appl. Phys. Lett. **68**, 1613 (1996).

[Lanco, 2006a] L. Lanco, S. Ducci, J.-P. Likforman, X. Marcadet, J. A. W. van Houwelingen, H. Zbinden, G. Leo, and V. Berger, "Semiconductor Waveguide Source of Counterpropagating Twin Photons", Phys. Rev. Lett. **97,** 173901 (2006).

[Lanco, 2006b] L. Lanco, S. Ducci, J.-P. Likforman, M. Ravaro, P. Filloux, X. Marcadet, G. Leo, and V. Berger, "Backward difference frequency generation in an AlGaAs waveguide", Appl. Phys. Lett. **89**, 031106 (2006).

[Le Dû, 2006] M. Le Dû, I. Sagnes, G. Beaudoin, L. Travers, J.-C. Esnault, and J.-C. Harmand, "Enhanced kinetics of $Al_{0.97}Ga_{0.03}As$ wet oxidation through the use of hydrogenation", Appl. Phys. Lett. **89**, 111105 (2006).

[Leo, 2001] G. Leo, M. Secondini, M. Morabito, A. De Rossi, G. Assanto, A. Fiore, V. Berger, M. Calligaro, and J. Nagle, "Birefringence evaluation of multimode multilayer AlGaAs/AlAs waveguides", Appl. Phys. Lett. **78**, 1472 (2001).

[MacDougal, 1994] M. H. MacDougal, H. Zhao, P. D. Dapkus, M. Ziari, and W.H. Steier, "Wide-bandwidth distributed Bragg reflectors using oxide/GaAs multilayers", Electron. Lett. **30**, 1147 (1994).

[Martin, 1995] P. Martin, E. M. Skouri, L. Chusseau, C. Alibert, and H. Bissessur, "Accurate refractive index measurements of doped and undoped InP by a grating coupling technique", Appl. Phys. Lett. **67**, 881 (1995).

[Moutzouris, 2001] K. Moutzouris, S. Venugopal Rao, M. Ebrahimzadeh, A. De Rossi, V. Berger, M. Calligaro, and V. Ortiz, "Efficient second-harmonic generation in birefringently phase-matched GaAs/Al_2O_3 waveguides", Opt. Lett. **26**, 1785 (2001).

[Nabors, 1990] C. D. Nabors, S. T. Yang, T. Day, and R. L. Byer, "Coherence properties of a doubly resonant monolithic optical parametric oscillator", J. Opt. Soc. Am. B **7**, 815 (1990).

[Nickel, 1995] H. Nickel, "A detailed experimental study of the wet oxidation kinetics of $Al_xGa_{1-x}As$ layers", J. Appl. Phys. **78**, 5201 (1995).

[Normandin, 1979] R. Normandin and G.I. Stegeman, "Nondegenerate four-wave mixing in integrated optics", Opt. Lett. **4**, 58 (1979).

[Ohashi, 1993] M. Ohashi, T. Kondo, R. Ito, S. Fukatsu, Y. Shiraki, K. Kumata, and S. Kano, "Determination of quadratic nonlinear optical coefficient of $Al_xGa_{1-x}As$ system by the method of reflected second harmonics", J. Appl. Phys. **74**, 596 (1993).

[Okamura, 1983] Y. Okamura, S. Yoshinaka, and S. Yamamoto, "Measuring mode propagation losses of integrated optical waveguides: a simple method," Appl. Opt. **22**, 3892 (1983).

[Oster, 2001] B. Oster and H. Fouckhardt, "M-waveguide structures for direct phase matching in AlGaAs", Appl. Phys. B **73**, 535 (2001).

[Padgett, 1994] M. J. Padgett, F. G. Colville, and M. H. Dunn, "Mode Selection in Doubly-resonant Optical Parametric Oscillators", IEEE J. Quantum Electron. **30**, 2979 (1994).

[Palik, 1985] E. D. Palik, *Handbook of Optical Constants of Solids*, Academic Press, New York (1985).

[Rao, 2002] S. Venugopal Rao, K. Moutzouris, M. Ebrahimzadeh, A. De Rossi, G. Gintz, M. Calligaro, V. Ortiz, and V. Berger, "Measurements of optical loss in $GaAs/Al_2O_3$ nonlinear waveguides in the infrared using femtosecond scattering technique", Opt. Commun. **213**, 223 (2002).

[Rao, 2003] S. Venugopal Rao, K. Moutzouris, M. Ebrahimzadeh, A. De Rossi, G. Gintz, M. Calligaro, V. Ortiz, and V. Berger, "Influence of scattering and two-photon absorption on the optical loss in $GaAs/Al_2O_3$ nonlinear waveguides measured using femtosecond pulses", IEEE J. Quant. Electron. **39**, 478 (2003).

[Regener, 1985] R. Regener and W. Sohler, "Loss in low finesse Ti:$LiNbO_3$ optical waveguide resonators", Appl. Phys. B **36**, 143 (1985).

[Richy, 1995] C. Richy, K. I. Petsas, E. Giacobino, C. Fabre, and L. Lugiato, "Observation of bistability and delayed bifurcation in a triply resonant optical parametric oscillator", J. Opt. Soc. Am. B **12**, 456 (1995).

[Scaccabarozzi, 2006] L. Scaccabarozzi, M. M. Fejer, Y. Huo, S. Fan, X. Yu, and J. S. Harris, "Enhanced second-harmonic generation in AlGaAs/Al_xO_y tightly confining waveguides and resonant cavities," Opt. Lett. **31**, 3626 (2006).

[Schreiber, 2000] G. Schreiber, R. Ricken, K. Rochhausen, and W. Sohler, "Doubly resonant near-infrared optical parametric oscillator with periodically poled Ti:$LiNbO_3$ waveguide", CLEO/QELS 2000, San Francisco (USA), May 7-12 2000.

[Schreiber, 2001] G. Schreiber, D. Hofmann, W. Grundkötter, Y. L. Lee, H. Suche, V. Quiring, R. Ricken, and W. Sohier, "Nonlinear Integrated Optical Frequency Converters with Periodically Poled Ti:$LiNbO_3$ Waveguides", Proc. SPIE **4277**, 144 (2001).

[Shen, 1984] Y. R. Shen, *The principles of nonlinear optics*, Wiley, New York (1984).

[Siegman, 1962] A. E. Siegman, "Nonlinear optical effects: An optical power limiter", Appl. Opt. **1**, 739 (1962).

[Skauli, 2002] T. Skauli, K. L. Vodopyanov, T. J. Pinguet, A. Schober, O. Levi, L. A. Eyres, M. M. Fejer, J. S. Harris, B. Gerard, L. Becouarn, and E. Lallier, "Measurement of the nonlinear coefficient of orientation-patterned GaAs and demonstration of highly efficient second-harmonic generation", Opt. Lett. **27**, 628 (2002).

[Smith, 1973] R. G. Smith, "A Study of Factors Affecting the Performance of a Continuously Pumped Doubly Resonant Optical Parametric Oscillator", IEEE J. Quantum Electron. **9**, 530 (1973).

[Sohler, 1980] W. Sohler and H. Suche, "Optical parametric amplification in Ti-diffused $LiNbO_3$ waveguides", Appl. Phys. Lett. **37**, 255 (1980).

[Sohler, 1981] W. Sohler and H. Suche, "Optical parametric oscillation in Ti-diffused $LiNbO_3$ optical waveguide resonators", in Digest of the Third International Conference on Integrated Optics and Optical Fiber Communication, Optical Society of America, Washington D.C. (1981).

[Sorokina, 2003] I. T. Sorokina and K. L. Vodopyanov, *Solid-State Mid-Infrared Laser Sources*, Springer, New York (2003).

[Suche, 1988] H. Suche and W. Sohler, in Integrated and Guided-Wave Optics **5**, Optical Society of America, Washington D.C. (1988).

[Sugg, 1991] A. R. Sugg, N. Holonyak, Jr., J. E. Baker, F. A. Kish, and J. M. Dallesasse, "Native oxide stabilization of AlAs-GaAs heterostructures", Appl. Phys. Lett. **58**, 1199 (1991).

[Sugg, 1993] A. R. Sugg, E. I. Chen, N. Holonyak, Jr., K. C. Hsieh, J. E. Baker, and N. Finnegan "Effects of low-temperature annealing on the native oxide of $Al_xGa_{1-x}As$", J. Appl. Phys. **74**, 3880 (1993).

[Sutherland, 1996] R. L. Sutherland, *Handbook of Non Linear Optics*, Marcel Dekker, New York (1996).

[Tachibana, 2003] H. Tachibana, T. Matsushita, K. Ara, and T. Kondo, "Quasi-phase-matched parametric fluuorescence in periodically inverted GaAs waveguides", CLEO 2003, Baltimore (USA), June 1-6 (2003).

[Taflove, 2000] A. Taflove and S. C. Hagness, *Computational Electrodynamics: The Finite-Difference Time-Domain Method*, Artech House, Boston (2000).

[Takamori, 1996] T. Takamori, K. Takemasa, and T. Kamijoh, "Interface structure of selectively oxidized AlAs/GaAs", Appl. Phys. Lett. **69**, 659 (1996).

[Thompson, 1976] D. E. Thompson, J. D. McMullen, and D. B. Anderson, "Second harmonic generation in GaAs stack of plates using high-power CO_2 laser radiation", Appl. Phys. Lett. **29**, 113 (1976).

[Twesten, 1996] R. D. Twesten, D. M. Follstaedt, K. D. Choquette, and R. P. Schneider, Jr., "Microstructure of laterally oxidized $Al_xGa_{1-x}As$ layers in vertical-cavity lasers", Appl. Phys. Lett. **69**, 19 (1996).

[Vakhshoori, 1988] D. Vakhshoori, M. C. Wu, and S. Wang, "Surface-emitting second-harmonic generator for waveguide study", Appl. Phys. Lett. **52**, 422 (1988).

[Vodopyanov, 2004] K. L. Vodopyanov, O. Levi, P. S. Kuo, T. J. Pinguet, J. S. Harris, M. M. Fejer, B. Gerard, L. Becouarn, and E. Lallier, "Optical parametric oscillation in quasi-phase-matched GaAs", Opt. Lett. **29**, 1912 (2004).

[Vodopyanov, 2006] K. L. Vodopyanov, M. M. Fejer, X. Yu, J. S. Harris, Y.-S. Lee, W. C. Hurlbut, V. G. Kozlov, D. Bliss, and C. Lynch, "Terahertz-wave generation in quasi-phase-matched GaAs", Appl. Phys. Lett. **89,** 141119 (2006).

[Whitbread, 1994] N. D. Whitebread and P. N. Robson, "Theoretical Analysis of Passive Visible Surface-Emitting Second-Harmonic Generators", IEEE J. Quant. Electron **30**, 139 (1994).

[Yang, 1993] S. T. Yang, R. C. Eckardt, and R. L. Byer, "Continuous-wave singly resonant optical parametric oscillator pumped by a single-frequency resonantly doubled Nd:YAG laser", Opt. Lett. **18**, 971 (1993).

[Yang, 1994] S. T. Yang, R. C. Eckardt, and R. L. Byer, "1.9-W cw ring-cavity KTP singly resonant optical parametric oscillator", Opt. Lett. **19**, 475 (1994).

[Yariv, 1989] A. Yariv, *Quantum Electronics*, Wiley, NewYork (1989).

[Yeh, 1988] P. Yeh, *Optical waves in layered media*, Wiley, New York, (1988).

[Yu, 2005] X. Yu, L. Scaccabarozzi, J. S. Harris, Jr., P. S. Kuo, and M. M. Fejer, "Efficient continuous wave second harmonic generation pumped at 1.55 µm in quasi-phase-matched AlGaAs waveguides", Opt. Express **13**, 10742 (2005).

[Yoo, 1995] S. J. B. Yoo, R. Bhat, C. Caneau, and M. A. Koza, "Quasi-phase-matched second-harmonic generation in AlGaAs waveguides with periodic domain inversion achieved by wafer bonding", Appl. Phys. Lett. **66**, 3410 (1995).

[Zheng, 1987] Y. F. Zheng and J. F. Tang, "New automatic design technique for optical coatings", Appl. Opt. **26**, 1546 (1987).

[Zheng, 1998] D. Zheng, L. A. Gordon, Y. S. Wu, R. S. Feigelson, M. M. Fejer, R. L. Byer, and K. L. Vodopyanov, "16-µm infrared generation by difference frequency mixing in diffusion-bonded-stacked GaAs", Opt. Lett. **23**, 1010 (1998).

[Ziel, 1975] J. P. van der Ziel, "Phase-matched Harmonic Generation in a Laminar Structure with Wave Propagation in the plane of the Layers", Appl. Phys. Lett. **26**, 60 (1975).

[Ziel, 1978] J. P. van der Ziel and A. C. Gossard, "Optical birefringence of ultrathin AlGaAs-GaAs Multilayer Heterostructures", J. Appl. Phys. **49**, 2919 (1978).

List of publications

AlGaAs waveguides

Journals

1) M. Ravaro, E. Guillotel, M. Le Dû, C. Manquest, X. Marcadet, S. Ducci, V. Berger, and G. Leo "Nonlinear measurement of mid-IR absorption in AlOx waveguides", Appl. Phys. Lett. **92**, 151111 (2008).

2) M. Ravaro, M. Le Dû, J.-P. Likforman, S. Ducci, V. Berger, and G. Leo, "Estimation of parametric gain in GaAs/AlOx waveguides by fluorescence and second harmonic generation measurements", Appl. Phys. Lett. **91**, 191110 (2007).

3) L. Lanco, S. Ducci, J.-P. Likforman, M. Ravaro, P. Filloux, X. Marcadet, G. Leo and V. Berger, "Backward difference frequency generation in an AlGaAs waveguide", Appl. Phys. Lett. **89**, 031106 (2006).

4) M. Ravaro, Y. Seurin, S. Ducci, G. Leo, V. Berger, A. De Rossi and G. Assanto, "Nonlinear AlGaAs waveguide for the generation of counterpropagating twin photons in the telecom range", J. Appl. Phys. **98**, 063103 (2005).

Conferences

1) M. Ravaro, M. Le Dû, J.-P. Likforman, S. Ducci, V. Berger, and G. Leo, "High-Efficiency, Low-Loss AlGaAs/AlOx Waveguides for Parametric Down-Conversion", Nonlinear Photonics 2007, Quebec City (Canada), September 2-6 2007.

2) M. Ravaro, M. Le Dû, E. Guillotel, J-P. Likforman, S. Ducci, V. Berger, and G. Leo , "Guides d'ondes GaAs/AlOx pour la generation paramétrique: performances et perspectives", 10ème Colloque sur les Lasers et l'Optique Quantique (COLOQ 10), Grenoble (France), July 2-5 2007.

3) E. Guillotel, M. Le Dû, M. Ravaro, C. Langlois, C. Ricolleau, I. Sagnes, J-P. Likforman, S. Ducci,

V. Berger, and G. Leo , "Vers un contrôle ultime de l'oxydation latérale humide de couches d'Al(Ga)As pour son utilisation dans des dispositifs photoniques", 26éme Journées Nationales de l'Optique Guidée, (JNOG2007), Grenoble (France), July 2-5 2007.

4) M. Ravaro, J.-P. Likforman, S. Ducci, V. Berger, and G. Leo, "Parametric Generation in AlGaAs/AlOx waveguides: performances and perspectives", CLEO 07, Baltimore (USA), Mai 6-11 2007.

5) L. Lanco, S. Ducci, J. Likforman, M. Ravaro, V. Berger, and G. Leo, "AlGaAs waveguide generation of counterpropagating twin photons", SPIE Europe International Congress on Optics and Optoelectronics, Prague (Czech Republic), April 16-19 2007.

6) M. Le Dû, E. Guillotel, M. Ravaro, I. Sagnes, J.-P. Likforman, S. Ducci, G. Leo, and V. Berger, "Towards an ultimate control of laterally wet oxidized Al(Ga)As layers for a reliable use in photonics devices", Journées Scientifiques de l'ONERA "Sources optiques paramétriques pour l'infrarouge", Clamart (France), February 5-6 2007.

7) M. Ravaro, M. Le Dû, J.-P. Likforman, S. Ducci, G.Leo, and V. Berger, "Parametric generation in selectively oxidized AlGaAs waveguides", Journées Scientifiques de l'ONERA "Sources optiques paramétriques pour l'infrarouge" Clamart (France), February 5-6 2007.

8) M. Ravaro, J-P. Likforman, S. Ducci, V. Berger, and G. Leo, "Birefringently phase-matched parametric generation in AlGaAs waveguides", Research Conference on Photonic Nano-objects, Les Houches (France), January 22-26 2007.

9) G. Leo, V. Berger, S. Ducci, L. Lanco, and M. Ravaro, "Semiconductor twin-photon sources for quantum information", Mid-infrared coherent sources (MICS 2005), Barcelona (Spain), November 6-11 2005.

10) M. Ravaro, Y. Seurin, S. Ducci, G. Leo, V. Berger, A. De Rossi, and G. Assanto, "Guide nonlinéaire en AlGaAs pour la génération de photons jumeaux contrapropageants", 9ème Colloque sur les Lasers et l'Optique Quantique (COLOQ 9), Dijon (France), September 7-9 2005.

11) Y. Seurin, M. Ravaro, S. Ducci, G. Leo, A. de Rossi, and V. Berger, "Guides d'onde en semiconducteurs pour la génération de photons intriqués contrapropageants", Journée "Nanophotonique et Information Quantique", Paris (France), November 25 2004.

Book chapters

1) M. Ravaro, L. Lanco, X. Marcadet, S. Ducci, V. Berger, and G. Leo, "Parametric fluorescence in semiconductor waveguides", in *Compte Rendus Physique*, Elsevier (in press).

2) L. Lanco, M. Ravaro, J.-P. Likforman, P. Filloux, X. Marcadet, S. Ducci, G. Leo, and V. Berger "Semiconductor waveguides for nonlinear frequency conversion", in *Mid-Infrared Coherent Sources and Applications*, M. Ebrahimzadeh and I. T. Sorokina Eds., Springer (2007).

$LiNbO_3$ waveguides

Journals

1) A. C. Busacca, A. C. Cino, S. Riva Sanseverino, M. Ravaro, and G. Assanto, "Silica masks for improved surface poling of lithium niobate", Electron. Lett. **41**, 92 (2005).

Conferences

1) A. Busacca, M. Cherchi, S. Riva Sanseverino, A. Parisi, A. C. Cino, M. Ravaro, and G. Assanto, "Short period Lithium Niobate poling for nonlinear three waves interactions", European WORKSHOP Photonic Signal Processing for Defence Applications, Roma (Italy), March 17-18 2005.

2) A. C. Busacca, A. C. Cino, M. Ravaro, G. Assanto, F. Caccavale, A. Morbiato, and S. Riva Sanseverino, "Nano-domains definition in congruent lithium niobate by surface periodic electric-field poling", Proc. 12th European Conference on Integrated Optics (ECIO'05), Grenoble (France), April 6-8 2005.